An Integrated Smart Energy Management and Model-Free Control Approaches for Islanded Residential Microgrids

Sarah Kassir

THÈSE DE DOCTORAT DE

NANTES UNIVERSITÉ et UNIVERSITÉ LIBANAISE

ÉCOLE DOCTORALE N° 641
Mathématiques et Sciences et Technologies de l'Information et de la Communication
Spécialité : *Génie Électrique*

Par

« Sarah KASSIR »

An Integrated Smart Energy Management and Model-Free Control Approaches for Islanded Residential Microgrids.

Thèse présentée et soutenue à St Nazaire, le 25 Septembre 2023
Unité de recherche : Institut de Recherche en Énergie Électrique de Nantes Atlantiques (UR 4642)

Rapporteurs avant soutenance :

Farid MEIBODY TABAR, Professeur des Universités, Lemta, Université Lorraine
Abdelhamid RABHI, Professeur des Universités, MIS, Université de Picardie Jules Verne

Composition du Jury :

Présidente : Corinne ALONSO, Professeur des Universités, LAAS, Université Paul Sabatier
Examinateurs : Amrane OUKAOUR, MCF HDR, GREYC, Université de Caen Normandie
Corinne ALONSO, Professeur des Universités, LAAS, Université Paul Sabatier
Dir. de thèse : Mohamed MACHMOUM, Professeur des Universités, IREENA, Nantes Université
Co-dir. de thèse : Clovis FRANCIS, Professeur des Universités, CRSI, Université Libanaise
Co-enc. de thèse : DOUMIATI Moustapha, Enseignant-Chercheur, IREENA, ESEO (École Supérieure d'Électronique de l'Ouest)
Co-enc. de thèse : ELRAFEI Maher, MCF, CRSI, Université Libanaise

To ALLAH,
to my parents, my brothers and my sister:
Without you, this achievement would not have been possible, and I would not have been where I am today..

Acknowledgement

The present work was carried out as a cotutelle doctoral thesis between Nantes University (NU) and the Lebanese University (LU) in Beirut, involving specifically the IREENA laboratory (Institute of Research in Electrical Energy of Nantes Atlantique) and ESEO School of Engineering (École supérieure d'électronique de l'Ouest).

It is of great importance to me to express my gratitude to all those who contributed to the realization of this project. First and foremost, I would like to convey my deep appreciation to the management of the IREENA Laboratory, Nantes University, ESEO, and the Lebanese University for welcoming me into their research teams.

I extend my special gratitude to my co-encadrant Dr. Moustapha DOUMIATI, who not only warmly welcomed me to ESEO but also accurately guided me through every small step in my daily progress. His insightful comments and thought-provoking questions significantly contributed to the refinement of this manuscript.

I would also like to extend a heartfelt thank you to my co-director Pr. Mohamed MACHMOUM for his guidance and for facilitating the validation process of my work at the IREENA laboratory, despite the very limited time we had.

I would like to sincerely thank my co-director Pr. Clovis FRANCIS, for his unwavering support throughout this study. His guidance, expertise, and confidence in me have been invaluable.

Additionally, I am deeply grateful to my co-encadrant Dr. Maher ELRAFEI for his instrumental role in this journey, both in follow-up and insightful comments.

Thank you Pr.Farid MEIBODY TABAR (University of Lorraine) and Pr.Abdelhamid RABHI (University of Picardie Jules Verne) for agreeing to be the rapporteurs of this thesis dissertation. I thank also the members of the jury, Lecturer HDR Amrane OUKAOUR (Université de Caen Normandie) and Pr.Corinne ALONSO (Université Paul Sabatier).

A big thank to all of you.

Table of Contents

List of Figures

Acronyms

GHG	Greenhouse gas
PV	Photovoltaic
EMS	Energy Management System
HRES	Hybrid Renewable Energy System
Batt	Battery
FC	Fuel cell
SC	Supercapacitor
MPPT	Maximum Power Point Tracking
MF-STSMC	Model-Free Super-Twisting Sliding mode control
SoC	State of Charge
HESS	Hybrid Energy Storage System
DC	Direct Current
AC	Alternative Current
MG	Microgrid
P&O	Perturb And Observe
PI	Proportional Integral
PEMFC	Proton Exchange Membrane Fuel Cell
ESS	Energy Storage Storage
RES	Renewable Energy Source
SMC	Sliding Mode Control
STSMC	Super-Twisting Sliding Mode Control
RC	Resistance Capacitance
PWM	Pulse-Width Modulation
FL	Feedback Linearization
EFC	Equivalent Full Cycle
HIL	Hardware-in-the-loop
ADC	Analog-to-Digital Converter
DAC	Digital-to-Analog Converter
RTI	Real-Time Interface

General Introduction

PhD thesis framework

This thesis is a cotutelle between Nantes University (NU) and Lebanese University (LU) in Beirut, involving specifically the IREENA laboratory (Institute of Research in Electrical Energy of Nantes Atlantique) and ESEO school of engineering (École supérieure d'électronique de l'Ouest). The research work was conducted under the guidance of Professors Machmoum Mohamed and Francis Clovis, as well as Doctors Doumiati Moustapha and EL Rafei Maher. It is funded by Région Pays de la Loire, France, in the context of CAMI Project AAP RFI WISE "Smart Power Axis".

General context

"Today 770 million people live without access to electricity, mostly in Africa and Asia". The report [1] published by the international energy agency in 3 november 2022, highlighted the significant number of individuals living in homes without electricity. The Covid-19 pandemic, inflation and the energy crisis have worsened the situation by setting back global progress on universal access to electricity and making energy less affordable for households in developing countries. As per Legrand [2], a French industrial group, two main reasons account for this evaluation. Firstly, the deadlock in adopting traditional solutions like expanding electrical grids or relying on generators. Secondly, the limited utilization of renewable energies, which could be a viable solution for addressing the energy divide. In contrast, many countries, including France, have successfully achieved electricity access to almost their entire population [1]. However, this has led to a significant dependence on electricity, which presents challenges in terms of cost, quality, and reliability of the energy supplied. Therefore, one of the main concerns in the world is that some countries face the lack of reliable electrical grids for various reasons such as high infrastructure costs and limited utilization of renewable energies, while other countries that have met their electricity demand suffer from the enormous cost of energy transportation from power plants to consumers.

Another global concern is that today's electricity production and transportation sectors contribute to global warming, which poses a threat to the existence of humanity and the natural environment. Due to the fast growing in the energy demand, this energy-pollution dilemma pushes more than ever toward an energy transition in order to reduce greenhouse gas emissions. Governments, organizations, and individuals alike are working together to develop and implement sustainable energy solutions that can reduce carbon footprints and contribute to the fight against climate change. For instance, in order to implement a measure proposed by the "Convention Citoyenne pour le Climat", the article 147 of the Climate and resilience Law has introduced a mandatory offsetting of greenhouse gas (GHG) emissions related to domestic flights in France [3]. Another example is the Paris Agreement, adopted in 2015, establishes an international framework for climate action, requiring participating countries to take measures to reduce greenhouse gas emissions, enhance adaptation to climate impacts, and mobilize financing to support these efforts [4]. Renewable energy sources are at the center of the ongoing energy transition. In fact, the latest report from the International Energy Agency (IEA) indicates that renewable capacity additions are projected to expand by nearly 10% in 2021, setting a record. Furthermore, renewables are expected to surpass coal as the largest source of global electricity generation by 2025, signaling a shift in the global electricity sector towards cleaner and more sustainable energy options [5]. According to [6], renewable energy has experienced a significant upward trend in usage and in 2020, for the first time, renewable energy in Europe exceeded the production of electricity from fossil fuels. Solar, hydropower, and wind energy contributed 38% to the overall energy mix, surpassing the 37% share of fossil fuels (see Figure 1). This expansion has been fueled by technological advancements, increased investment, and favorable government policies, declining cost of renewable energy technologies.

In fact, cost-competitive renewables in comparison to higher fossil fuel prices are considered as one of the main driving agent towards the energy transition. International renewable energy agency (IREENA) estimates that, given the current high fossil fuel prices, the renewable power added in 2021 saves around USD 55 billion from global energy generation costs in 2022 [7].

One potential approach to integrate renewable energy resources into distribution grids is through the utilization of microgrids. Hence, microgrids are very interesting solutions to partially address these problems. A microgrid is a single controllable local power network that incorporates distributed energy sources (such as solar photovoltaics (PV), wind

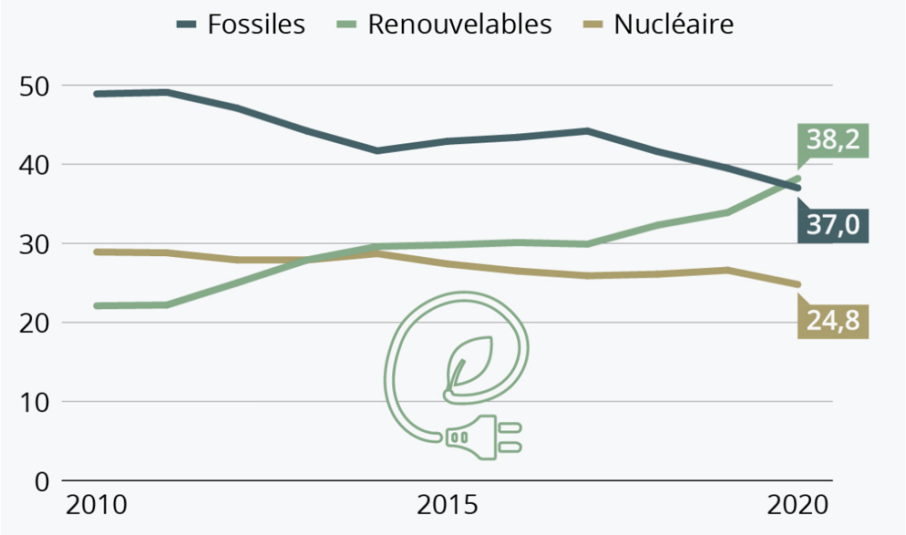

Figure 1 – Share of electricity produced in the EU-27 by energy type in %.

energy, diesel generators, fuel cells, wave energy, etc), energy storage systems, controllable distributed loads (such as households, commercial, industrial, etc), and advanced energy management systems (EMSs). It can operate independently or in conjunction with the utility grid [8]. Microgrids offer a lot of benefits in terms of technology, social impact, economics, and the environment. They can bring electricity to remote areas, reduce blackouts, and enhance overall energy efficiency. Furthermore, microgrids can lower system losses and provide auxiliary services to ensure the efficient operation of energy networks. This self-sustained energy system can cater to a specific geographic area, such as a college campus, hospital complex, business center, or neighborhood. A smart microgrid is a solution that ensures the sustainability of the electricity grid by providing intelligent and dependable power supply.

The popularity of microgrids can be attributed to several factors. Firstly, microgrids are known for their versatility in incorporating various energy generation methods, particularly renewable energy sources. This allows for a diverse and sustainable energy mix, reducing reliance on fossil fuels and promoting environmental sustainability. Secondly, microgrids are seen as a reliable solution for uninterrupted energy supply in areas with unreliable centralized power grids or vulnerable to severe weather events. This makes them an attractive option for regions prone to frequent power outages or facing extreme weather conditions, such as hurricanes or wildfires. Lastly, microgrids can help optimize energy usage, reduce energy waste, and lower electricity costs through efficient energy manage-

ment and utilization of local energy resources. This can result in substantial cost savings over time, making microgrids economically appealing to various stakeholders, including businesses, communities, and governments [9].

Microgrid technology has found extensive application across diverse practical domains, including islands [10], remote areas [11], industrial power systems [12], commercial buildings [13], residential homes [14], and university campuses [15]. This innovative technology has the potential to create highly reliable regional power systems with favorable economic outcomes and flexible power supply capacity [16].

The physical configuration or system architecture of a microgrid can be optimized through the selection of the optimal number, type, technologies, and dimensions of energy sources. This is generally done to reduce acquisition costs and potentially operational costs of the system, assuming a prior energy management policy.

Problem Statement

While microgrids are indeed ideal for integrating renewable energy resources, the intermittent nature of renewable energy sources and their connection to the power grid through power electronics converters can make the power grid more vulnerable and unstable; Meaning that energy generation is not consistent and varies depending on factors such as weather conditions. Moreover, the increased use of power electronics converters in the grid can decrease its inertia, making it more susceptible to frequency and angle instability, which are transient stability phenomena. This can pose a challenge to power grids that require a consistent supply of electricity [17].

To tackle this challenge, energy storage systems like batteries, flywheels, hydro-storage and hydrogen storage are utilized to store surplus energy for use during periods of low generation. By combining renewable energy sources with energy storage and backup generators, a microgrid can be created as a self-sufficient energy system that generates, stores, and distributes electricity from multiple sources. Given the operational redundancy of a microgrid, which allow for simultaneous production and storage of power using multiple devices, there is a need for a global control strategy to efficiently manage the power across the various components [18]. In DC microgrids, two main control objectives are necessary, DC bus voltage regulation and current or power sharing. Regulating the voltages is required to ensure a proper operation of connected loads, whereas an appropriate current or power sharing prevents the overstressing of any source [19].

The main focus of this thesis is divided into two main topics for stability, resilience and reliability purposes in a microgrid. The first topic involves the control of the DC bus and local units, while the second topic focuses on the energy management system. Both of these topics fall under the global control system of the microgrid. In the literature, there have been various proposed control and energy management approaches, each with its own objectives, advantages, and compromises depending on the system architecture. To date, no single technique or strategy has emerged as the universally optimal solution for all real-world situations, and considerable work needs to be done to compare different strategies.

In this work, a hierarchical control structure is proposed for a standalone hybrid renewable energy system (HRES) comprising a solar photovoltaic unit (PV) as the primary source, a hydrogen fuel cell (FC) as a standby source, and a hybrid energy storage system (HESS) composed of a battery (Batt) and a supercapacitor (Sc). The PV system operates at the maximum power point (MPP), while the FC and HESS serve as support and storage systems, respectively. The main objectives of the control structure are to maintain a stable, reliable, and resilient microgrid by ensuring the DC bus voltage stability at a desired level and robustness against disturbances, parameter variations, and uncertainties. The proposed control structure comprises two levels: the higher level control focuses on DC bus voltage stabilization, while the lower or local controllers address current tracking of the units. The control technique used is a model-free super twisting sliding mode control (MF-STSMC) with an anti-windup technique for saturation. The sliding mode feature provides robustness, while independence from the model increases resilience to parameter variations and high perturbations. Moreover, to establish a global control structure, a new energy management system (EMS) strategy is proposed. This strategy emphasizes not only on appropriate power sharing between the FC, Batt, and Sc, but also regulates the battery state of charge (SoC) within desired limits, while considering the trade-off between battery usage and hydrogen consumption costs. This is accomplished by building a gain-scheduled low-pass filter where the gain value of the filter is adjusted online to increase the flexibility of source utilization and regulate the battery SoC to ensure safe operation within the operating range. The EMS aims to optimize the performance of the system while ensuring efficient battery usage and hydrogen consumption, taking into account dynamic changes in system conditions.

Thesis structure

The present PhD thesis is written in 5 chapters. After this current general introduction, the first chapter initially addresses a general presentation of a hybrid renewable energy system (HRES), the principle of hybridization, the microgrid elements, its architectures and topologies. This is followed by a literature review on the most commonly used control and energy management strategies. A synthesis of the challenges and limitations of these strategies in the context of microgrid systems is provided. This allows us to position this thesis work and define the objectives of our research.

The second chapter introduces the microgrid architecture under study, including the main constructive elements such as the photovoltaic system, the fuel cell, the battery, and the supercapacitor. The chapter also presents the modeling of each of these components, as well as the modeling of the power electronic converters in two ways. The first one is the instantaneous modeling done for control testing purposes, and the other one is the average modeling used for energy management purposes.

The third chapter of the thesis focuses on applying the proposed control technique, the model-free Super-Twisting Sliding mode control, to the residential microgrid under study. The chapter includes a comparison of this control technique with two other candidate controllers, namely the feedback linearization technique and the first order model-based sliding mode controller. The comparison is based on numerical simulations, considering scenarios with high disturbances in photovoltaic energy production, load demand, parameter variations, and sensors noise. The results are thoroughly discussed and compared in the chapter.

In the fourth chapter, the concept of the frequency-decoupling based EMS is firstly reviewed, as the proposed strategy is an extended version of this approach. The fundamentals of the strategy are then introduced, including the general strategy steps such as data collection, data analysis, battery usage, and hydrogen consumption calculation for building the cost function. At the end of this chapter, a case study is chosen to evaluate the performance of the strategy, which involves a microgrid with four energy sources including PV panels, a fuel cell, and a storage system with two different dynamic units. Two other different EMS approaches were utilized to serve the comparison with the proposed technique.

The fifth and last chapter is dedicated to the implementation of the control algorithms and their validation on a real multisource system, which includes an emulated fuel cell

and two different types of energy storage systems with different technologies. However, it should be noted that the validation of the energy management system itself is outside the scope of this study. The chapter provides a detailed explanation of the transition from analytical models to Simulink blocks and functions, along with the presentation of the test bench and the experimental results.

In conclusion, a comprehensive summary of the thesis work is provided, followed by a discussion on potential future perspectives.

Thesis Contributions

The main scientific contributions in this research can be summarized as follows:

1. The use of a MF-STSMC loaded up with an anti-windup technique guarantying the following points:
   — A stable and reliable system operation with a consistent power quality.
   — Robustness against uncertainties and perturbations.
   — Chattering phenomenon limitation.
   — Controller prevention from wandering away when saturated.
2. Overall control hierarchical structure with two level (lower level: local control, higher level: global level control).
3. Battery SoC management within predefined target margins via a filter gain scheduling technique.
4. Cost optimization between battery usage and hydrogen consumption consisting of finding the optimal gain value, appropriate for SoC regulation, among a finite set of gains.

   In addition to the mentioned scientific contributions, this PhD thesis presents a valuable resource covering the modeling of the HRES for the control and the EMS development and their associated experimental validation.

Validation and publications

Theses results were the subjects of 3 international conference presentations and two published international review, all listed here:

- ◇ Kassir S, Doumiati M, Machmoum M, Elrafei M, Francis C. DC microgrid voltage stability by Model Free Super-Twisting Sliding Mode Control. In Proceedings of the 47th Annual Conference of the IEEE Industrial Electronics Society (IECON2021), Virtually in Toronto, Canada, October 10-13, 2021.
- ◇ Kassir S, Doumiati M, Machmoum M, El Rafei M, Francis C. Robust control and energy management in a hybrid DC microgrid using second-order SMC. In IEEE IECON 2022–48th Annual Conference of the IEEE Industrial Electronics Society, Brussels, Belgium on Oct 17, 2022, (pp. 1-6). IEEE.
- ◇ Kassir S, Doumiati M, Machmoum M, Francis C, Elrafei E. Energy management system based on cost optimization of battery aging and hydrogen consumption in a microgrid. International Review of Electrical Engineering 2022, I.R.E.E, PWP, vol. 17(4), pp. 346-359, DOI: https://doi.org/10.15866/iree.v17i4.21983.
- ◇ Mroueh M, Kassir S, Doumiati M, Francis C, Machmoum M. A time scale based energy management strategy for hybrid energy storage system in DC Microgrid. In47th IEEE IECON2021 2021 Oct 13.
- ◇ Imen Iben Ammar, Moustapha Doumiati, Sarah Kassir, Mohamed Machmoum, Clovis Francis, et al. New Nonlinear Control Based on Polynomial Approach for Islanded DC Microgrid Robustness and Voltage Stability. International Review of Automatic Control, 2022, 15 (5), pp.263. ⟨10.15866/ireaco.v15i5.22535⟩. ⟨hal-03925300⟩.

Chapter 1

Microgrid Overview

1.1 Introduction

The aim of this chapter is to provide an overview of Hybrid renewable energy systems, multi-source systems. In the first part, hybridizaton concept in energy sources as well as in storage system will be presented by describing various possible combinations between these sources and their complementarities. Additionally, a literature review on the components of the multi-source system used in this study. The subsequent part of the study will involve a critical analysis of the control and energy management techniques and strategies implemented in multi-source systems. A comprehensive discussion of the advantages and limitations of each of these approaches will also be provided.

1.2 Hybrid Renewable Energy System (HRES)

1.2.1 Hybridization: modality and importance

Hybrid Renewable Energy Systems (HRES) combine one or more distributed renewable energy sources, such as PV system and/or wind turbine (WT), Hydrogen system, diesel generator..) along with an energy storage system. This concept is usually performed to overcome the intermittent nature of the renewable energy sources [20]. It smooths out the energy production by providing energy during periods of high demand and storing excess energy during periods of low demand. The storage devices also provide an additional degree of freedom to better manage power and improve the efficiency and availability of the system [21]. Some studies integrate a diesel generator with a PV source, but it is not eco-friendly due to high CO2 emissions ([22], [23]). In contrast, other studies integrate a fuel cell system as a green energy source with 0% CO2 emissions ([13], [24]), making it a recommended solution to backup renewable sources while being environmentally safe [25]. Additionally, combining photovoltaic panels and wind turbines in a complementary

manner is also a feasible option [26] in a windy location in winter and sunny location in summer.

Hybridization is also a valuable strategy for energy storage systems. Since each storage device has its own characteristics, advantages and limitations, the hybridization of storage devices offers numerous benefits such as improved reliability, greater efficiency, cost savings and sustainability of energy production and consumption [27]. Among the most common storage devices, we have batteries, fuel cells and supercapacitors. Each type has its own internal dynamics that determine the instantaneous power it can provide or absorb without significantly affecting its lifespan. The Ragone diagram represented in Figure 1.1 provides an idea of the performance of electrical sources in terms of E (energy density or specific energy) and P (power density or specific power). Thus, batteries and fuel cells appear more as energy sources rather than power sources, unlike supercapacitors, which are more power sources with a relatively fast dynamics depending on their technologies. Hybrid energy storage systems can take various forms, as demonstrated in several recent studies. For instance, some authors have combined batteries and supercapacitors ([28], [29]), with such hybridization shown to extend the lifespan of batteries by alleviating constraints. Another example of hybridization can be found in [30], where a Hybrid Energy Storage System (HESS) of a battery, a fuel cell and a supercapacitor in a stand-alone power system configuration. This HESS is designed to store excess PV energy and provide backup power during outages.

1.2.2 HRES structure and components

The various classes of HRES structures are summarized in Figure 1.2. The diverse configurations and components available for HRES systems result in a wide range of HRES types that can be found. Based on its structure, the HRES can be classified into two main types [32]:

- Isolated or islanded systems: these systems offer more energy independence and are less constrained geographically, but are less tolerant of faults and require a dependable local power storage. These systems need to be wisely designed and sized in order to ensure high reliability and prevent power shortages.
- Grid connected systems: they are connected to the utility grid and can import and export power. They are less dependent on the storage, more reliable but are also more costly than islanded systems. They offer the advantage of synchronization with the grid, which means they can maintain a harmonized voltage and frequency

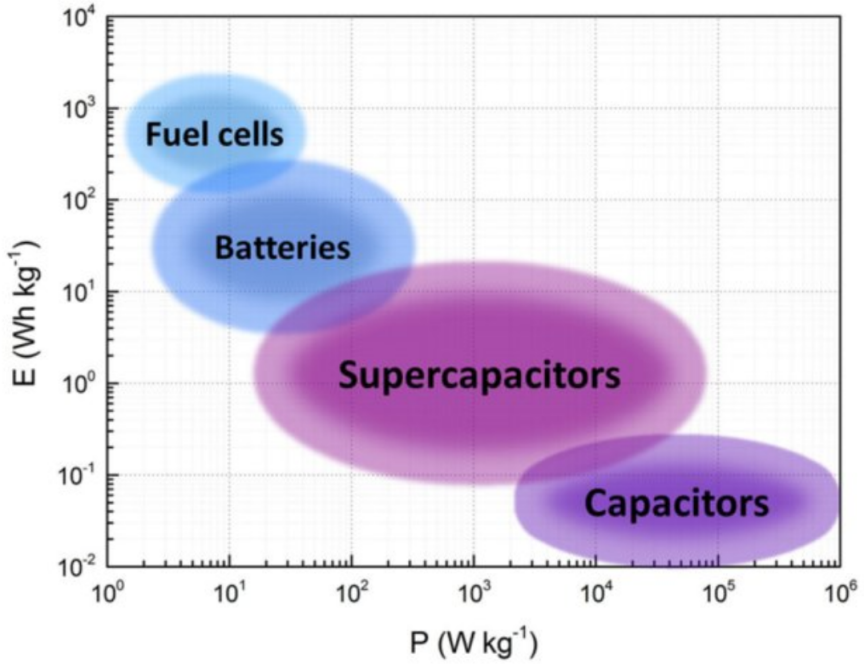

Figure 1.1 – Ragone plot [31].

with the utility grid. This synchronization allows for seamless power exchange between the grid and the system, enabling efficient import of power when needed and export of excess power generated.

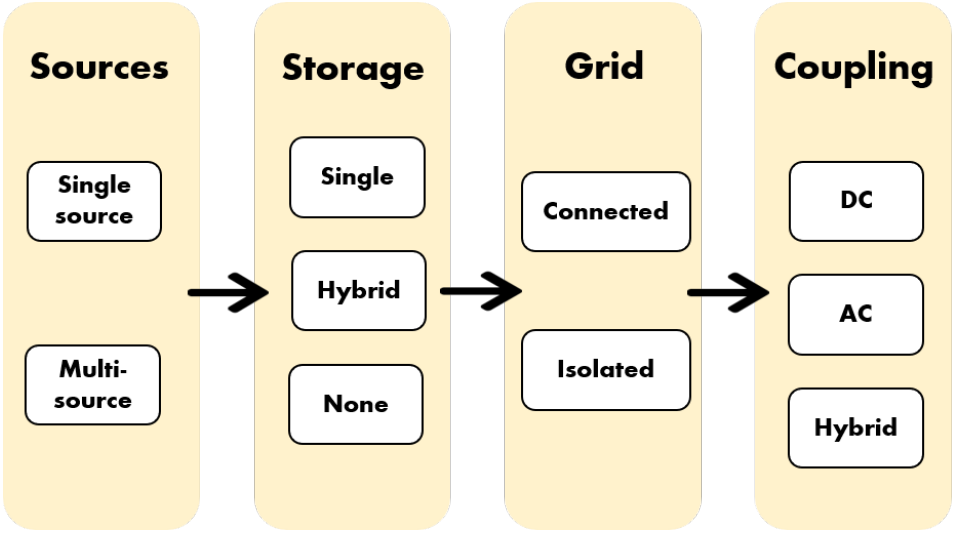

Figure 1.2 – Different HRES structure classes.

Indeed, the presence of multiple sources in a HRES enables the system to have various

configurations for electrical coupling, allowing for the sources to be linked via a DC, AC bus or both (Hybrid AC/DC) [33]. Each coupling type has its own advantages and disadvantages. Therefore, the choice between AC and DC microgrids ultimately depends on the specific application and its own conditions.

AC bus-coupled systems are capable of easily integrating with conventional utility grid or in islanded mode what makes them versatile. But they are more complex and require more components than DC bus-coupled systems, such as inverters and transformers, which results in higher costs and may require more maintenance. Synchronization is also necessary, and the system is more sensitive to the quality of the generated power. AC microgrids are commonly used in large-scale applications like cities or industrial complexes where AC is the standard power supply. They are also used in applications where there is a mix of AC and DC loads, such as commercial buildings with elevators and lighting systems that require AC power [34].

A major shift in the energy mix is expected to occur in the distribution networks, as AC transmission has been the norm until now, but **DC bus-coupled system** is gaining recognition as a promising solution due to technological advancements. With the increasing use of DC equipment associated with renewable energy sources, storage systems, and loads, the need for the fast integration of this equipment into the existing electrical network has become important. DC networks are becoming significant as they provide high controllability because it avoids issues related to the synchronization of Distributed Generators (DGs), reactive power flow control, frequency control, voltage sags and swells, flickering, harmonic currents and imbalances that are common in AC MGs [35]. They have a higher conversion efficiency due to the avoidance of conversions what makes them an ideal option to run high-performance electrical machinery. With fewer components required, the DC Bus-Coupled Systems are less complex and cost less than AC bus-coupled system. Moreover, they require less maintenance [36]. They are suitable for applications that require high power quality, such as hospitals and laboratories, and for applications where DC loads are dominant, such as electric vehicles and renewable energy systems [37]. However, the adoption of this type of technology may face some challenges. One major issue is the additional costs involved when using inverters. In additon, the reliability of the grid for AC loads may be affected by inverter failures, which could hinder the adoption of this technology. Indeed, changing the mindset of people and investors to embrace this new technology can be difficult. Some argue that transitioning from AC loads to DC loads or requiring an extra adapter in DC microgrids may be necessary. But, the majority of

loads today are electronic loads that can be directly plugged into DC sockets without the need for adapters or extra costs. This can help convince people to adopt this change since they can use their equipment in both AC and DC sockets.

Microgrid configuration

In terms of the physical arrangement of components within a microgrid, there are several possible topologies that can be used to establish a microgrid.

Single bus topology: the simplicity of this topology lies in its single DC bus design, which allows for all generators, storage systems, and loads to be linked to the same point. Additionally, this configuration is known for its low maintenance demands and cost-effectiveness, making it an attractive option. This topology can be seen in small-scale microgrids with limited distributed energy resources (DERs), such as residential or small commercial microgrids [37]–[41].

Radial topology: this topology builds on the single bus configuration by incorporating multiple DC buses. Each bus is utilized to connect generators, storage systems, and loads. This topology is one if the simplest and least expensive topologies, both to construct and for their protection system. There are two common configurations: series and parallel. The series configuration allows for two or more DC microgrids to be interconnected in series, however it has a difficulty of maintaining supply in the event of a fault occurring in the feeder. That means that a fault result in the loss of supply to a number of customers until the fault is located and cleared. The next level of reliability is given by a parallel configuration where microgrids are connected in parallel. In the event of a line fault only one of the feeder sets of cables will be affected, thus allowing the remaining parallel feeder to continue to supply the load. This topology retains its simplicity while supporting different voltage levels and improving reliability. However, it may encounter instability during the islanding mode. This topology is usually used in industrial or commercial microgrids with a single main power source, such as a large generator or a grid connection [37], [40], [42], [43].

Ring or loop topology: in this topology, all generators, storage systems, and loads are connected to a single DC bus in a loop configuration, which enables the supply of electricity through two different paths. This topology is more reliable than the previous configurations, as a fault in the DC bus can be overcome by operating in a single bus configuration. However, the main challenge with this topology is its increased complexity. Loop topology is commonly utilized for urban or community microgrids with multiple

DERs that are interconnected in a ring configuration [37], [40], [44], [45].

Meshed topology: this topology allows for the integration of radial topologies with a mesh configuration, resulting in a complex structure that provides improved reliability and flexibility when compared to the previous topologies. This is achieved by including one or more integrating rings. This topology is often seen in urban areas with multiple power sources and loads, where a mesh topology can provide enhanced resilience against disruptions or failures [37], [46]–[48].

Interconnected topology: unlike the previous topologies that relied on a single connection to the AC main grid, this topology provides increased reliability by allowing connections to alternative AC grids (two or more). This topology is known as interconnections and enables the system to be connected to multiple AC grids for added reliability. This topology is typically employed in smart city or community-scale applications, where multiple microgrids serving different areas or buildings are interconnected for optimized energy management and distribution [37], [40], [49], [50].

1.2.3 Microgrid elements

Energy sources are key elements of a microgrid system as they determine its autonomy and the technologies to implement. Several types of energy sources are currently used in microgrid application, and sometimes combined according to the concept of hybridization explained earlier. Each source has its own characteristics, advantages, and limitations. It also has its own internal dynamics that determine the instantaneous power it can provide or absorb without significantly affecting its lifespan. Among the most common are the Solar photovoltaic (PV) panels, wind turbines, hydrogen systems as renewable energy sources. Batteries and supercapacitors are primarily used for energy storage purposes to ensure the autonomy of microgrids. The microgrid desgin, and more specifically the choice of microgrid elements is highly dependent on several factors including the type of application, energy demands, resources availability, environmental impacts, cost and economic viability, etc.

Renewable source: PV system

Renewable energies, particularly solar photovoltaic (PV) panels have been largely integrated into power systems, mainly due to the fact that this technology is environmentally friendly and available almost everywhere. The PV device is designed to capture solar ra-

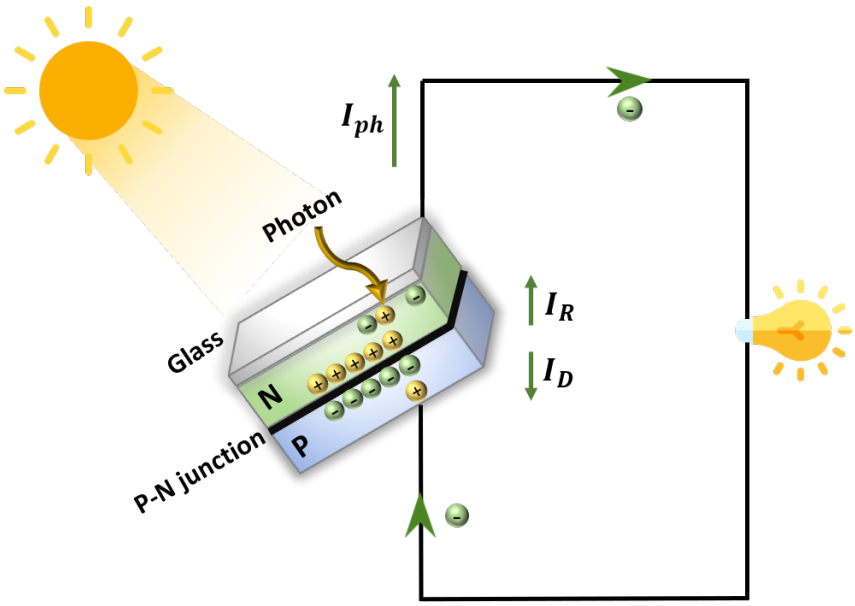

Figure 1.3 – Working principle of the PV cell.

diation and convert it into electrical energy. This process involves generating an electrical current by utilizing electrons that have been activated by absorbing the sun's radiation. The general working principle of the PV cell is shown in Figure 1.3, where the global current of the mobilized electrons is represented by I_{ph}. A portion of this current passes through the N-P layer junction, which is known as the diode reverse current I_D. The remaining current, I_R, represents the net generated power, not including any losses incurred through the various layers. There are many types of PV technologies available, with the majority being silicon-based, including mono-crystalline and poly-crystalline PV. Mono-crystalline PV offers higher efficiency due to its higher silicon purity, but it requires more processing, making it more expensive. On the other hand, poly-crystalline PV is less efficient but more affordable and easier to manufacture. Both types operate based on the same principles and phenomena, with differences in their efficiency resulting from the differences in silicon structure and purity.

Typically, the efficiency of commercially available PV panels ranges from 15% to 25%. Advances in solar cell technology have led to the development of more efficient types of panels, such as thin-film and concentrator PV panels, which can achieve higher efficiencies of up to 40% ([51], [52]). In terms of control, the amount of power generated by a photovoltaic (PV) system is influenced by various environmental factors, including temperature and solar radiation. Additionally, the output voltage of the PV cell affects the

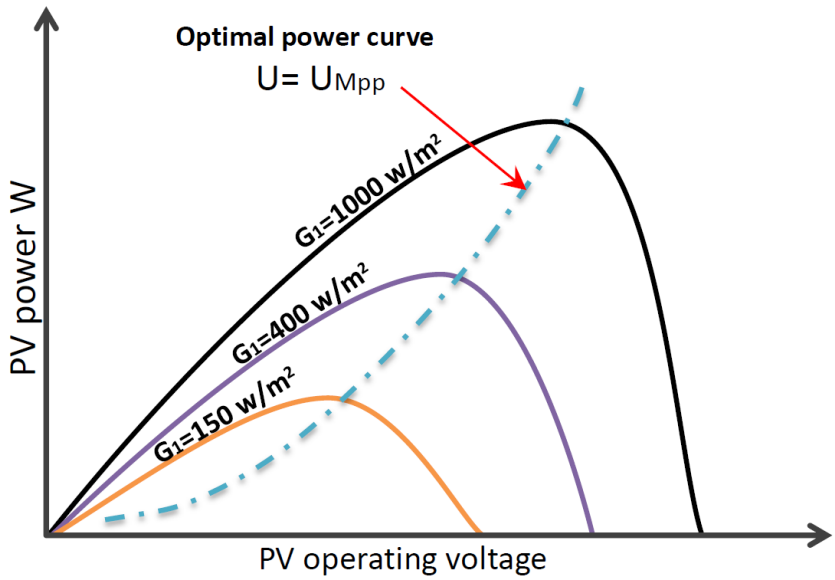

Figure 1.4 – Maximum power point tracking curve.

amount of power that can be extracted, as illustrated in Figure 1.4. For any given set of environmental conditions, there exists an optimal output voltage, referred to as the Maximum Power Point (MPP), at which the PV system generates the greatest amount of power. The optimal voltage curve is a 2D surface that identifies the optimal operating voltage (maximum power point voltage UMPP), based on irradiation and temperature. This curve can be determined through experimental measurements or provided by the manufacturer. Using measurements of irradiation G and temperature T, lookup tables can be used to set the PV voltage to the UMPP using the DC/DC converter. Various MPPT tracking algorithms and DC/DC converters have been proposed, reviewed, and compared in the literature [18]. Some examples of MPPT algorithms: Perturb and Observe (P&O) algorithm, Incremental Conductance (INC) algorithm , Fractional Open Circuit Voltage (FOCV) algorithm, Fractional Short Circuit Current (FSC) algorithm , Artificial Neural Network (ANN) algorithm [53].

The MPPT algorithm selected for this study is the Perturb and Observe (P&O) algorithm. It is one of the most widely used algorithms since it requires less sophisticated circuitry and is simple to implement in any system, regardless of its PV properties. Additionally, it can locate MPP with respectable accuracy and at a reasonable cost [54], [55]. The strategy of this algorithm is based on a slight variation (perturb) in voltage, i.e. $\Delta(V_{PV}^*)$, through the duty cycle of the PV converter u_{PV}. After that, $\Delta(P_{PV})$ is measured. If $\Delta(P_{PV}) > 0$, the PV module working point is closest to MPP and the subsequent vari-

ation takes place in the same trend as the preceding one; otherwise, if $\Delta(P_{PV}) < 0$, the obtained operating point of the system is far from MPP and the following variation occurs in the contrary direction. The procedure is repeated until MPP is attained. Afterwards, the system operates around that MPP [56]. Table 1.1 shows the behavior of the P&O algorithm in summary:

Table 1.1 – Behavior of the Perturb and Observe (P&O) algorithm.

Measurements	Voltage reference V^*_{PV}	Duty ratio u_{PV}
$\Delta(P_{PV}) > 0$, $\Delta(V^*_{PV}) > 0$	Rise	Drop
$\Delta(P_{PV}) > 0$, $\Delta(V^*_{PV}) < 0$	Drop	Rise
$\Delta(P_{PV}) < 0$, $\Delta(V^*_{PV}) < 0$	Rise	Drop
$\Delta(P_{PV}) < 0$, $\Delta(V^*_{PV}) > 0$	Drop	Rise

In addition to the diverse tracking algorithms documented in the literature, there exist two approaches for applying these algorithms. These approaches are the **Single Stage MPPT** and the **Double Stage MPPT**.

The control algorithm in **Single Stage MPPT** is designed to operate in a single control loop. The PV module's output voltage and current are input variables, and the converter duty cycle is the output variables. Because of the nonlinear characteristics of the PV module, this technique is simpler and less expensive to implement, but it may not always achieve the optimal power point.

Double stage MPPT, on the other hand, is a more complex control strategy that employs multiple control stages. According to [57], This approach not only rapidly and accurately tracks the maximum power point (MPP) even under dynamic weather conditions, but also significantly reduces power fluctuations around the MPP when subjected to both fast and slow changes in irradiation levels, which is an important feature for maintaining stable and reliable performance of photovoltaic systems. It does, however, necessitate more hardware components and is more expensive to implement. In this thesis, a double stage MPPT approach is proposed. Its control structure is depicted in Figure 1.5. In the initial stage, the actual current and voltage values of the PV module I_{PV} and V_{PV} are assessed in order to be sent to the MPPT searching algorithm. The MPP algorithm provides then a voltage reference V^*_{PV} that corresponds to the MPP. The second stage's controller keeps track of this reference. A PI controller that is proportional integral is suggested for this particular situation as there is no need for intense control demands.

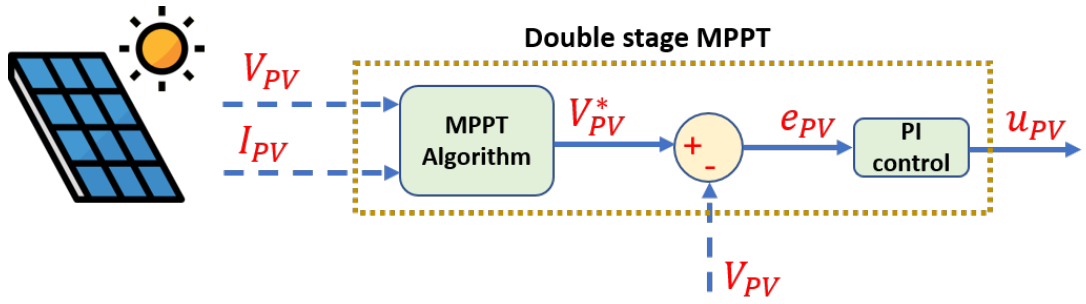

Figure 1.5 – Double stage MPPT.

Green source: Fuel Cell

Fuel cells work like batteries, but they do not run down or need recharging. They are a type of energy conversion technology. From a chemical reaction between hydrogen and oxygen, fuel cells generate electricity as long as fuel is supplied. They offer advantages such as high efficiency, zero emissions, and reliability. Fuel cells are being used in a wide range of applications, from powering vehicles and providing backup power to generating electricity for homes and businesses. As the demand for clean and efficient energy grows, the use of fuel cells is likely to continue increasing. Ongoing research and development may make fuel cells even more affordable and practical for widespread adoption. Figure 1.6 represents a recent strategic hydrogen energy road map for europe from 2015 to 2050.

The most common types of fuel cells that are found in literature are proton exchange membrane fuel cells (PEMFCs), alkaline fuel cells (AFCs) and solid oxide fuel cells (SOFCs)[59].

The alkaline fuel cell (AFC) was one of the earliest fuel cell technologies to be developed, utilizing non-noble metal electrodes and a liquid electrolyte. Despite being a well-established and cost-effective method, it is not capable of providing high hydrogen purity or supporting high current density.

The proton exchange membrane fuel cell (PEM FC) uses a solid proton exchange electrolyte and is more suitable for high current density, high power, and smaller-sized cells, making it an excellent option for compact and embedded applications. The PEM FC offers leak-free high hydrogen purity and more dynamic operation, but it comes with a higher cost and shorter lifespan compared to alkaline technologies. There are other highly efficient technologies, like solid oxide electrolysis, that are still in the research phase. Carmo et al. have conducted a comprehensive review and comparison of all these technologies [60].

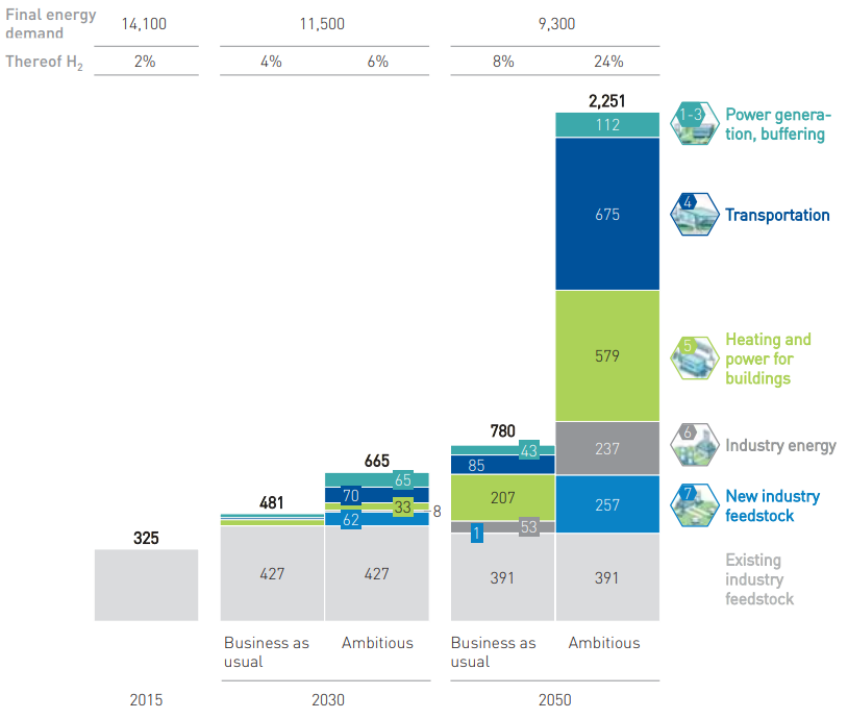

Figure 1.6 – Ambitious scenario for Energy demand and the Hydrogen deployment For Europe from 2015 to 2050 [58]

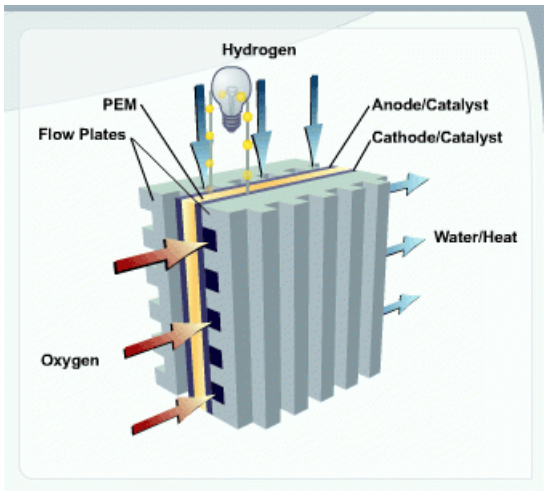

Figure 1.7 – PEM Fuel cell working principle [61].

In Figure 1.7, the working principle of a PEMFC is illustrated.

- At the beginning of the process, hydrogen atoms enter the fuel cell's anode.
- Next, the electrons in the hydrogen atoms are stripped away.

- As a result of the stripping process, protons are formed, which move through the fuel cell's membrane to the cathode.
- Electrons flow through an external circuit, generating electrical power.
- Finally, the electrons and protons combine at the cathode, producing only water and heat as byproducts.

Electrochemical storage system: Battery

A battery is a mechanism that stores electrical energy by converting chemical energy into electrical energy. It operates using two electrodes, namely, a positive electrode (anode) and a negative electrode (cathode), separated by an electrolyte. When the battery is connected to an external circuit, a chemical reaction occurs at the interface between the electrodes and the electrolyte, producing an electric current, and simultaneously causing charged particles (ions) to move through the electrolyte to balance the charge imbalance created by the electron flow. When a battery is charging, the electron flow reverses, and external power sources, such as chargers, force the electrons back into the anode.

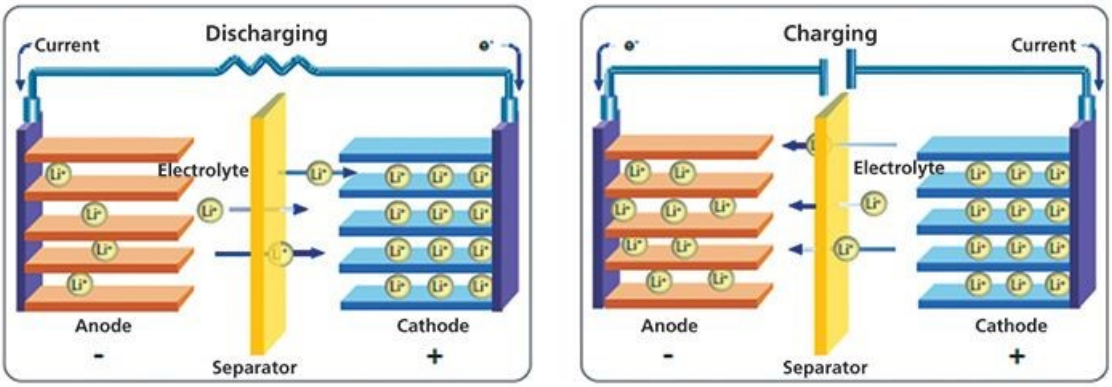

Figure 1.8 – Basic working principle of a battery [62].

Since the mid-1800s, Lead Acid batteries have been employed to store energy, however, in order to improve upon their energy storage capacity, durability, and cost-effectiveness, numerous alternative battery technologies have been developed. These different technologies display significant variation in terms of their energy and power densities, cycle-life, energy efficiencies, availability, and operating conditions. Among the newer battery types are Lithium Ion, Lithium Polymer, Nickel Metal Hydride (Ni-MH), Vanadium Redox (VRB), Nickel Cadmium (Ni-Cd), Sodium Sulfur (NaS), and Zinc Bromide [63] [64]. However, no single technology is universally applicable or optimal for every location or application.

Therefore, a careful case-by-case analysis is necessary to identify the best energy storage system option. A summary of key parameters for different batteries is provided in Table 1.2.

Table 1.2 – Comparison of different battery technologies [64].

Type	Energy Density (Wh/kg)	Energy Efficiency (%)	Power Density (W/Kg)	Cycle Life (Cycles)	Self Discharge (%/Month)
Lead-Acid	30 - 40	70 - 90	180	200 - 2000	3 - 4
Li-Ion	100 - 250	75 - 90	1800	500 - 2000	5 - 10
Li Polymer	130 - 200	70	3000	>1200	4 - 8
Ni-MH	30 - 80	70	250 - 1000	500 - 100	30
Ni-Cd	40 - 60	60 - 90	140 - 180	500 - 2000	10 - 15
NaS	150	80 - 90	120 - 150	2500	-
VRB	25 - 40	80	100 - 150	>16,000	<1
Zinc Bromide	70	70	-	1000	-

Electrical storage system: Supercapacitor

A supercapacitor, also known as an ultracapacitor or a double-layer capacitor, belong to the capacitor family but have very large capacities and it operates on a different principle than traditional capacitors. While traditional capacitors store energy in an electric field between two conductive plates, supercapacitors store energy electrostatically in the form of ions at the interface between a high-surface-area electrode and an electrolyte.

The basic structure of a supercapacitor in Figure 1.9 includes two porous electrodes, typically made of activated carbon, with a separator between them, immersed in an electrolyte solution. When a voltage is applied to the electrodes, ions from the electrolyte accumulate at the electrode-electrolyte interface, forming an electric double layer. This double layer acts as a "reservoir" of charges that can be quickly charged and discharged, enabling the supercapacitor to store and release large amounts of energy in a short amount of time [65]. Supercapacitors have several advantages over traditional capacitors and batteries, including high power density, rapid charging and discharging, long cycle life, and excellent performance in a wide range of temperatures [66].

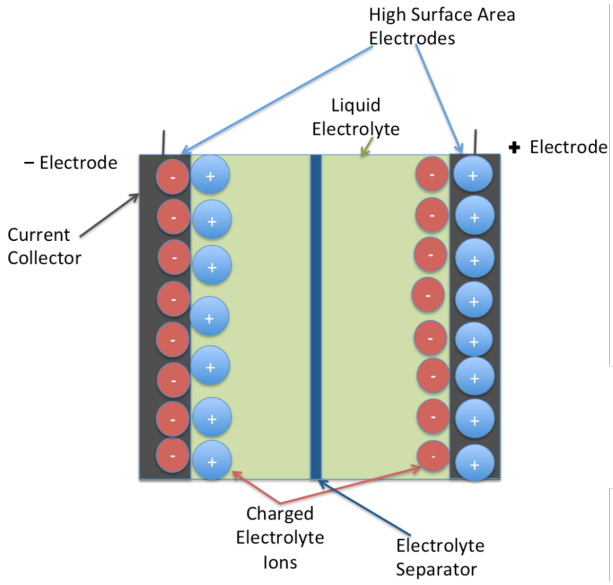

Figure 1.9 – Schematic of the internal composition of a supercapacitor [67].

MG case study It is worth mentioning that the objective of this thesis does not involve designing and sizing a microgrid from scratch. Therefore, we chose to focus on a specific residential application as a case study for control and energy management purposes and utilize an existing, appropriately sized microgrid that had previously undergone design and analysis. This served as the main subject of investigation in a thesis conducted at the IREENA laboratory in 2019 [68]. It is worth noting that in the study conducted by Mahjoubi et al. [68], the choice of each microgrid element was made with the following reasoning:

— Photovoltaic panels: They were chosen as the primary source of energy production because they are flexible, adaptable to different surfaces, emit no CO2, have a long lifespan, and require low investment and maintenance costs compared to other technologies.

— PEM Fuel cell: It was chosen as an auxiliary source of energy production to address the intermittent nature of photovoltaic panels. As the study aimed to achieve 0% of CO2 emission, the fuel cell seemed like an adequate technology for the system.

— Lithium-ion Battery storage: It was chosen as a storage technology due to its long lifespan, high energy density, and ability to ensure system autonomy. This helps to minimize the total cost of the system and the cost of energy produced.

— Maxwell Supercapacitors: They were chosen as a source of high power to satisfy the demand of the load in real-time. This is because sudden variations in power demand

require a significant need for power, which can be met by using supercapacitors as a source of high power.

For the microgrid sizing, the following concept was conducted in [68]. It is important to note that a frequency-decoupling energy management system technique was employed. In fact, the selection of cutting frequencies plays a crucial role in dimensioning, as each combination of cutting frequency values produces different power profiles that need to be distributed among the various organs while adhering to their dynamic constraints. The sizing of the different organs in the multi-source system is based on simulating the system's operation for one year. Using the load power profile together with the identified power profiles of the MG units, the costs and dimensions of the fuel cell, battery, and supercapacitor required for ensuring the system's autonomy can be calculated. Finally, a techno-economic optimization problem is formulated in order to generate the MG units size, taking into account energy constraints, including the power limitations of the considered energy storage systems (SC and Batt), and the regulation of their state of charge.

Power electronic converters

Typically, converters are employed to connect distributed generation systems in parallel with the grid or other power sources. However, it can be advantageous for the converters to operate in stand-alone mode when other sources are unavailable, ensuring a continuous power supply to critical loads by controlling the power flow and converting it into suitable DC or AC form. Each power electronics interface comprises a power converter with power semiconductor switches and primary electronic components like resistors, capacitors, inductors, transformers, and diodes, along with a control unit that manages power flow and voltage/current conversion. Depending on the application, the converter may need to support bidirectional power flow, as in battery interfaces, or unidirectional power flow from a source to a load. Different types of converters, such as buck converters, boost converters, bidirectional converters, and buck-boost converters, may be needed to perform various functions within a microgrid. In the microgrid under study, four DC-DC power electronic converters are required to connect each source to the DC bus. A boost converter is utilized to link the PV panel to the load, while another boost converter is used for the Fuel Cell. Unidirectional converters are employed for both the PV panel and the Fuel Cell, as they do not support reverse current flow. Additionally, two bidirectional converters are used to connect the storage system consisting of the battery and the supercapacitor, as they

need to be charged and discharged as required. The charging and the discharging cycles of the DC-DC power electronic converters are controlled by a voltage signal provided by the EMS block that adjusts the duty cycles of converters. Further details about the converters modeling are provided in Chapter 3.

.

1.3 Control and Energy Management System

The operational redundancy in the HRES where several devices can be used to produce and store the power simultaneously, the unknown fluctuating load demands, the variable electricity prices, and the Energy Storage System (ESS) operation schedules pose several challenges for energy management and coordination in Microgrids (MG). Several studies ([69]–[71]) have shown that the Energy Management System (EMS) plays a critical role in managing and monitoring energy flow in the MG to overcome these challenges.

However, due to the high randomness and intermittent behavior of Renewable Energy Sources (RES), non-linearity caused by interconnected power interfaces, harsh energy harvesting tasks, uncertain network parameters and component degradation over time, temperature, and malfunctioning, the MG becomes a time-variant system with varying parameters and uncertainties, which can exhibit complex and unpredictable behaviors that can be difficult to understand and manage without proper control. Therefore, designing an effective robust control is also crucial in order to achieve reliable and stable performance in Microgrids (MG) [72].

1.3.1 Control systems in microgrids

Control architectures in MGs

According to the literature reviews on microgrid control, control strategies are categorized into four main types: centralized, decentralized, distributed, and hierarchical frameworks, as represented in Figure 1.10.

Centralized Control: In a centralized control system, decision-making authority is held by a single entity or individual. Communication is the heart of the central control scheme. This scheme offers notable benefits, including enhanced visibility and control over the entire system. However, it also has several drawbacks, such as the vulnerability of a

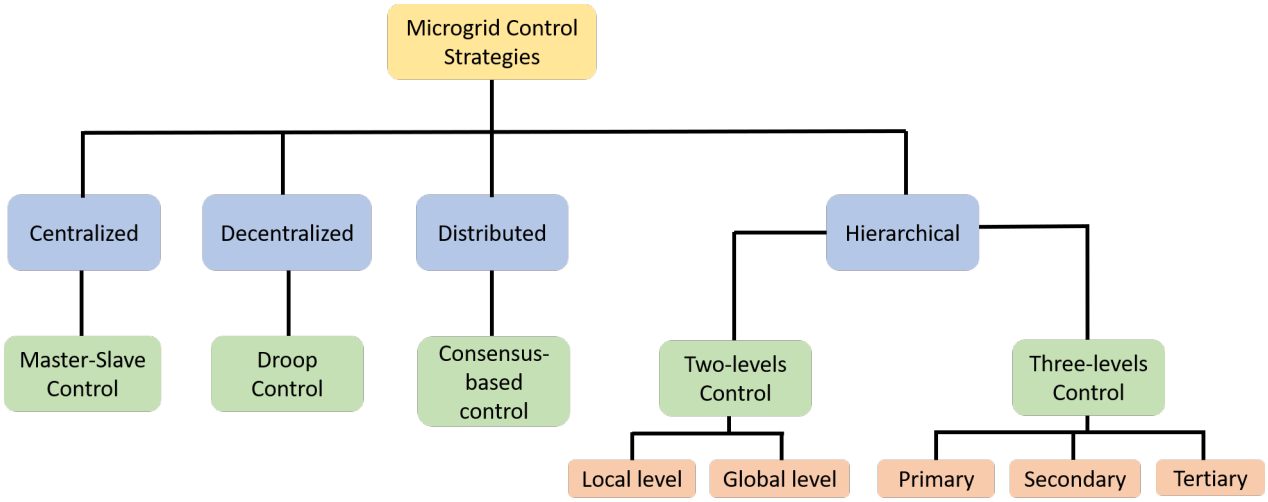

Figure 1.10 – Classification of MG control strategies.

single point of failure, diminished reliability, flexibility, and scalability and can also lead to bottlenecks and delays in decision-making [73], [74]. Master slave control strategy is a typical example of a centralized control scheme. In [75], the control strategy works as a specific converter is designated as the master, functioning as a Voltage Source Converter (VSC) and responsible for regulating the DC bus voltage. Meanwhile, the remaining converters act as Constant Source Inverters (CSI) and mimic the behavior of the master converter.

Decentralized Control: In a decentralized control system, decision-making authority is distributed among multiple entities or individuals. Each entity has some degree of autonomy and can make decisions independently [74], [76]. In droop control, the output power or frequency of a power source is regulated by adjusting its voltage or frequency in proportion to the load demand. The key idea behind droop control is to allow power sources to share the load in a decentralized manner, without requiring explicit communication or centralized coordination [77], [78].

Distributed Control: In a distributed control system, decision-making authority is also distributed among multiple entities, but these entities work together to achieve a common goal. The decision-making process is often more complex than in a decentralized system, as entities need to communicate and coordinate with each other. This scheme includes advantages of both centralized and decentralized schemes [74], [79]. It is immune to single point failure because the system can keep full functionary even if the failure of the some digital communication links.The main drawbacks of distributed control schemes are bus

voltage deviation, power tracking error and complexity of analytical performance. In [80], a distributed multiagent based algorithm is proposed to achieve SoC balance for DES in the DC microgrid by means of voltage scheduling.

Hierarchical Control: In a hierarchical control system, decision-making authority is organized into a hierarchy, with each level having some degree of control over the levels below it [74], [81]. There are two hierarchical control structures commonly used: two-level hierarchy and three-level hierarchy. In two-level hierarchy, the control system consists of decentralized low-level control for local control tasks and centralized or distributed high-level control for global control. On the other hand, in three-level hierarchy, each level is assigned specific tasks to perform within their respective time frames. A comprehensive review on the hierarchical structure for DC bus voltage control can be found in [82]. The paper discusses both typical structures for three-level and two-level hierarchical controls in detail.

It is important to note that there is no singular control architecture that can be used for all MGs. The strategy to be used depends on different factors like the particular model of the MG, its configuration, and the components used.

Overview of Control techniques used for MGs

Three important control considerations to define in a microgrid are the the following:

— **Reliability**: reliability refers to the ability of the microgrid to provide continuous power to its loads, even in the face of disturbances or disruptions.

— **Resilience**: Resilience is a related term that refers to the ability of the microgrid to quickly recover from disruptions and return to normal operation.

— **Stability**: Stability refers to the ability of the microgrid to maintain stable and consistent voltage and frequency (in AC MG case) levels, even in the face of changes in load demand or generation capacity.

Hence choosing the right control technique is considered as the most crucial task in control system engineering. This involves carefully studying the system's characteristics, such as the accuracy of the model, complexity of inputs/outputs, and type of parameters. It also involves considering dynamics like linear or nonlinear behaviors and ordinary or partial differential equations, as well as the computational time needed for real-world experiments [83].

In the field of microgrid control, linear control methods like PID have been widely adopted due to their simplicity, as evident from studies such as [84] and [85]. However,

linear control relies on a linearized model that is designed for a specific operating point, which can be a significant drawback when dealing with variable sources such as renewable energy and changing loads. To overcome this limitation, nonlinear theory has been suggested as a more effective approach that can provide a more comprehensive framework that covers all aspects of the microgrid, across a wide range of operating points [86]. In order to compensate for the strong non-linearities in microgrids, numerous recent studies have utilized non-linear model-based control methods to regulate DC bus voltage as evidenced in publications such as ([86]–[88]). One common control technique for these systems is the Lyapunov-based control technique ([89], [90]). In [91], a lyapunov control method is used to control the DC bus voltage of a microgrid dedicated for electric vehicle application. By choosing an appropriate Lyapunov function, it is possible to determine the stability of the system's equilibrium points without explicitly knowing the complete time evolution of the system behaviour. However, one of the primary limitations in Lyapunov analysis is that there is no general method of constructing Lyapunov functions and it is potentially very difficult to come up with suitable Lyapunov function candidates depending on several factors including the system complexity and the specific requirements of the control problem [92]. In addition, the use of a model-based controller without any adaptation can limit the controller's performance in some cases, especially when dealing with parameter uncertainties or variations over time. For instance, in [86], the authors employed a non-linear backstepping approach to stabilize the DC bus voltage and track the desired current references. However, their study did not investigate the robustness of the proposed controller against parameter variations or noise sensitivity. On the other hand, [87] proposed an adaptive feedback linearizing approach to maintain regulated DC bus voltage and performed sensitivity analysis for parameter variation and sensor noise in an islanded DC microgrid. However, adapting a model-based controller to deal with parameter variation is limited to the variation made in the model itself. Therefore, the controller may not perform well under large variations or in cases where the model is not accurate enough to reflect the system's behavior.

In recent times, advanced control algorithm as the Model Predictive Control (MPC) technique has gained popularity for controlling microgrids, owing to its numerous benefits. These benefits include its ability to provide a quick response to changes and its flexibility in handling non-linearities. In [93], the authors propose a fast model predictive control (MPC) based voltage control and power allocation optimization method for a hybrid energy storage system (HESS) in DC microgrids. The proposed method is validated by

simulation and hardware experimental results, demonstrating significant improvements than other methods. But it should be noted that the use of a Model Predictive Control (MPC) is associated with a significant disadvantage, which is the high computational effort required for its implementation ([94]–[96]). Another advanced control strategy used in literature is the H-infinity control. In [97], the author adresses the frequency stability of a hybrid microgrid consisting of renewable energy sources such as wind turbine generator and solar photovoltaic while using an H-infinity–based robust controller. But in fact, the H-infinity controller may have limited performance under system parameter variation, and involve solving complex optimization problems that require high computational resources, similar to the MPC controller.

Further control strategy that has gained attention during the past decades is the sliding mode control (SMC). Indeed, sliding modes are well known for their robustness properties and, belonging to the class of Variable Structure Control Systems, have been extensively applied in power electronics, since they are perfectly adequate to control the inherently variable structure nature of DC–DC converters. SMC has several advantages such as high reliability, robustness to parameters uncertainty and external disturbances, fast convergence rate and good transient response [98]. Further, its lower computational effort compared to strategies like MPC and its lower tuning effort comparing to strategies like fractional order PID control, makes it more easy applicable [99]. There are many types of SMC such as conventional or first order SMC, higher order SMC, terminal sliding mode control, integral SMC, etc ([100]–[102]). In [103], a conventional (First order) model-based SMC control is applied on a battery energy storage component. In fact, SM controllers require to operate at very high (ideally infinite) and variable switching frequency. A higher frequency allows for more precise control. When applying sliding mode control theory to real systems, the main challenge is dealing with chattering, which is an undesired phenomenon characterized by finite frequency and amplitude oscillations. In general, chattering can have negative consequences such as decreased control accuracy, increased wear of moving mechanical components, and higher levels of heat loss in electrical power circuits ([19], [104], [105]).

Positioning to the state of the art in system control

In order to keep the SMC advantages while limiting the chattering and the frequency leakage issue at the same time, huge efforts have been devoted in the last years to avoid chattering in SMC such as Qasi-SMC, using smoothing techniques (like approximative

continuous "sign" function, continuous high-order SMC, etc [106], being the Super-twisting SMC one of the most successful [107]. STSMC is a superior type of sliding mode control compared to others such as conventional SMC, terminal sliding mode control, and continuous terminal SMC. It has faster convergence rates with less chattering, is robust to external disturbances, and doesn't require precise knowledge of system dynamics or parameters, making it more practical for real-world applications [108].

In [109], a Super-twisting sliding mode controller is designed for a grid-connected photovoltaic system, while in [110] the authors proposed an adaptive approach to the Super-Twisting SMC for a differential boost inverter-based photovoltaic system. In addition, researchers such as ([111]–[113]) have utilized the fractional counterpart of the Super-twisting sliding mode controller to address control issues in DC microgrids. Over the years, Super-twisting sliding mode controllers have developed a well-established theory for both single-input single-output (SISO) and multiple-input multiple-output (MIMO) systems ([114]–[118]), to name just a few.

The control part of this study makes a significant contribution by utilizing a hierarchical control structure consisting of Super-Twisting Sliding Mode Controllers on two levels that are entirely model-free. Additionally, in order to prevent the actuators from exceeding their saturation limit, the proposed control algorithm incorporates an anti-windup technique. This approach is applied to a DC microgrid to stabilize the DC bus voltage and ensure robustness against disturbances and parameter variations without the need for online adaptation. The proposed control methodology offers a practical and effective solution for real-world applications of DC microgrids, which can improve their stability, reliability, and performance while reducing maintenance costs and increasing efficiency.

1.3.2 Energy management system in microgrids

The EMS in a microgrid is a multi-objective system that addresses in general technical, economic, and environmental concerns. The EMS aims to optimize the operation, energy scheduling, and system reliability in both modes islanded and grid-connected. To effectively control the microgrid, it's cruitial that the EMS is connected to all parts of the system, as depicted in Figure 1.11. A microgrid central controller (MGCC) and local controllers (LCs) control and coordinate the entire microgrid operation through a communication network [119].

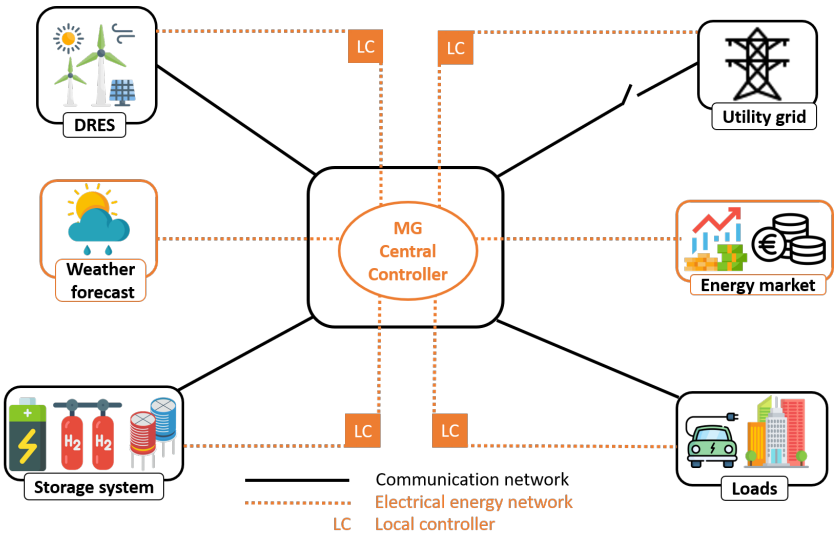

Figure 1.11 – Energy management system EMS-based microgird architecture.

In literature, different classifications for energy management system strategies are found. In a review by Ali, Zheng, Aillerie, *et al.* [120], the classification of these strategies is divided into two categories: **classical methods** (Mixed integer linear programming MILP, Mixed integer non-linear programming MINLP, Mixed integer quadratic programming MIQP, dynamic programming DP, model predictive control, non-linear programming NLP, stochastic and robust control methods..) and **artificial intelligence methods** (genetic algorithm, neural network, fuzzy logic, particle swarm...) [120].

Another common classification of EMS strategies found in literature is the division into two different classes : **rule-based methods** (deterministic like frequency sharing [121] or power limitation threashold [122] and fuzzy logic [91], [123], [124]) and **optimization-based methods** (Instantaneous optimization or global optimization like dynamic programming DP, model predictive control MPC, neural network, LP...) [125]. More specifically, optimization-based methods can be classified into two types: online and offline, each with its own advantages and limitations. Offline methods are flexible in implementation and typically do not require continuous computational efforts, as the optimization can be performed offline during system design or planning stages. This can reduce the computational burden on the system during real-time operation, resulting in faster and more reliable energy management decisions. However, offline energy management strategies require knowledge of the load profile to determine the optimal power distribution among the different components of the multi-source system. This reliance on load profile information makes real-time implementation impractical. As a result, these strategies were

often used for tasks such as sizing of hybrid systems or evaluating other real-time management strategies [126]. Indeed, recent advancements in artificial intelligence have made it increasingly feasible to accurately forecast load and weather (temperature, irradiance) profiles for extended periods of time [127], [128]. This implies that the limitations associated with offline energy management strategies, which relied on pre-known load profiles, are no longer considered as significant drawbacks.

Unlike offline optimization strategies, online strategies allows for real-time energy flow allocation, which requires significant computational resources and execution time [129]. Indeed, online optimization strategies do not require prior knowledge of the load power profile. However, the challenge lies in achieving a relatively small execution time for real-time implementation [130]. Nevertheless, knowing the shape of the load profile in advance can potentially improve the performance of the strategy.

The focus of the work described in [131] is to develop an energy management system (EMS) that considers the appropriate time scale for each component of an energy storage system (ESS) and includes a power rate-limiter for each energy source to ensure that it does not exceed its maximum power output. However, a limitation of this method is that it does not account for the state of charge (SoC) of the energy storage systems, which may compromise the stability of the overall system. The same limitation is also present in the work described in [86], where the author develops a classical passive filtering EMS that utilizes two low pass filters to distribute the power among energy storage system units. Although this approach offers benefits in terms of real-time power distribution between the battery and the supercapacitor, it does not take into account the state of charge of the energy storage systems.

The work described in [123] adopts an improved energy management system (EMS) approach based on frequency sharing, while also considering the state of charge (SoC) of the energy storage elements. This is achieved by incorporating additional distribution criteria that are determined online using fuzzy logic control. While the findings of the research in [123] successfully address the previous limitation by utilizing a rule-based strategy that is simple and quick to implement, other limitations were also identified. Specifically, with a rule-based approach, it is not possible to achieve an optimal solution. Additionally, the design of the controller is heavily dependent on the system's knowledge, and a large number of sources would require an impractically high number of rules to define. In the article [132], the author discussed a more sophisticated EMS approach that achieves the same objectives as the one that uses fuzzy logic, but does not rely on it.

This alternative strategy employs a flexible filtering method and considers the current state of the system, including the SoC of the storage component and the level of hydrogen stock. It determines a regulation criterion using a pseudo-optimization algorithm that is performed online. The adopted architecture was composed of FC, Batt and Sc but regrettably, no battery degradation neither hydrogen consumption cost were considered in the optimization study.

In [133], authors address the requirements to predict in real-time the driving cycles under the framework of a model predictive control based EMS for a battery/ultracapacitor HESS in electric vehicles. To account for the impact of battery aging on EMS performance, an online optimization problem was integrated to optimize energy distribution between the Batt and the Sc. In this model predictive control based EMS, no vehicle model was involved in the optimization solution. Instead, a neural network approach was executed. However, there was no offered explanation for this choice. As a result, the online optimization problem was not model-based but data-driven. This approach is considered time-consuming since it demands a labor-intensive data for training the algorithm.

Several studies, for instance, [124] and [134] use dynamic programming algorithm to structure their EMS. In [134], authors deal with an optimal EMS in wind-based standalone microgrid where a new day-ahead integrated control based on dynamic programming is proposed to enhance the battery's lifetime and optimize the power flow. This strategy suffers from a series of pitfalls, first, a perfect knowledge of the decision problem to be solved is necessary, second, significant computing time is required, what makes the real-time implementation out of reach. On top of that, the more sources we add, the more complexity is increased to reach the optimal solution.

The study conducted by Bukar et al. [135] presented a rule-based EMS approach for microgrid application using queuing theory. The primary aim of the optimization problem was to reduce energy costs and increase the reliability of the system. The authors concluded that their approach achieved these objectives successfully.

Positioning to the state of the art in EMS

In [68], a simple filtering EMS is applied on a residential microgrid consisting of a PV, FC, Sc and Batt, with FC taken as a reinforcement system for the PV renewable source, this EMS does include battery usage and hydrogen consumption cost for solving an offline optimization problem and then determine the optimal filter frequency value to consider, but not the filter gain. It is worth noting that in both work [132] and [68], a serious

criticism of SoC regulation can be noticed when the regulation was done according to a fixed constant reference not an interval, what limits the power capability of the energy unit. In fact, considering a fixed SoC reference is a very stiff objective. Garcia in [136] established an EMS based on Fuzzy logic in order to satisfy the energy requested by load and maintain the battery SoC and the hydrogen level between certain target margins while trying to optimize the utilization cost and lifetime of the ESS. This work was done on a stand-alone HRES of WT, PV, hydrogen and battery hybrid system. However, in this study the hydrogen system (FC coupled with an electrolyser) was used as a storage system not as a backup source. A switch between two EMS was made, the first EMS determines the power of the Batt and FC based on cost optimization where each one of the storage system (Hydrogen or battery) was used at a time, whereas the second one is a fuzzy logic based EMS launched only when the Batt SoC and H_2 level are out of range.

Based on the discussed literature work, this work introduces a new energy management system approach based on a gain scheduled filtering. The proposed EMS ensures power balance within the microgrid and achieves two key objectives: managing the State of Charge (SoC) of the battery within predefined margins and optimizing costs of battery and hydrogen by determining the optimal gain value for SoC management. This EMS approach complements the work of Joshi et al. [137], who developed an innovative method for Supercapacitor SoC regulation. However, their approach has a limitation in that it works only when the battery SoC is within safe operation limits. If limits are exceeded, the battery must be shut down, which could have severe consequences. Our proposed approach addresses this issue by focusing only on battery SoC regulation, while Joshi et al.'s approach focuses only on SoC regulation. Combining these two approaches enables us to create a more comprehensive and effective EMS approach.

1.4 Conclusion

A microgrid system offers an appealing solution for clean power outage, reducing dependence on traditional power grid infrastructure, and promoting sustainable and environmentally friendly energy practices, while maximizing energy utilization, increasing system efficiency, and enhancing system resilience to fluctuations in energy availability and demand. It can be designed with different architectures, topologies, energy resources, and storage units, depending on factors such as the application, load requirements, available energy resources, cost considerations, and environmental considerations. Reliability,

resilience, and stability are three key factors must be ensured through a proper control structure in a microgrid. To effectively coordinate between the different energy sources and storage units in a microgrid, a well-designed energy management system is essential. The energy management system can be tailored to meet various objectives, such as power sharing, operational cost reduction, units degradation mitigation, and fuel consumption optimization. Control and energy management systems are multidimensional problems that often require compromises between objectives. As seen in the literature, numerous control and management strategies are proposed for different microgrid architectures, each with its own advantages and limitations. Choosing the appropriate strategy is a critical task in microgrid design. In this chapter, after reviewing various control and management strategies from the literature, our motivation for choosing the proper control and energy management system strategy for the studied microgrid is explained in detail.

The following chapter focuses on modeling the microgrid elements, including PV panels, fuel cells, batteries, supercapacitors, and power electronic converters.

Chapter 2

Microgrid Modeling

2.1 Introduction

It is well known that the successful implementation of any application requires a well-designed multi-source system to support it in terms of its topology, number of sources, characteristics, and power interfaces. As a result, the design of the microgrid architecture is a critical aspect of the overall project. In fact, the control and the energy management strategies for the microgrid depend on this determined architecture. In the following section, the considered microgrid architecture is presented. The next section outlines an appropriate modeling methodology for the energy production and storage units, including their associated power electronic converters.

2.2 Microgrid architecture

The studied microgrid system is designed to be used in islanded mode to meet the energy demands of an isolated habitat. In Figure 2.1, the general schematic of the applied DC microgrid architecture is presented, it includes:

— **Energy production units**: The primary energy source is a renewable one, represented by the photovoltaic panels. They primarily supply the load in this microgrid. In other words, the PV panels covers the major part of the demanded load during the sunny periods of the day. In addition to the PV system, an auxiliary energy production unit consisting of a fuel cell acts as a reinforcement agent. It provides energy support to the system when the primary generation source (PV) is not able to meet the increasing load demand due to low efficiency periods or during night hours.

— **Energy storage units**: The hybrid energy storage system used includes a battery and a supercapacitor. The storage elements act as compensators for any lack or excess in electrical production. The battery and supercapacitor have different re-

sponse times, making the complementary dynamics of this MG suitable for both fast, medium and slow response demand. It also helps ensuring that energy targets are met to the greatest extent possible.

— **Power electronic converters**: DC-DC converters are used as interface units between the common DC bus and energy sources on one side and the storage systems on the other. Boost converters are used for both of the power sources, while bidirectional converters are chosen for the storage units because they have the ability to charge and discharge based on the microgrid's loading conditions and the power produced by the sources.

— **DC bus**: All components in the DC microgrid are interconnected through the common DC bus that is considered as the backbone of this network. It is equipped with a filtering capacitor that mitigate the fluctuations in the voltage level and ensures a stable and constant DC voltage.

— **Loads**: A controlled current source fed by a residential current profile serves as load model.

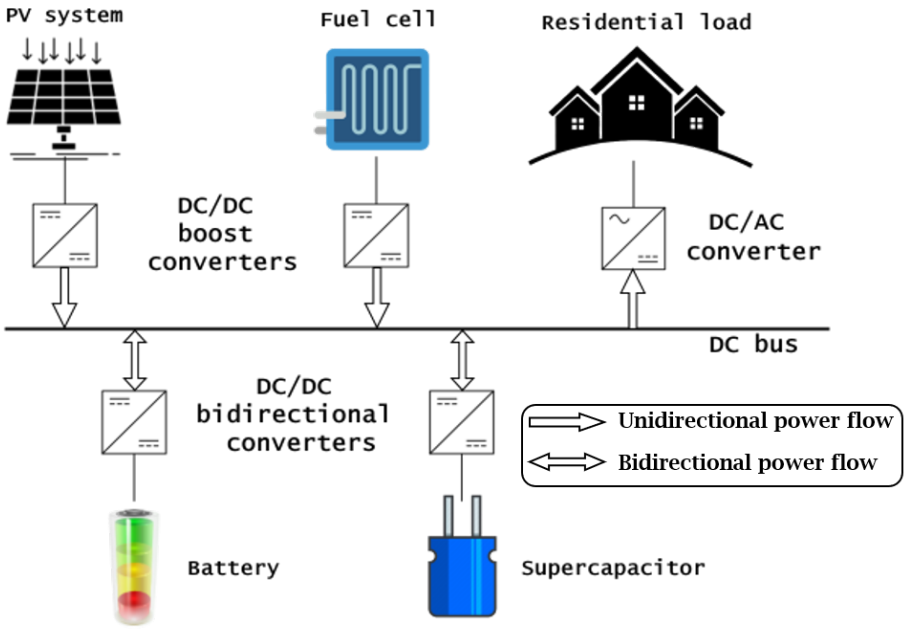

Figure 2.1 – Microgrid system architecture.

2.3 Modeling of the electric MG system

2.3.1 Photovoltaic system

Solar Cell modeling Depending on the level of accuracy required and the computing resources available, different modeling assumptions are employed in literature such as the single diode model, the Bishop model, and the Direct–Reverse model. In [138], the authors have reviewed various published works on electrical equivalent models for PV.

The **single diode electrical model** is chosen for the case study application of this thesis work. It is widely used due to its simplicity and and computational efficiency. It can be used to simulate the behavior of PV cells under different conditions, making it a popular choice for both academic research and industrial applications ([139], [140]). Some studies have explored a PV model featuring multiple diodes, while others have examined how the accuracy of the model is affected by series or parallel resistance. The single diode electrical model of a PV cell describes the electrical behavior of a PV cell as a single diode connected in parallel with a current source, known as the photocurrent, which represents the ideal current generated by the cell in response to incident light. The diode represents the non-ideal behavior of the PV cell. Additionally, this model also includes the series and shunt resistances that account for the ohmic losses in the cell. Figure 2.2 shows the one-diode electrical model of the photovoltaic cell where:

— I_{ph} is the photocurrent generated by solar irradiance (A)
— I_D is the current passing through diode (A)
— I is the output current of solar cell (A)
— V is the output voltage of solar cell (V)
— R_{sh} represents the loss of dissipative effect of the cell (Ω)
— R_{se} represents the junction resistance (Ω)

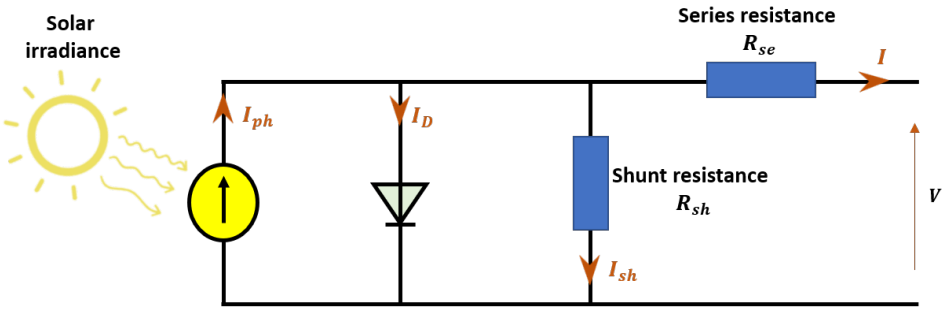

Figure 2.2 – One diode equivalent circuit of a PV cell.

The characteristic equation of the real cell is then given by [18], [141]:

$$I = I_{ph} - I_D - I_{sh} \tag{2.1}$$

Bypass current I_D

The current on the diode is calculated according to the Shockley diode ideal equation I_D, modeled as follows:

$$I_D = I_0[(e^{\frac{(V+R_{se}I)q}{nKT}} - 1] \tag{2.2}$$

Where:

- n is the ideal factor representing how closely the diode follows the ideal diode equation which depends on the manufacturing, in many cases n is assumed to be approximately equal to 1.
- I_0 = Reverse saturation current of the diode (A)
- q = electric charge [1.60e-19C]
- k = Boltzmann constant [1.38e-23 J/K]
- T = the absolute temperature of the p–n junction (K)

Shunt current I_{sh}

The shunt current passing through parallel resistance is easily computed according to Kirchhoff's circuit laws:

$$I_{sh} = \frac{V + R_{se}I}{R_{sh}} \tag{2.3}$$

Replacing equations (2.2 and 2.3) in the initial Eq.2.1 establishes a unique model of the solar cell represented by Eq.2.4 as follows:

$$I = I_{ph} - I_0[(e^{\frac{(V+R_{se}I)q}{nKT}} - 1] - \frac{V + R_{se}I}{R_{sh}} \tag{2.4}$$

The static model of a PV system is based on the relationship between voltage (V) and current (I). The electronic nature of PV systems does not typically exhibit a transient dynamic model. Some studies have included capacitors on the output of the PV, but most research has found that a static model is sufficient.

Another common PV cell model used in literature is the **Bishop model**. It integrates an avalanche mechanism into the single diode model, as illustrated in Figure 2.3. This mechanism accounts for the reverse characteristics of the PV cell, which are influenced by the current flowing through the shunt resistance R_{sh}. The current term in this model

comprises of an ohmic component and a nonlinear multiplication factor [142], as depicted in Equation 2.5.

$$I_{\text{cell}} = I_{\text{ph}} - I_0 \left(e^{\frac{(V_{\text{cell}} + I_{\text{cell}} R_s)}{AV_T}} - 1 \right) - \frac{(V_{\text{cell}} + I_{\text{cell}} * R_s)}{R_{\text{sh}}} \left(1 + a * \frac{(1 - (V_{\text{cell}} + I_{\text{cell}} R_s))}{V_{br}} \right)^{-m} \tag{2.5}$$

Equation 2.5 in the Bishop model establishes a relationship between the output current and voltage of a PV cell. In this equation, a represents the portion of the current that is associated with ohmic behavior related to avalanche breakdown, m denotes the exponent that characterizes the avalanche breakdown, and V_{br} represents the junction breakdown voltage [142].

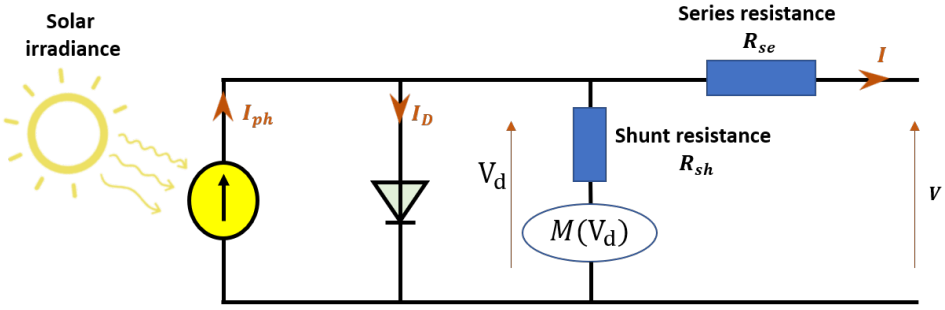

Figure 2.3 – Circuit diagram of the Bishop model.

Constitution of a photovoltaic generator PVG

A Photovoltaic Generator (PVG) is created by connecting multiple photovoltaic cells in a series or parallel configuration. The structure of a PVG typically comprises three main components: the cells, module, and array as illustrated in Figure 2.4. The solar cells, which are the primary element of a PVG, are responsible for absorbing energy from the sun. The PV module serves as a housing for the solar cells, while the PV array is the arrangement of interconnected PV modules which produces the desired voltage output. To enhance the performance of the PVG, protection diodes are added in series to prevent reverse current flow and parallel by-pass diodes are added to limit reverse voltage across terminals and minimize production loss [141], [143], [144].

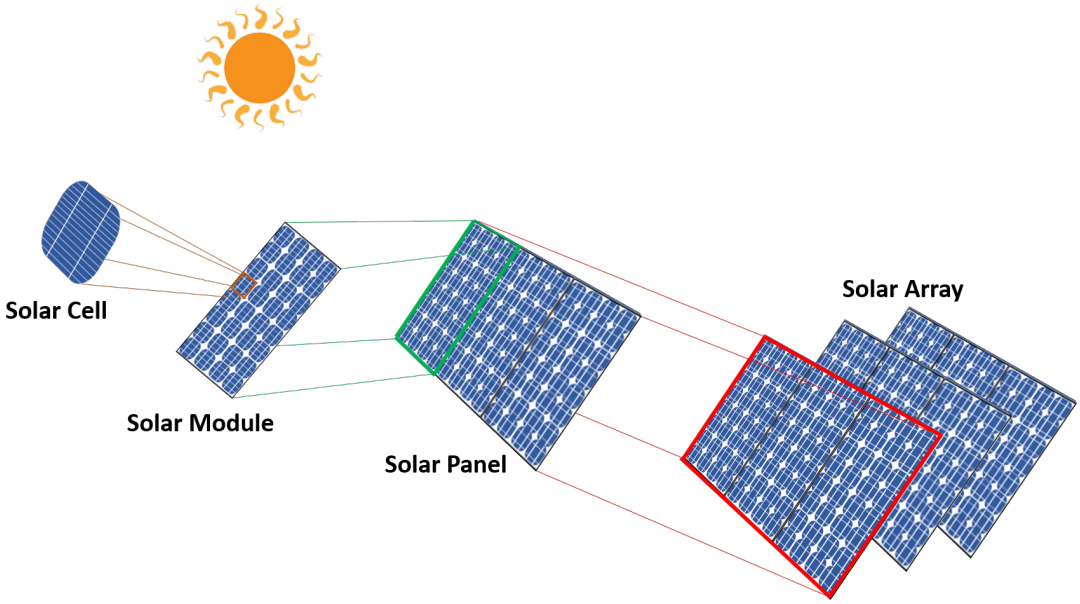

Figure 2.4 – The basic building blocks of a PV solar array.

2.3.2 Fuel cell

According to [145], equivalent circuit models for PEMFCs can be divided into two categories: passive models and dynamic models. Passive models represent the operating behavior of the PEMFC in the stand-by state and can be used to evaluate potential performance and degradation while the fuel cell is in stand-by mode. Dynamic models represent the operating behavior of the PEMFC under the output electric power state, and must include a voltage source and inherent losses. These models can be used to optimize the performance, transient response, and efficiency of power conversion systems that use PEMFCs as the power source. Figure 2.5 presents the dynamic model adopted in this work. It is represented by an electrical equivalent RC (Resistance-Capacitance) circuit. It is considered to be more advanced than a static model since it takes into account the double-layer charging effect inside a fuel cell. It includes equations that describe how the fuel cell's performance changes over time. It considers the resistive and capacitive properties of the cell's components, which allows the model to more accurately predict the cell's response to changes in its operating conditions [87].

The fuel cell stack's electrochemical behaviour can be represented by the following equations:

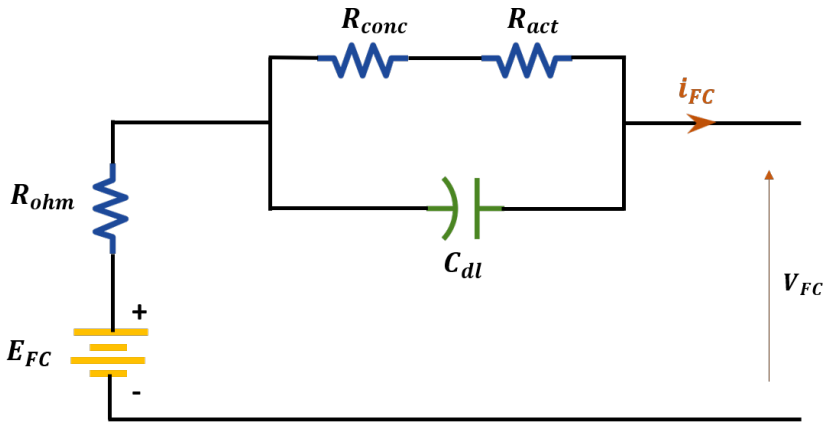

Figure 2.5 – Equivalent circuit of the double-layer charging effect inside a fuel cell.

$$V_{FC} = E_{FC} - V_{ohm} - V_{act} - V_{conc} \tag{2.6}$$

$$\frac{dV}{dt} = \frac{1}{C_{dl}} i_{fc} - \frac{1}{\tau} V \tag{2.7}$$

— E_{FC} is the open circuit voltage.
— R_{ohm} is the resistance of the fuel cell membrane. It models the losses due to the electrons transfer in the electric circuit and the movement of ions through the electrolyte and membrane.
— C_{dl} is the equivalent capacitor due to the double-layer charging effect.
— R_{conc} is the concentration resistance. It models the losses caused by the reduction in concentration of the reactant gases.
— R_{act} represents the activation losses that arise due to slow kinetics of reactions.
— V_{FC} is the fuel cell stack output voltage.
— V represents the dynamical voltage across the equivalent capacitor.
— τ is the fuel cell electrical time constant defined as $\tau = (R_{act} + R_{conc})\, C$

The open circuit voltage E_{FC} can be defined as follows:

$$E_{FC} = n_s \left(E_{\text{Nernst}} - V_{act_{drop}} \right) \tag{2.8}$$

where n_s is the number of cells in series in the stack, E_{Nernst} is the thermodynamic potential of the cell, and represents its reversible voltage or Nernst potential and $V_{act_{drop}}$ is the activation voltage drop [146].

$$\begin{aligned} E_{\text{Nernst}} =& 1.229 - 8.5 \times 10^{-4} \times (T - 298.15) - 3.33 \times 10^{-3} I_{fc}(s) \frac{80s}{80s+1} \\ &+ 4.31 \times 10^{-5} \times T \times \left(\ln\left(P_{H2}\right) + \frac{1}{2}\left(P_{O2}\right) \right) - 3.33 \times 10^{-3} I_{fc}(s) \frac{80s}{80s+1} \end{aligned} \tag{2.9}$$

$$\begin{aligned} V_{act_{drop}} &= -0.948 + T \\ &\times \left[2.86 \times 10^{-3} + 2 \times 10^{-4} \ln(A) + 4.3 \times 10^{-5} \ln\left(C_{H_2}\right) + 7.6 \right. \\ &\left. \times 10^{-5} \ln\left(C_{O_2}\right) \right] \end{aligned} \tag{2.10}$$

where P_{H_2} and P_{O_2} are the partial pressures (atm) of hydrogen and oxygen, respectively. T is the cell's absolute Kelvin temperature and A is the cell's active area (cm^2). The terms C_{O_2} and C_{H_2} are the oxygen concentration at the cathode membrane/gas interface (mol/cm^3), and the liquid phase concentration of hydrogen at the anode/gas interface (mol/cm^3), respectively. They can be obtained as follows [147]:

$$C_{O_2} = \frac{P_{O_2}}{5.08 \times 10^6 \exp\left(\frac{-498}{T}\right)} \tag{2.11}$$

$$C_{H_2} = \frac{P_{H_2}}{1.09 \times 10^6 \exp\left(\frac{77}{T}\right)} \tag{2.12}$$

Fuel cell aging it refers to the gradual decline and reduced performance of a fuel cell over time. Several factors contribute to this process, including catalyst degradation in the electrodes. The catalyst undergoes physical and chemical changes over time, which hampers its effectiveness and overall fuel cell performance. Additionally, exposure to harsh operating conditions like high temperatures, humidity, and contaminants can cause the fuel cell membranes to degrade. To address these challenges, researchers are actively studying ways to enhance the durability and longevity of fuel cells, making them more viable for long-term applications [148]. There have been numerous research studies focused on developing fuel cell aging estimation models to assess the rate of fuel cell degradation and predict its remaining lifetime. These models aim to provide valuable insights into the health and performance of fuel cells over time. In [149], an online evaluation model for fuel cell voltage degradation considering four operation modes is introduced to predict fuel cell aging. While in [150], an aging prognosis model of PEMFC is proposed in different operating conditions based on the Backpropagation (BP) neural network and evolutionary

Table 2.1 – Comparison of electrical equivalent battery models.

S. No.	Battery model	Features
1	R_{int} model	Model is static.
2	Thevenin electric model	Does not consider the dependency of state of charge.
3	Second order RC Thevenin model	Model does not consider the parameters like temperature and capacity.
4	Accurate electrical equivalent model	Model considers the battery life time.

algorithm. In [151], the authors developp an online natural aging estimation algorithm, coupled with an Electrochemical Impedance Spectroscopy (EIS)-based diagnostic algorithm, to refine detection features extraction during Solid Oxide Fuel Cell (SOFC) stack operation and to predict its Remaining Useful Life (RUL) [151].

2.3.3 Hybrid Energy Storage System

Battery model

In order to emulate the electrochemical behavior of the battery, different models are proposed in the literature. Depending on the level of detail or precision required, the model may be more or less complex. In [152], a review of various lithium-ion battery equivalent circuit models are presented. Table 2.1 gives the different Electrical equivalent circuit models available in literature along with its important features [153].

In Figure 2.6, the first order RC model used for our case study of the battery is shown. This dynamic model has been widely used for its good characteristics in terms of accuracy and complexity as in [154], [155], [156].

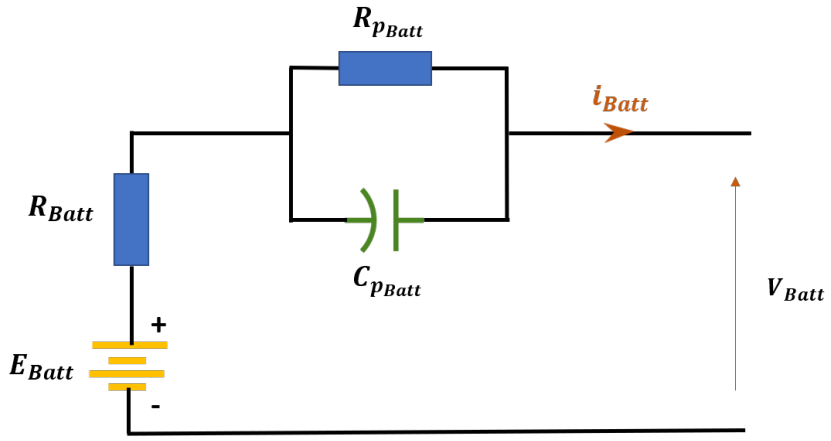

Figure 2.6 – Equivalent circuit of the battery.

— E_{Batt} is the open circuit voltage of the lithium-ion battery which usually varies nonlinearly with SoC.
— R_{Batt} is the ohmic resistance of the lithium-ion battery which describes its internal resistance.
— $C_{p_{Batt}}$ is the polarization capacitance that represents the polarization of the metallic electrodes.
— $R_{p_{Batt}}$ is the polarization resistance due to the contact of the electrodes with the electrolyte .
— i_{Batt} is the lithium-ion battery current flowing to the load direction.
— V_{Batt} is the terminal voltage of the battery which can be directly measured from a voltage sensor.

It should be noted that batteries can be affected by corrosion and degradation, which are the two main reasons why they can stop working properly. In fact, deep charge/discharge cycles tend to decrease the battery's lifespan, which is defined by the number of cycles it can undergo before it no longer functions. The end of life is generally defined by a decrease of 20% in capacity compared to its nominal value.

State of Charge (SoC) is a measure of the amount of energy remaining in a battery expressed as a percentage of its total capacity. It is one of the most important parameters for batteries. The value of the SOC varies between 0% and 100%. If the SOC is 100%, then the cell is said to be fully charged, whereas a SOC of 0% indicates that the cell is completely discharged. However, using the battery within its entire range of operation can cause it to age prematurely. Therefore, in practical applications, a balance between

battery performance and lifespan is taken into consideration, so that the battery is operated within the ideal parameters recommended by the manufacturer [6] (see Figure 2.7). Some of the commonly used methods for SoC estimation in the literature are Coulomb Counting, Voltage-Based Methods, Kalman Filtering, Extended Kalman Filtering (EKF), Artificial Intelligence (AI) and Machine Learning (ML) Methods, and Adaptive Methods. The choice of the estimation method depends on the specific application, accuracy requirements, available data, computational resources, and other factors. However, coulomb counting and voltage-based methods are the most commonly used in practice due to their simplicity and relatively low computational requirements.

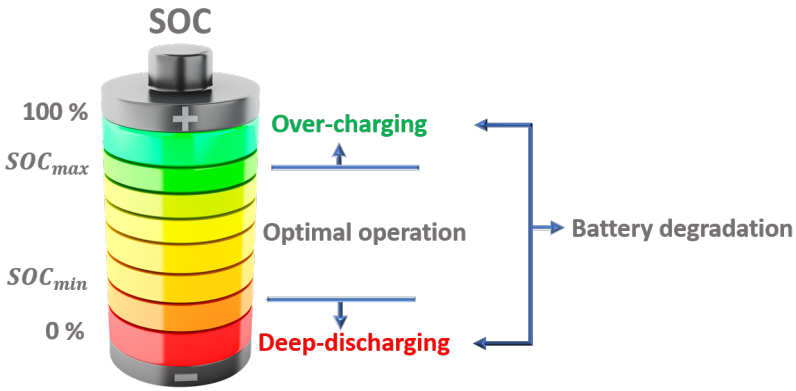

Figure 2.7 – Battery optimal operating range.

The Coulomb counting method, as described in [157], involves measuring the discharging current $I(t)$ of a battery and integrating it over time to estimate the State of Charge (SoC) while taking into account the battery cell capacity Q_n and the previously estimated SoC values.

$$\mathrm{SOC}(t) = \mathrm{SOC}(t-1) + \frac{I(t)}{Q_n}\Delta t \tag{2.13}$$

Indeed, the accuracy of the Coulomb counting method for SOC estimation can be influenced by various factors, as mentioned in [157]. These factors may include temperature, battery history (such as aging or previous charging/discharging cycles), discharge current, and cycle life. An updated approach, known as the modified Coulomb counting method, has been proposed in [158] to enhance the accuracy of the original Coulomb counting method. The modified method utilizes a corrected current to improve the accuracy of the SoC estimation process. The corrected current is determined based on the discharging

current of the battery and is found to have a quadratic relationship, as supported by experimental data. The calculation of the corrected current is performed using the following formula:

$$I_c(t) = k_2 I(t)^2 + k_1 I(t) + k_0 \tag{2.14}$$

where the constants k_1, k_2 and k_3 are obtained from experimental data in practical applications. The State of Charge (SoC) estimation in the modified Coulomb counting method is determined using the following equation:

$$\mathrm{SOC}(t) = \mathrm{SOC}(t-1) + \frac{I_c(t)}{Q_n}\Delta t \tag{2.15}$$

Based on experimental results [158], it has been observed that the accuracy of the modified Coulomb counting method surpasses that of the conventional Coulomb counting method. In summary, the standard Coulomb counting method is straightforward to implement since it does not involve any adjustments for efficiency or capacity loss. In contrast, the modified Coulomb counting method requires additional computations to consider these factors, which can make the SOC estimation algorithm more complex.

The main and most challenging objective is to identify the aging mechanisms in batteries, which are further complicated due to the interplay of multiple factors, such as the ambient environment and charge-discharge modes, giving rise to various aging effects.

The mechanism of battery aging can be divided into two distinct components: cycle aging and calendar aging. These two components describe different types of degradation caused by different battery usage scenarios. Calendar aging occurs as a result of battery storage, while cycle aging is associated with the impact of charging and discharging cycles.

There are numerous factors that affect the cycle life of batteries, including temperature, state of charge (SOC), changes in SOC (ΔSOC), charge and discharge current, charging and discharging cut-off voltage, and charging methods, among others. The aging mechanisms in cells can generally be classified into two types: capacity decrease and increased impedance or inner resistance during storage and cycling. To evaluate the level of aging in lithium-ion batteries, several indicators or concepts have been developed.

The most commonly utilized indicator in literature is the state of health (SOH), while [159] typically defines battery capacity loss and SOH interpretation through the use of relative capacity indicators. The following provided equation Eq. 2.16 can be used to

calculate relative capacity of a cell.

$$C_{\text{relative}} = \frac{C_{\text{n}_\text{p}}}{C_{n_0}} \tag{2.16}$$

Battery aging Different methods can be used to estimate degradation in lithium-ion batteries, depending on the specific performance attribute being studied (e.g., capacity fade or resistance increase), the type of battery life being considered (calendar or cycle life), and the overall modeling approach. Some approaches rely on electrochemical models that are based on theoretical understanding of the chemical reactions causing battery degradation, while others take a more empirical approach by establishing relationships between battery aging and experimental data. Both approaches have limitations, with electrochemical models being complex and theoretical, and empirical models requiring substantial data and being valid only under specific conditions. Semi-empirical models aim to combine the advantages of both approaches by incorporating theoretical principles with experimental data to estimate model parameters. These models are simpler than electrochemical models and can be applied to a wider range of conditions than empirical models [160].

One of the most popular semi-empirical aging model, used in [131], [161]–[163], is employed for the estimation of lithium-ion battery aging. It is described by the equation below:

$$\begin{aligned}
&\Delta_{Batt} = \frac{1}{Q_{Batt}} \int_0^t F\left(SOC_{Batt}\right) G\left(I_{Batt}\right) I_{Batt} dt \\
&F\left(SOC_{Batt}\right) = 1 + 3.25\left(1 - SOC_{Batt}\right)^2 \\
&\begin{cases} G\left(I_{Batt}\right) = 1 + 0.45\frac{I_{Batt}}{I_{\text{Battnom}}} & \text{if} \quad I_{bat} > 0 \\ G\left(I_{bat}\right) = 1 + 0.55\frac{|I_{\text{Batt}}|}{I_{\text{Battnom}}} & \text{if} \quad I_{Batt} < 0 \end{cases}
\end{aligned} \tag{2.17}$$

where Q_{Batt} is the entire life battery capacity and $I_{Battnom}$ the nominal current of the battery.

Supercapacitor model

An ideal capacitor is considered to be a linear, passive component in electrical circuits, but a real-world capacitor has an equivalent series resistance (R_s) representing the combined resistance of the electrodes and electrolyte and a parallel resistance that interprets the self-discharging phenomena caused by the overall leakage through various mechanisms

(R_p) as depicted in Figure 2.8. This model is proper to catch high-frequency dynamics, for example, during fast charge/discharge cycles or high-level fluctuating power pulses, it is the most commonly used SC model in the literature ([164],[165]).

Numerous models have been developed in the literature with the aim of adding more dynamics and complexity to the models, thereby enhancing their ability to represent dynamic behavior over extended periods of time. Figure 2.9 demonstrates an equivalent model developed by Zubieta and Boner, which is applicable to a wide range of power electronic applications. The three RC branches in the model, namely the immediate, delayed, and long-term branches, represent the SC characteristics on distinct time scales. Each branch has unique time constants to allow for easy measurement during various periods. The immediate branch consists of a voltage-dependent nonlinear capacitor c_v, a constant capacitor c_0, and a constant resistor R_i and is used to capture transient behavior over seconds. The delayed branch is suitable for emulating SC behavior in the range of minutes and consists of a constant capacitor (C_d) and a constant resistor R_d. Finally, to represent SC behavior over long time scales (typically higher than 10 min), the long-term branch is used, consisting of a constant capacitor (C_j) and a constant resistor (R_j). As shown in Figure 2.10, a dynamic model of SC can be represented in the frequency domain by a combination of a series resistor ($\mathrm{R_s}$), a bulk capacitor (C), and n number of parallel RC networks, utilizing electrochemical impedance spectroscopy. Figure 2.11 shows the use of transmission line modules to emulate distributed capacitance and electrolyte resistance as determined by porous electrodes. Generally, the fidelity of the model increases with a higher number of RC networks, but at the cost of computational power [166].

Supercapacitor aging Supercapacitors are known as they have a prolonged lifespan, typically enduring hundreds of thousands to millions of cycles, depending on their design and usage conditions. Supercapacitor aging is influenced by various factors, including an increase in Equivalent Series Resistance (ESR), loss of capacitance, cycling fatigue, temperature effects, and voltage overstress. It is important to note that the rate of supercapacitor aging depends on factors such as material quality, operating conditions, and specific design characteristics [167]. In [168], a supercapacitors degradation model is developed using current ripple rate temperature and cycles number. This aging model can be used in adaptive energy management based on the micro-grid power fluctuations mitigation in variable temperature conditions. It is important to note that accurately predicting the remaining useful life of supercapacitors is crucial to optimize their efficiency, prevent

equipment damage, and facilitate timely replacement. In [169], authors developed an enhanced forecasting model for predicting the capacity of supercapacitors. This optimized model combines an Extreme Learning Machine (ELM) with the heuristic Kalman filter (HKF) algorithm. An additional research study [170], focuses on predicting the remaining useful life of supercapacitors. The work offers a comprehensive analysis of both model-based and data-driven approaches utilized in this prediction process. It examines the distinctive features of these various methods and provides valuable insights into potential future developments.

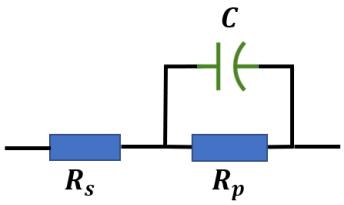

Figure 2.8 – Simplified model.

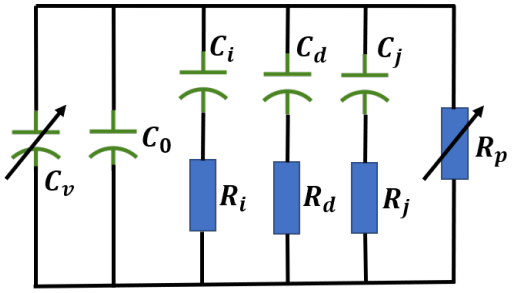

Figure 2.9 – Zubieta and Boner developed mode.

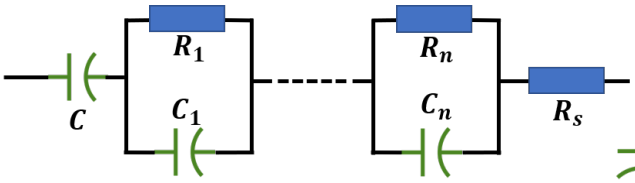

Figure 2.10 – Modified version of Zubieta and Boner developed model.

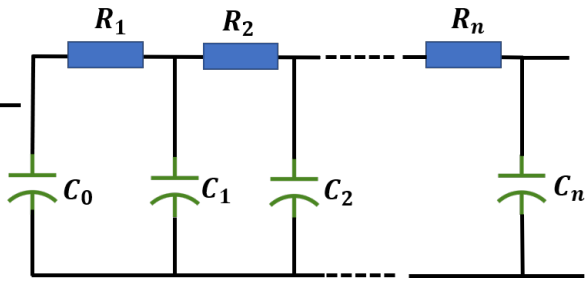

Figure 2.11 – Transmission line model.

2.3.4 Power Electronic Converters

As specified at the beginning of this chapter, two types of converters will be used, bidirectional current type converters for reversible sources and unidirectional boost type converters for the irreversible sources, which are the PV system and the fuel cell. In this thesis, two forms of converter modeling are employed, the instantaneous and the average modeling technique.

Instantaneous modeling

Initially, it was determined that the instantaneous model was the most suitable for simulating and accurately evaluating the performance of the control structure. This is due to the fact that it allows for a more precise representation of the electrical signals present in the converter.

Boost converter The boost converter, depicted in Figure 2.12, consists of an inductor, a switching element, a diode that prevents reverse current flow towards the energy source and a capacitor on the high voltage side.

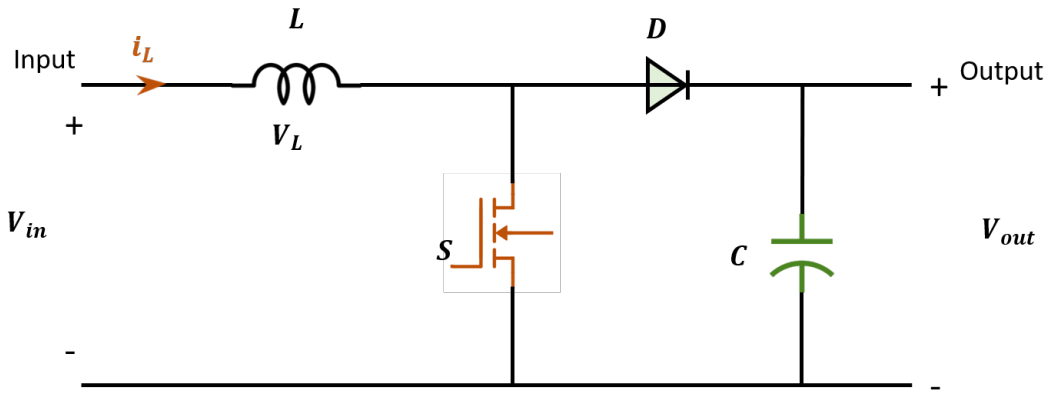

Figure 2.12 – The instantaneous model of a boost converter.

Bidirectional converter The bidirectional converter, as shown in Figure 2.13, allows for power transfer in both directions, from the storage element to the DC bus and vice versa. The structure of the converter comprises an inductor on the low voltage side, a capacitor on the high voltage side, two MOSFET switches, S_1 and S_2, and two complementary diodes, D_1 and D_2. Depending on the sign of the current, two operating modes are available, i.e. charge mode and discharge mode. In charge mode, the flow of current from the DC bus to the storage system is enabled through the actions of switch S_1 and diode D_2, acting as a buck converter. In discharge mode, switch S_2 and diode D_1, acting as a boost converter, facilitate the transfer of energy from the storage element to the DC bus.

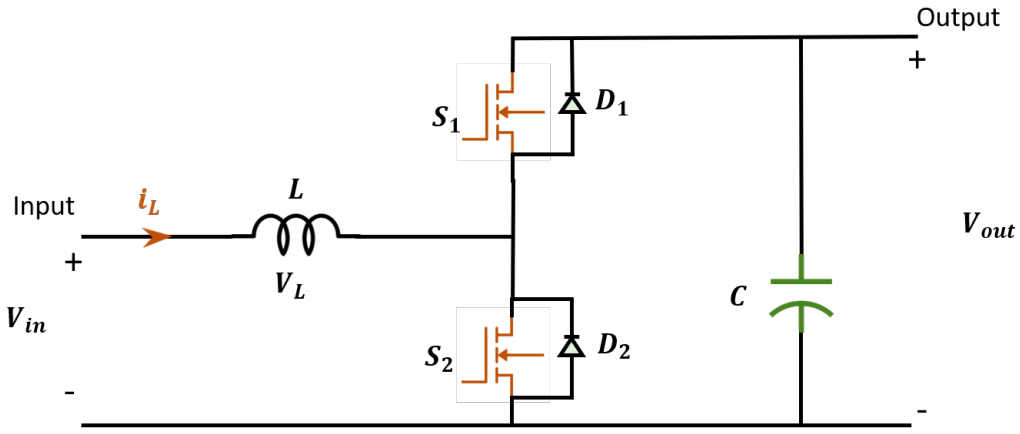

Figure 2.13 – The instantaneous model of a bidirectional converter.

Now the MG system being studied is definitely categorized as a complex system due to its multiple components, the non-linear interaction between them, and the hierarchical design of its control system. Since all control and regulations actions in the MG system need to be performed through the DC-DC converters, it is crucial to choose the appropriate converters model approach to highly serve the application study in terms of accuracy and computational perspective.

According to a study published in [171], the utilization of the instantaneous approach for converter models, which involve the operation of real switching devices, results in improved accuracy in terms of dynamic response and loss modeling. However, the smaller sampling time associated with the switching frequency of converters restricts the ability to conduct long-term simulations. Additionally, the simulation of a complex system, with realistic load and external source input profiles spread over a wide time span, may result in a high computational burden, requiring a significant amount of memory space in the hardware which may obstruct the simulation. To find a good balance between having a detailed model and quick simulation, the average modeling method is used for both boost and bidirectional converters in energy management system simulation. This is important due to the requirement of extended simulation periods in the EMS.

Average modeling

This approach eliminates the use of real switching devices, and the converters are controlled directly through duty cycles rather than pulse width modulation. By eliminating

the need for the Pulse-Width Modulation (PWM) block, the sampling time is increased, thus the efficiency of the simulation is faster and improved, which fits well with the requirements. Although the average modeling approach may not capture all the dynamic effects of the converter, it is often used in energy management system simulations due to its balance between model accuracy and computational efficiency. This is particularly important for EMS simulations that require extended simulation periods. The average models of the converters are depicted in the Figure 2.14, and it can be observed that the typical switches of an instantaneous converter (MOSFET or IGBT) are substituted by controlled current and voltage sources to simulate the behavior of the converters.

For the case of the DC-DC boost converter, the differential equation of the current passing through the inductor can be expressed as:

$$L\frac{di_L}{dt} = V_{in} - (1-u)V_{out} \tag{2.18}$$

where u is the duty cycle fed to the MOSFET S and i_L is the current passing through the inductance L. The average modelling technique typically involves analyzing the steady-state behavior of the converter. Therefore, the model transfer function in both terms (voltage and current) can be expressed in function of the duty cycle as follows:

$$\frac{V_{in}}{V_{C_{DC}}} = \frac{i_{in}}{i_{DC}} = 1 - u \tag{2.19}$$

The input current i_{in} and the output voltage $V_{C_{DC}}$ are measured instantaneously in order to compute the values of the voltage and current signals fed to the controlled sources. The average modeling of DC-DC bidirectional converters is done using the same approach, relying on their respective equations.

2.4 Conclusion

In this chapter, the architecture of the studied microgrid system is presented and discussed. The system consists of four different sources of electrical energy: the photovoltaic system as the primary energy source, the fuel cell as an auxiliary energy source, the battery as an energy storage support, and the supercapacitor as a power storage support. Each source is connected to the DC bus, the power node, through an appropriate converter that adjusts its voltage level to that of the bus. This includes reversible current-type converters for the battery and supercapacitor and a Boost-type converter for the photovoltaic

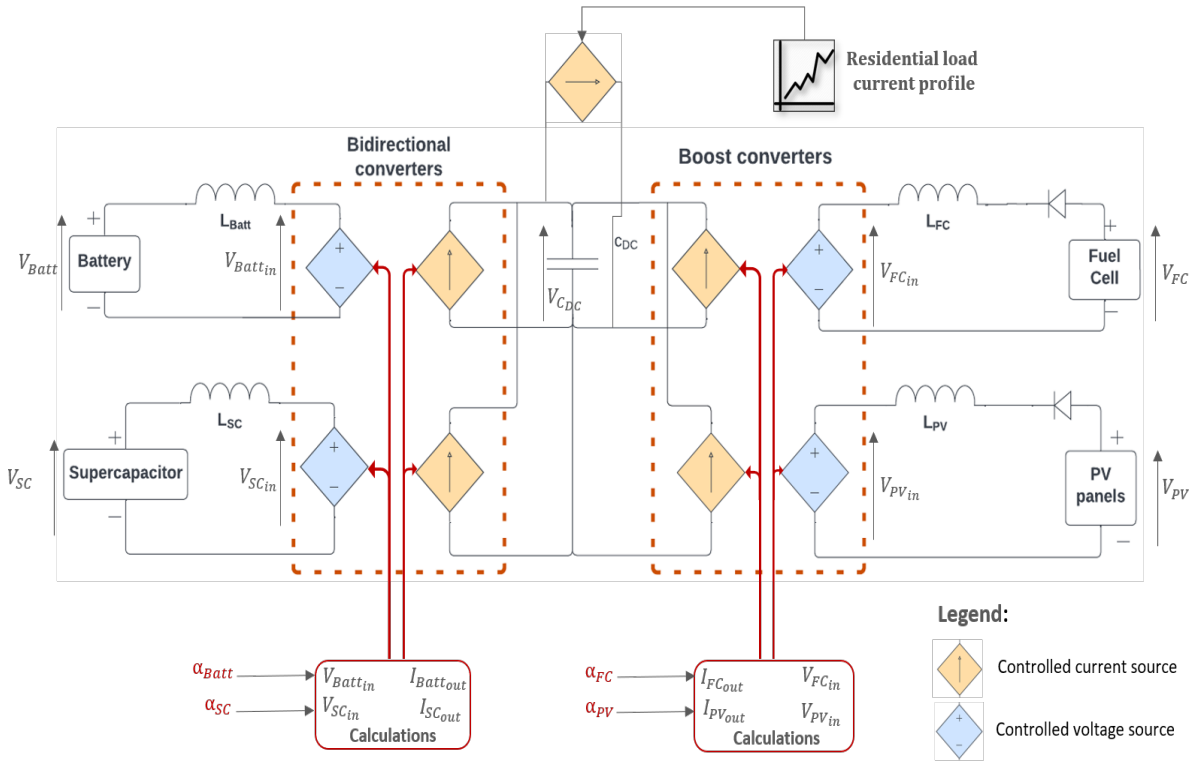

Figure 2.14 – The average modeling circuit diagram of the MG.

system and the fuel cell to prevent reverse currents. The architecture is primarily designed as a hybrid system, with the aim of increasing the autonomy of the electric support and extending the lifespan of the onboard sources, particularly the fuel cell and battery, by utilizing complementary dynamic sources.

In this chapter, a comprehensive modeling of the components of the microgrid is provided. The electrical models of the energy sources are presented and discussed in detail. Two techniques for modeling the power electronic converters have been also described in this chapter. The first technique, which is instantaneous in nature, is used for control simulation purposes. The second technique, which is based on average values, is employed for energy management system simulation purposes.

In the following chapter, the hierarchical control structure designed for the studied microgrid will be presented, including the theory of the control technique, simulation, and results, which will be shown and discussed.

Chapter 3

Microgrid Control

3.1 Introduction

Guaranteeing a stable DC bus voltage in a DC microgrid is crucial for reliable power distribution, grid stability, protection of energy storage systems, efficient energy management, and safety. It ensures that power from renewable sources or energy storage systems can be efficiently distributed, helps maintain stability and integrity of the microgrid, protects energy storage systems from over-voltage or under-voltage conditions, enables efficient energy management, and minimizes safety risks. Stable DC bus voltage is essential for uninterrupted power supply, optimal system performance, and overall microgrid reliability. In this thesis framework, the reliability and the resilience of the DC microgrid is emphasized through their ability to maintain a stable DC bus voltage in the face of serious disturbances like fluctuations in renewable energy source and load changing over time which are considered as high-probability events. Robustness against parameters variation as well as sensitivity to sensor noise sensor are also taken into consideration as part of the DC microgrid resilience assessment.

For a stable operation in this DC microgrid, it is necessary to make sure that the following net power P_{net} is maintained as zero:

$$P_{\text{net}} = P_{production} \pm P_{storage} - P_{\text{Load}}$$

where $P_{production}, P_{storage}$ and P_{load} are the total output power of the generation sources, the storage and the load respectively. In order to achieve this power balance, a hybrid energy storage system (HESS) is utilized to regulate the DC bus voltage. The HESS is responsible for either supplying or absorbing the required power or energy, with the aim of improving response times to enhance the microgrid's resilience and stability.

This chapter focuses on the control structure proposed for the application under consideration. Specifically, we present a hierarchical control structure that is designed to meet

the control objectives of the system. In addition, we propose a control technique that is used within this structure to effectively control the system. The proposed technique is the model-free super twisting sliding mode control, which is known for its robustness and fast convergence properties. We then present the simulation results obtained using the proposed control structure and technique. Three case studies are considered, and the performance of the proposed control technique is technically compared with two other nonlinear controllers, namely the feedback linearization and the conventional sliding mode control. The simulation results provide a comprehensive evaluation of the effectiveness and the superiority of the proposed control technique for the considered application.

3.2 Hierarchical control structure

The MG controller's primary goal is to stabilize the DC bus voltage while maintaining a balanced power flow between the various energy sources and consumers. Think globally and act locally is the foundation of the proposed control philosophy. This is accomplished using a Systems of Systems methodology [[172], [173]]. It is significant to note that each component of the system was developed with the goal of contributing to the stability of the entire DC microgrid. Figure 3.1 details the hierarchical control structure made up of dual cascaded loops of voltage and current control. The higher level represents the global controller which is responsible for setting the overall goals or set points for the system, it is represented by the DC bus voltage control as well as the MPPT control of the PV. The low level controllers represents the local controllers that are responsible for implementing the necessary control actions to achieve those goals. They are represented by the local current controllers at the power converter levels of each MG component. It it worth mentioning that a hierarchical control structure can help with improved performance, stability and more flexibility in a system [[86], [123], [172]–[174]].

To explain the internal work of this control structure, let's first start by the PV panel. In order to extract the maximum power that can be generated by the solar system, the high level control of the PV panel represented by the maximum power point tracking algorithm (MPPT) generates a time varying (piecewise constant) reference voltage to be tracked by the local control at the PV boost converter level. When the full PV power is generated and directly fed to the load, then any excess or deficiency in the power at the DC bus level is meant to be supported by the remaining energy units (FC, Batt and Sc). This will be done according to the specs of each element to accommodate such

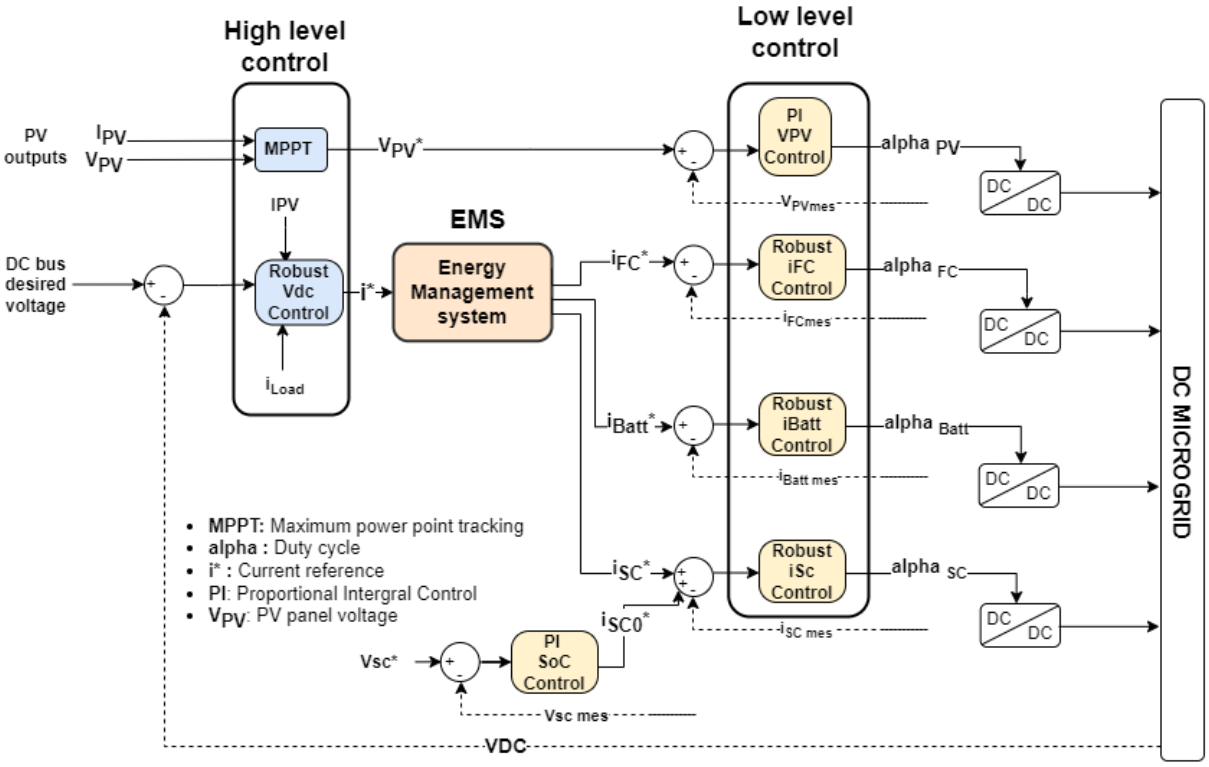

Figure 3.1 – Hierarchical control structure

fluctuations. Hence, a DC bus voltage regulator at a high level computes the total required current to be provided/absorbed by the storage units in a way to comply with the energy balance principle. The system exhibits a multi-time-scale behavior characterized by the presence of fast, intermediate and slow transients. Therefore, the total reference current is transmitted to the storage units by means of an energy management system that takes the role of the current allocation. It distributes the current between the different units (Batt, SC and FC) according to their physical and dynamical specs. Thereafter, each split of current is tracked by its corresponding local controller, through generating a duty cycle to control the associated converter. From the point of view of current and voltage dynamics, the current dynamics requires to be controlled such as to be much faster than the voltage dynamics. As a result, the system may operate on several time scales. In addition, an extra proportional-integral (PI) control loop is implemented to regulate the State of Charge (SoC) of the supercapacitor. This control loop addresses the quick discharge characteristic of the supercapacitor. By actively monitoring and managing the SoC, the control system optimizes the operation of the supercapacitor to maintain its performance and longevity.

3.3 Control technique: Model-Free STSMC

SMC has been used for trajectory tracking, power flow control, vehicle dynamics control, energy management, and other control tasks, demonstrating its versatility and effectiveness in diverse applications including robotics, power electronics, automotive systems, aerospace systems, renewable energy systems, and process control. In a general sense, the sliding Mode Control (SMC) approach is chosen for various applications due to its systematic resilience and robustness when it comes to uncertain models with unknown time varying plant parameters, as well as bounded matched disturbances and parasitic dynamics, therefore offering an attractive control approach for the MG systems. The principle of the sliding mode control is to force the system trajectories to reach a domain (named sliding surface) in a finite time. This domain is attractive; once the system trajectory has reached it, it is insensitive to the perturbations and uncertainties, and the dynamics of the closed-loop system is linked to the sliding surface definition.

Consider a dynamic system of the form:

$$\dot{x} = a(t, x) + b(t, x)u \tag{3.1}$$

where a, b represent the continuous nonlinear functions in the system, $x \in R^n$ is measureable state vector and $u \in R$ is control input.

The design of the SMC is made in two steps:

1. Designing a proper sliding manifold (common for standard 1st order SMC and MF STSMC):

$$\sigma(t, x) = (d/dt + p)^k e, \quad e = x^* - x \tag{3.2}$$

   Where p is the the slope of the sliding surface that is inversely proportional to the reaching time, it is assumed to be a strictly positive constant to make the sliding function Hurwitz stable. The integer parameter k must be equal to $r - 1$, with r being the relative degree of the system, e is the error state, x is the measured state variable and x^* is the desired one.

2. Designing a control action in order to force the system trajectories to reach and to remain on the sliding surface after a finite time, in spite of the uncertainties and perturbations.

Conventionl model-based SMC:

There have been various methods developed for creating model-based SMC, such as the one outlined in [175]. The following is the step-by-step design process [72], [104]:

1. After defining the proper sliding variable σ and set it to zero, a positive definite Lyapunov candidate function is proposed $V = \frac{1}{2}\sigma^2$ in order to determine a control law that keeps the system on $\sigma = 0$. The first derivative of V should be negative definite, $\dot{V} = \sigma\dot{\sigma} < 0$.
2. By means of the standard SMC algorithm, $\dot{\sigma}$ could be chosen as $\dot{\sigma} = -\rho\,\text{sign}(\sigma)$ where ρ is sufficiently large positive constant.
3. Finally, $\dot{\sigma}$ is replaced in the differential equation of the model so the final model-based control law is obtained. By ensuring $\sigma.\dot{\sigma} = -\rho\,|\sigma|$, reachability condition is satisfied.

The signal function, $sign(\sigma)$ can be expressed as

$$sign(\sigma) = \begin{cases} 1 \quad \texttt{if} \quad \sigma > 0 \\ 0 \quad \texttt{if} \quad \sigma = 0 \\ -1 \quad \texttt{if} \quad \sigma < 0 \end{cases} \tag{3.3}$$

Discontinuity in the control input is introduced due to the use of the signal function as it leads to an abrupt change in the control action when the system state crosses the sliding surface. This phenomena known as chattering can cause increased stress on power electronic components, such as transistors or thyristors, due to the high-frequency voltage and current oscillations. Thus, this can lead to increased wear and tear, reduced reliability, and decreased lifespan of the components.

The discontinuous "sign" term can be replaced by a continuous smooth approximation as

$$\frac{\sigma}{|\sigma| + \varepsilon}$$

where ε is a small positive value. The purpose of employing a continuous approximation is to reduce the controller gains close to the sliding surface, where the system tends to exhibit high-frequency oscillations, in order to minimize chattering. At the same time, the gains are maintained at higher levels away from the sliding surface to ensure rapid convergence. Although this smooth approximation can address certain issues, it may result in a reduction of robustness. As an effec-

tive alternative, the STSMC is introduced, which resolves the chattering problem without compromising the robustness properties [83].

Super-Twisting SMC:

The general form of a sliding mode control law includes two terms:

$$u = u_{eq} + u_{cor}$$

Where u_{equ} is the equivalent control calculated from the nominal model, and u_{cor} is a control correction based on tracking errors and the bounds of uncertainties [176]. With this distinction in mind, there are different approaches to MFSMC in the literature. The most common one is to neglect the equivalent control since it is based on the system model and to try and find a form of u_{cor} that results in the desired tracking while remaining stable and feasible [177], [178].

The relative degree of the system is assumed to be one, which implies that the first derivative of σ can be expressed as:

$$\dot{\sigma} = h(t,x) + g(t,x)u, \quad h = \dot{\sigma}|_{u=0}, g = \frac{\partial \dot{\sigma}}{\partial u} \neq 0 \tag{3.4}$$

Furthermore assume that for some positive constants C, K_m, U_m, q

$$|\dot{h}| + U_M|\dot{g}| \leq C, \quad 0 \leq K_m \leq g(t,x) \leq K_M, \quad |h/g| < qU_M, \quad 0 < q < 1 \tag{3.5}$$

hold and define the control law $u(t)$ based on the Super-Twisting Sliding Mode control algorithm as:

$$\left.\begin{array}{l} u_1 = -\lambda\,|\sigma|^{\tau}\, sign(\sigma), \;\; \tau \in]0, 0.5] \\ \dot{u_2} = -\alpha sign(\sigma) + \beta(u - u_{sat}) \end{array}\right\} u_1 + u_2 = u(t) \tag{3.6}$$

With $K_m\alpha > C$ and λ sufficiently large, the controller (Eq. 3.6) guarantees the appearance of a 2-sliding mode $\sigma = \dot{\sigma} = 0$ in system (Eq. 3.1), which attracts the trajectories in finite time [179]. This control scheme guarantees the appearance of a second order sliding mode , which attracts the trajectories in finite time [180], [181]. Further insights into the supertwisting sliding mode control theory can be found in [179].

The convergence of the sliding mode trajectories on the second order sliding plane

are characterized by twisting around the origin as shown in Figure 3.2 [83]. The convergence analysis is given in [182].

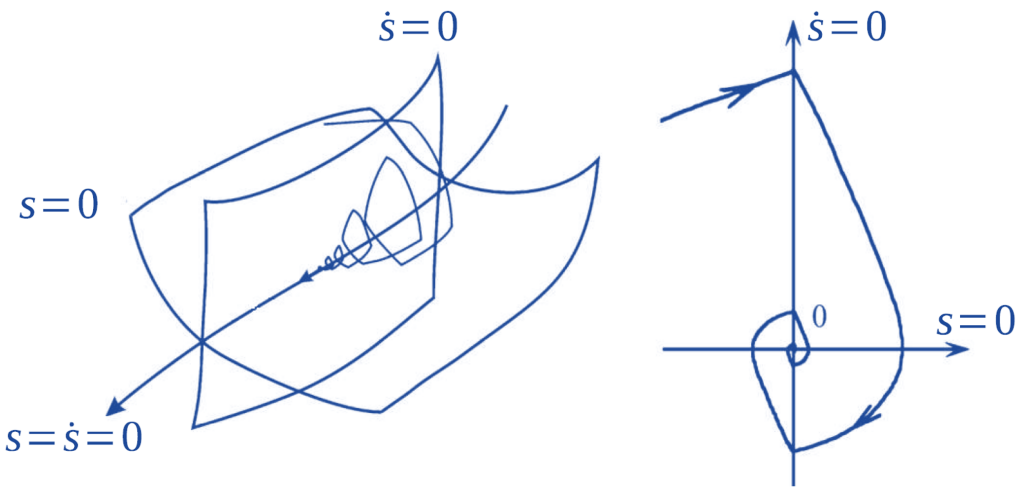

Figure 3.2 – Super-twisting sliding mode trajectory.

Hence, the following properties are exhibited by the super-twisting control formulation [179]:

— The Super-Twisting control represented in Eq.3.6 is a second-order sliding mode control, since it drives both $\sigma, \dot{\sigma} \rightarrow 0$ in finite time.

— it is continuous since both the proportional and the integral term are continuous. Now, the high-frequency switching term sign(σ) is hidden under the integral.

In our control study case, the low-level controllers are designed to operate within an admissible duty cycle range, while the DC bus voltage controller (high-level controller) is limited by the extremum current values supported by the ESS. As a result, a saturating actuator is used to introduce control input to the system. However, the signal generated by the regular super-twisting controller may exceed the saturation limits, leading to an unwelcome windup event due to the integral action of the controller [183]. To address this challenge, an anti-windup approach is utilized. The existing literature suggests several techniques for anti-windup, with the back-calculation, integrator, and clamping anti-windup methods being the most commonly used. Back-calculation is a straightforward method for anti-windup that maintains the original control structure but may suffer from slow recovery and require additional parameter tuning. The integrator method offers fast recovery and stability, but may introduce overshoot and require careful tuning.

Clamping is a simple approach that prevents integrator windup but can cause discontinuities and may require careful handling. In this work, the back-calculation technique is introduced, it uses a feedback loop to unwind the controller block internal integrator when the controller hits specified saturation limits and enters nonlinear operation. It is represented by the term $\beta(u - u_{sat})$ in equation Eq.3.6, where β is the anti-windup gain and u_{sat} is the saturated control law at the actuator level.

Projecting this theory on the concerned application, the corresponding sliding manifold of each controller is listed as below:

- $\sigma_{DC\ bus} = {V_{DC}}^* - V_{DC}$
- $\sigma_{i_{FC}} = {i_{FC}}^* - i_{FC}$
- $\sigma_{i_{batt}} = {i_{batt}}^* - i_{batt}$
- $\sigma_{i_{Sc}} = {i_{Sc}}^* - i_{Sc}$

The control law showed in Eq. 3.6 is reproducible for each one of the low and the high level controllers. The obtained control laws for the low level control are represented by the duty cycles u_{FC}, u_{Batt} and u_{Sc}. They are imposed on the different converters by means of PWM. PWM allows converting the continuous values of duty cycles into a series of 0-1 which determine the switching states (on or off) of the different transistors in the converters. The obtained control law for the DC bus voltage control is the current reference i^*_{st} to be supported by the fuel cell and/or the storage system (only in case of power deficiency the fuel cell is called, since the fuel cell does not support reverse flow direction. Otherwise the power is totally supported by the storage system).

3.4 Feecback linearization - Candidate controller for comparison puprpose

Feedback Linearization (FL) is a model-based method for nonlinear control which amounts to cancel the nonlinearities of a nonlinear system through a change of variables such that the resulting closed-loop dynamics is linear [184]. The basic idea is to find a suitable coordinate transformation creating a virtual control system that is mathematically equivalent to the nonlinear system being controlled. After transformation, a linear feedback controller can be designed using standard linear control techniques to stabilize the system and attain desired performance objectives [175].

Feedback linearization can be applied to a class of nonlinear system described by the so-called companion form, or controllability canonical form. Consider the state-space

representation of a system in companion form (assuming b to be non-zero)

$$\begin{bmatrix} \dot{x}_1 \\ \dot{x}_2 \\ \vdots \\ \dot{x}_n \end{bmatrix} = \begin{bmatrix} x_2 \\ x_3 \\ \vdots \\ f(x) + b(x)u \end{bmatrix} \tag{3.7}$$

where

x	:	the state vector
$f(x), b(x)$	:	nonlinear function of the state
u	:	scalar control input

For this system, using the control input of the form

$$u = (v - f)/b \tag{3.8}$$

we can cancel the nonlinearities and obtain the simple input-output relation (multiple-integrator form) $x^{(n)} = v$. Thus, the control law

$$v = -k_0 x - k_1 \dot{x} - \ldots - k_{n-1} x^{(n-1)} \tag{3.9}$$

with the k_i chosen so that the polynomial $p^n + k_{n-1}p^{n-1} + \ldots + k_0$ has its roots strictly in the left-half complex plane, lead to exponentially stable dynamics

$$x^{(n)} + k_{n-1}x^{(n-1)} + \ldots + k_0 x = 0 \tag{3.10}$$

which implies that $x(t) \to 0$. For tasks involving the tracking of the desired output $x_d(t)$, the control law represented by

$$v = x_d^{(n)} - k_0 e - k_1 \dot{e} - \ldots - k_{n-1} e^{(n-1)} \tag{3.11}$$

(where $e(t) = x(t) - x^*(t)$ is the tracking error) leads to exponentially convergent tracking.

3.5 Simulation and results

In order to evaluate the proper functioning and feasibility of the proposed control structure and law, numerical simulations have been conducted using MATLAB/Simulink

with the aid of the SimPower-Systems™ Toolbox. Different test conditions have been investigated including alterations in power generation, fluctuations in load demand, parameters variation and potential sensor noise. A key point to consider is that a conventional frequency-decoupling based EMS was used to carry out the control structure simulation. Chapter 4 provides a thorough explanation of this EMS.

3.5.1 First case study

The cascade control system is tested for a residential microgrid application under different conditions of power generation and load demand.

System operating conditions

The simulation results presented in this case study are given:
— By using the microgrid architecture with four components (PV, FC, Batt and Sc).
— By using the control configuration shown in figure 3.1.
— The physical characteristics (sizing and properties) of the components are given in the Appendix 2.
— The weather and load conditions are given in the following paragraphs (Figure 3.4,3.3).

Weather and load demand profiles

This paragraph shows the operating conditions related to a studied residence. It should be noted that the isolated house for this application is assumed to be located in the city of Saint Nazaire in France [185]. Realistic profile of the solar irradiance as well as a residential load power demand is considered in order to create, to a great extent, realistic scenarios.

Irradiance

Figure 3.3 shows an estimate of the sunshine evolution over a day. Photovoltaic production is zero at night. It begins to increase at the beginning of the day to reach a maximum around 1 p.m. and then it decreases until it disappears around 7 p.m. The photovoltaic production may present breaks or degradation during the day due to climatic conditions (clouds, tree, etc.). This solar profile on which the solar electricity production rely on, is the input to the PV system. Based on this profile, the double stage MPPT algorithm

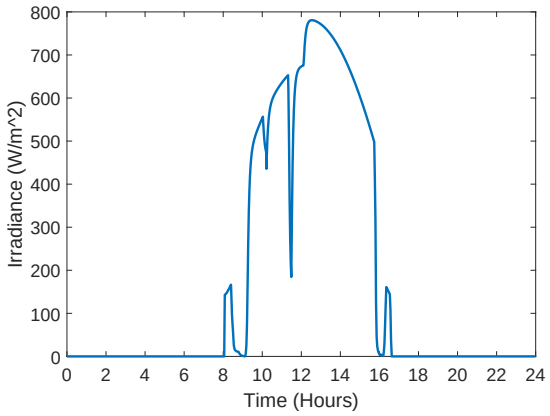

Figure 3.3 – Estimated daily profile of sunshine in the considered geographical area.

tries to impose, on the PV system, a voltage profile of the optimal voltage values that corresponds to the maximum power that can be extracted.

Power load profile

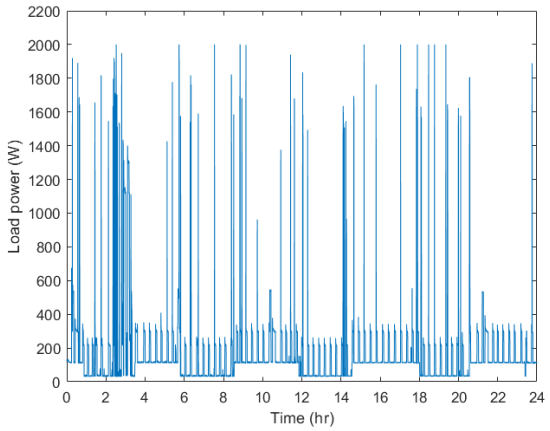

Figure 3.4 – Daily load profile of the studied residential habitat.

Figure 3.4 presents a daily consumption profile of the studied residential habitat, it is provided by a generator of individual consumption profiles of group of loads (washing machine, consumption lighting, an oven, a refrigerator, a microwave, a hob, a dishwasher and a washing machine, etc). These individual profiles are then randomly aggregated while taking into account the probabilities of occurrence of certain loads at certain times of the day. The consumption profile generator was developed in the test hall of IREENA

- UR 4642 laboratory and used in other works as in [21], [174].

MPPT behavior

Figure 3.5 reports the behavior of the double stage MPPT control, where the PV panel voltage V_{PV} is greatly tracking its reference that was generated by the MPPT algorithm. The PI controller used as a local controller in the double-stage MPPT seems to be efficient and effective in this task (see Figure 1.5).

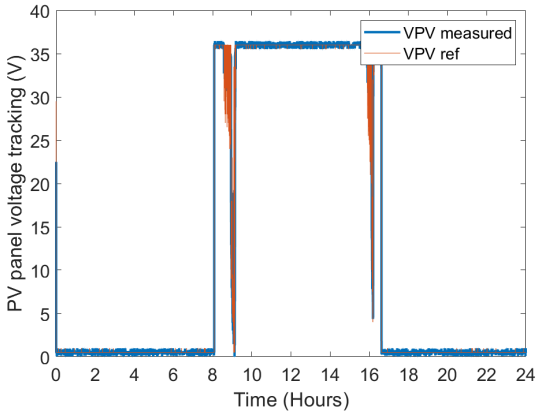

Figure 3.5 – PV panel voltage tracking.

DC bus voltage stabilization

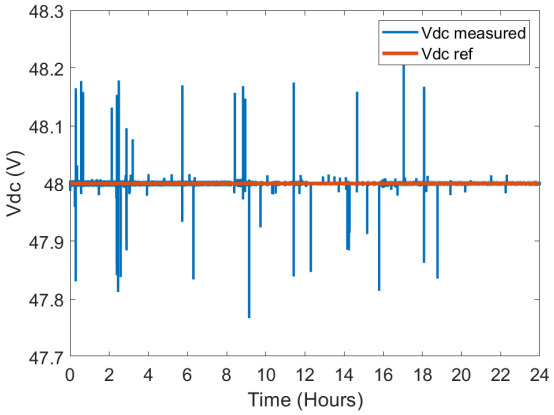

Figure 3.6 – Common DC bus voltage.

The common DC bus voltage profile can be seen in figure 3.6. An excellent tracking performance is noticed along the 24 hrs of simulation. The DC bus voltage varies briefly following the transients, recovering and settling at the rated voltage (48V). Voltage sags and swells while over and under-shooting is obvious as a response to the imposed external disturbances represented by irradiance and load demand variations. But with the suggested MF-STSMC strategy inside the multi-level control structure, the maximum voltage tracking error is about 0.24 V which is still far from the maximum acceptable limit (i.e. refereed as the 10% of the rated voltage).

Current tracking in FC and ESS

As previously explained, the EMS generates current references to stabilize the microgrid by controlling the energy flow among the FC, the Batt, and the SC. Figure 3.7, 3.8 and 3.9 depict the current tracking performance under these three energy components, the FC, the Batt and the Sc respectively. The local control design results in excellent tracking behavior, as shown by the graphs. The different time scales of the components can be seen in the signal frequency: the FC receives the lowest frequency signals, the battery receives medium frequency signals to meet energy needs over a longer period, and the SC supports high frequency signals to mitigate the impact of external disturbances. Note that a negative current sign indicates that the storage unit is in charging mode (storing energy), while a positive current sign indicates the discharging mode (releasing energy).

Duty cycles

The duty cycles, which are generated by the local controllers and serve as inputs to the DC-DC converters, are shown in Figure 3.10. The figure displays the duty cycles for the Battery, the SC, and the FC on the same graph. However, it confirms that the control laws are within their specified limit range of]0,1[that is supported by the converters. This limit range is guaranteed to be respected by the controllers, thanks to the anti-windup technique, regardless of any gap between the initial and reference values of the controlled signal.

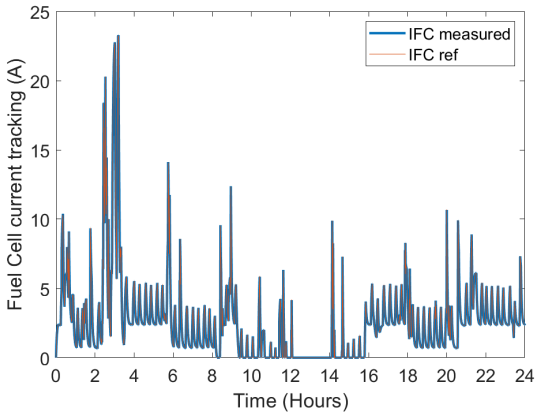

Figure 3.7 – Fuel Cell current tracking.

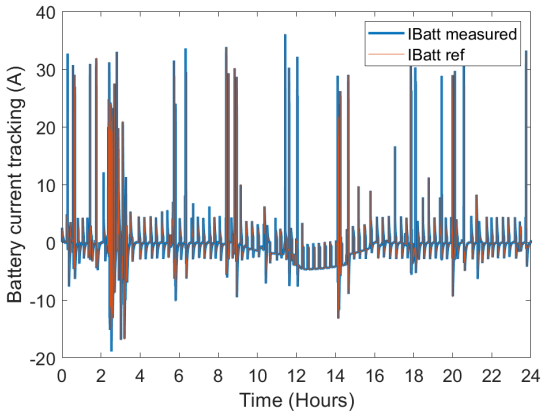

Figure 3.8 – Battery current tracking.

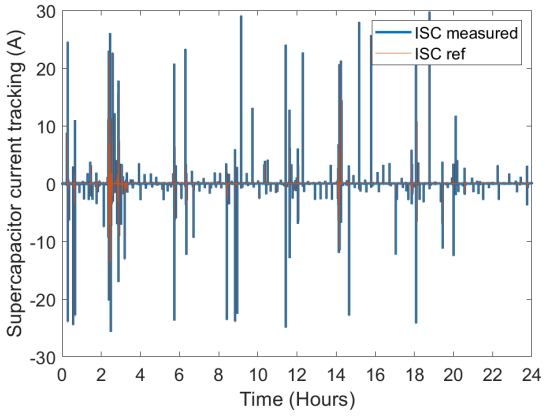

Figure 3.9 – Supercapacitor current tracking.

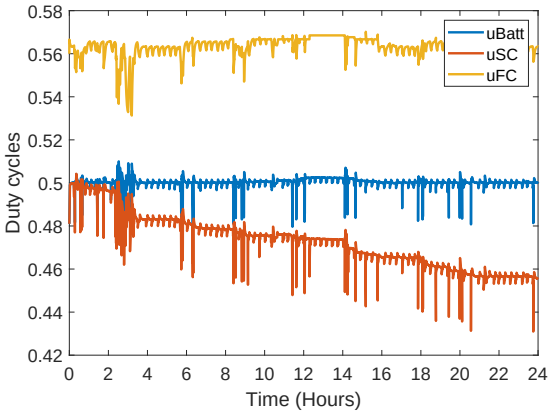

Figure 3.10 – Converters duty cycles for the FC, Batt and SC.

Power flow balance

In addition to regulating the DC bus voltage, another key objective of the control and management structure is to maintain a balanced power flow in the microgrid. Figure 3.11 displays a zoomed view (1hr period of time) of the power balance profiles of the various elements in the MG. The PV unit and the three dynamically complementary sources - the FC, Batt, and SC - provide the requested power on the DC bus. It is evident that during peak power demand, the supercapacitor instantaneously supports the majority portion of the demand, returning to zero right after the transitory phase. On the other hand, the battery reacts less quickly than the SC and supports the remaining portion of the peak demand, slowly settling at zero after transitory while satisfying the medium-frequency power demand. Since the fuel cell works as an auxiliary energy source, it is completely off for the steady phase support if the PV panels production is sufficient for the load. In other terms, the SC behave like a high-pass filter with a time constant of a few seconds (high frequency signals) while the battery and the FC take care of the rest in order to ensure continuity of service (medium/low frequency signals). This is how the time-scale concept is employed in this microgrid.

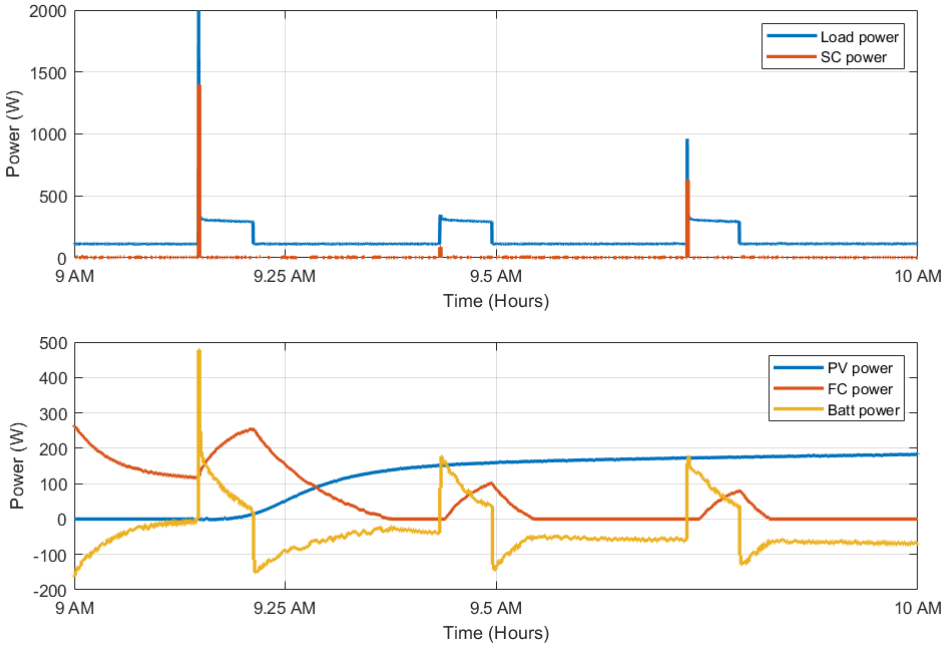

Figure 3.11 – Power flow distrubution between microgrid components.

3.5.2 Second case study

In this case study, a comparison is made between the Model-Free STSMC and the Model-based conventional SMC in terms of performance under the influence of control input disturbances and parameters variation. The objective is to evaluate and contrast the robustness and adaptability of these two approaches in dealing with uncertainties and disturbances in the system.

The simulation results presented in this case study are given:

— By using the microgrid architecture with three components (PV, Batt and Sc).

— By using the same hierarchical control structure in Figure 3.1 while adapted to three sources .

— The physical characteristics (sizing and properties) of the concerned components are given in the Appendix 1.

— The weather and load conditions are given in Figure 3.12.

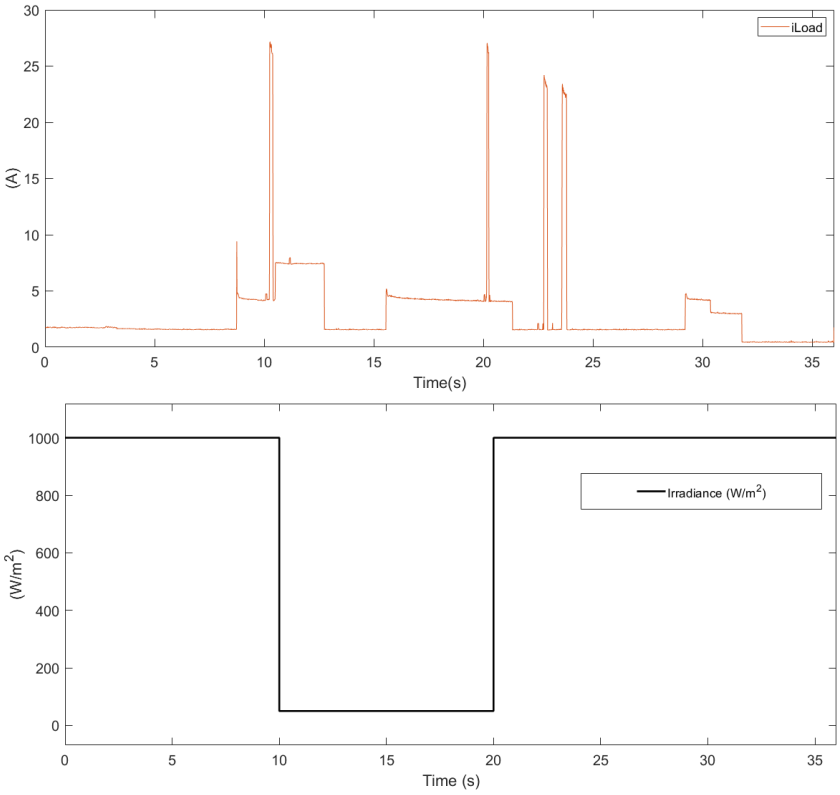

Figure 3.12 – Load and irradiance testing profile.

In Figure 3.13, the performance of both Model-Free STSMC and Model-Based SMC are compared. Details about conventional sliding mode control design are all available

in [179]. The DC bus voltage responses to changes in load and PV current indicate that the Model-Free STSMC shows an excellent tracking performance with a rapid recovery to the rated value of $48V$, with only slight errors of up to $1.5V$. On the other hand, the model-based SMC also shows a good tracking performance, but with noticeable differences in both over and undershoots when compared with the Model-Free STSMC. The model-based SMC registers a maximum tracking error of $7V$.

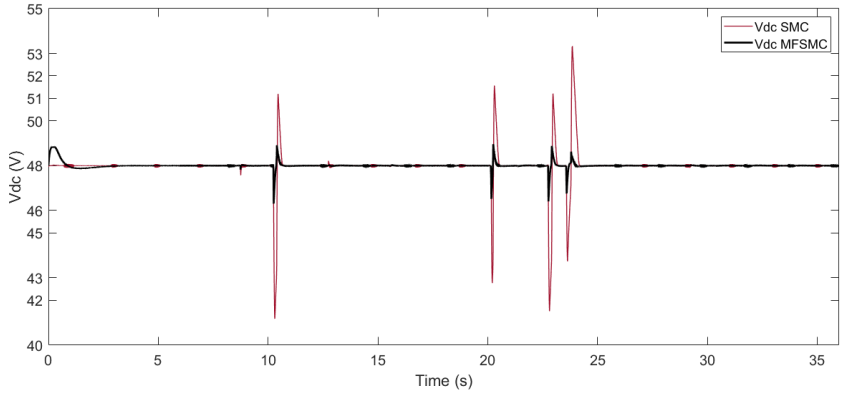

Figure 3.13 – DC bus voltage under MFSMC and SMC

Testing under control input disturbance

In practical implementation, the control law generated using any technology such as Digital Signal Processing (DSP), programmable logic controllers (PLC), microcontrollers or field-programmable gate arrays (FPGA)..., can be potentially influenced by various internal and external factors, including disturbances and quantization effects. Disturbances can come from external factors such as temperature changes or mechanical vibrations, or internal factors such as component failures. On the other hand, quantization effects can occur when the controller system converts analog signals to digital signals. Quantization can introduce errors or distortion in the signals, which can ultimately impact the accuracy of generated the control law. This section describes the simulation test where an input disturbance is introduced into the control law generated from the DC voltage control. In other terms, the current reference generated from the high level control is being disturbed in the form of an impulse signal with an amplitude of 2A, which is equivalent to 10% of the average value of the current reference signal. The impulse signal lasts for 1 second and occurs between the 10th and 11th seconds. Figure 3.14 illustrates the response of both controllers to this applied disturbance. The conventional SMC controller shows a

significantly greater over and undershoot, leading to a tracking error of around 7V. In contrast, the MFSMC controller has a maximum error of 2.5V.

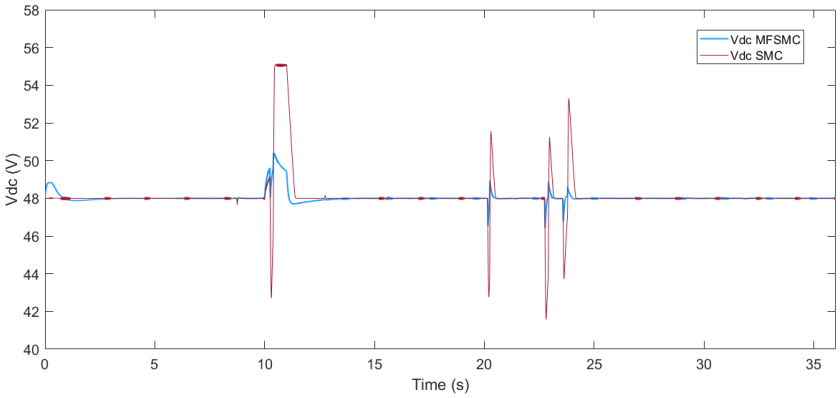

Figure 3.14 – DC bus Voltage control under disturbance: Model-Free STSMC vs. conventional SMC.

Testing under parameters variation

In practical electronic systems, the value of an electronic component may vary due to several factors, including manufacturing variations, temperature dependence, aging and degradation, and environmental factors. Manufacturing variations can introduce variations in component properties, which are accounted for by specifying a tolerance range. Temperature dependence and aging can cause values to drift over time, while environmental factors such as humidity, vibration, and exposure to chemicals can also affect component values [186]. In order to evaluate the candidate controllers, two model parameters are selected within their specified range of perturbation: the capacitance value of the DC bus capacitor and the inductance of both bidirectional converters. Specifically, a 20% downshift in the capacitance value and a 20% upshift in inductance value are applied. The impact of these variations on the system under sliding mode control (SMC) is illustrated in Figure 3.15, which shows that parameters variation amplifies both the overshoots and undershoots of the DC bus voltage.

The performance of the MF-STSMC controller is compared to SMC under these conditions, as shown in Figure 3.16. The relative difference (with-without parameters variation) in the overshoots and undershoots between SMC and MF-STSMC is approximately 10% and 1%, respectively. This indicates that the MF-STSMC controller is better equipped to handle DC bus stability in the presence of parameters variation or uncertainty.

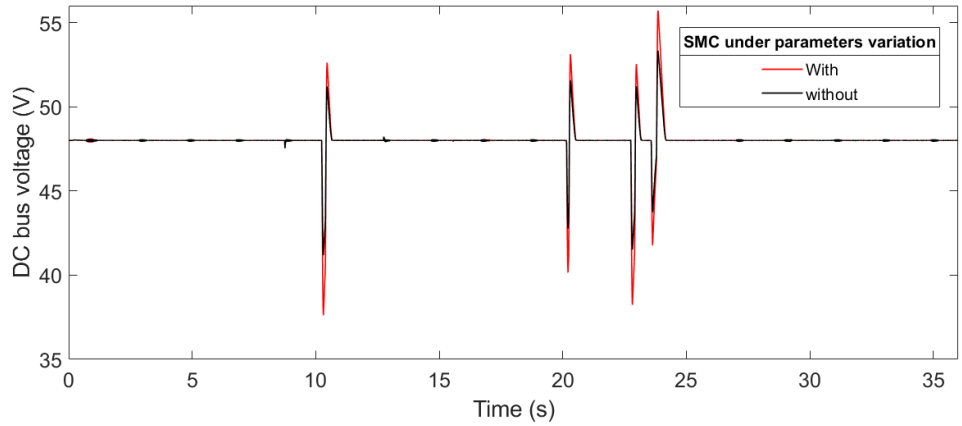

Figure 3.15 – DC bus Voltage Control under parameter variation: SMC

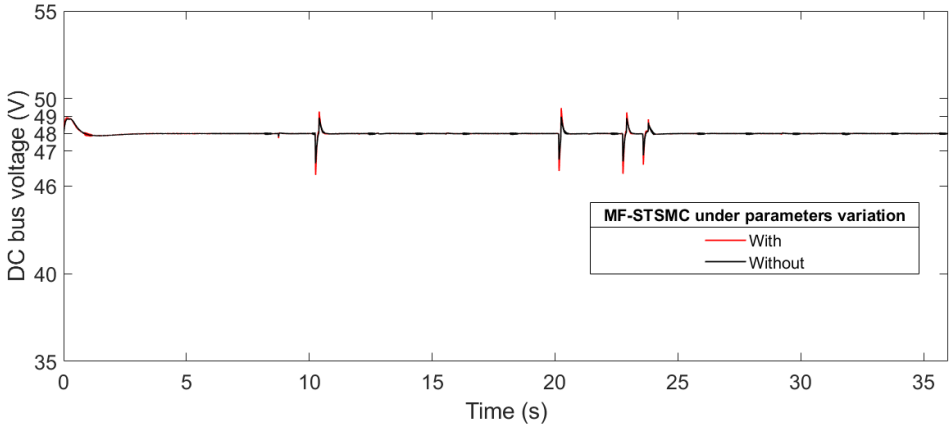

Figure 3.16 – DC bus Voltage Control under parameter variation: MF-STSMC

3.5.3 Third case study

This case study compares the sensitivity of Model-Free STSMC and feedback linearization control with respect to a measurement sensor noise. All the controller are desgined with respect to the theory presented in section 3.4. The simulation is carried out based on the same system with all specifications stated in the list 3.5.2.

Feedback linearization control implementation

Given that all the controllers share the same design concept,an example can be demonstrating by showcasing the implementation of the battery local control design. The differential equation that represents the instantaneous dynamic model of the battery along

with its converter (see Figure 2.13 in Chapter 2) is extracted based on power electronics averaging technique as:

$$L_{Batt}\frac{di_{L_{Batt}}}{dt} = V_{Batt} - u_{Batt}V_{DC} + (u_{Batt}(R_{D1} - R_{D2}) - R_{D1})i_{L_{Batt}} \tag{3.12}$$

where L_{Batt} is the inductance of the DC–DC bidirectional converter, $i_{L_{Batt}}$ is the output current of the batttery, V_{Batt} is the batttery voltage, u_{Batt} is the switching control signal for the corresponding DC–DC converter, V_{DC} is the DC bus voltage, R_{D1} and R_{D2} are the driving resistors of the power converter. Neglecting the internal resistance of the transistors, if u_{Batt} is chosen as:

$$u_{Batt} = -\frac{L_{Batt}}{V_{dc}}(-\frac{V_{Batt}}{L_{Batt}} + \gamma) \tag{3.13}$$

with γ being an the new equivalent input to be specified, the nonlinearity in equation Eq. 3.12 is canceled and the resulting dynamic become linear,

$$\begin{aligned} L_{Batt}\frac{di_{L_{Batt}}}{dt} &= V_{Batt} - (-\frac{L_{Batt}}{V_{dc}}(-\frac{V_{Batt}}{L_{Batt}} + \gamma))V_{DC} \\ \frac{di_{L_{Batt}}}{dt} &= \gamma \end{aligned} \tag{3.14}$$

choosing γ as

$$\gamma = -a\, e - b\int_0^t e\, d\tau + \dot{i^*_{L_{Batt}}} \tag{3.15}$$

where $e = i_{L_{Batt}} - i^*_{L_{Batt}}$ being the batttery current error, a and b being strictly positive constants which asymptotically lead the output of the system to its desired trajectory. Note that $\dot{i^*_{L_{Batt}}}$ can be neglected considering that the lower loop dynamic is much faster than the upper loop one, the resulting closed loop dynamics is:

$$\dot{e} + a\, e + b\int_0^t e\, d\tau = 0 \tag{3.16}$$

This implies that $e(t) \to 0$ as $t \to \infty$. Based on equations Eq. 3.13 and 3.15, the control input is determined by the nonlinear control law as:

$$u_{Batt} = -\frac{L_{Batt}}{V_{dc}}\left[-\frac{V_{Batt}}{L_{Batt}} - a\, e - b\int_0^t e\, d\tau\right] \tag{3.17}$$

The control law expressed in equation 3.17 utilizes the first term to supply the battery current, while the remaining two terms are utilized to control and adjust the current value based on the desired dynamic behavior specified by Eq. 3.16. Further information and specifics about this control methodology can be found in [187].

Sensitivity analysis to sensor noise

Figures 3.17 and 3.18 depict the disturbed conditions during the test in terms of irradiance and load current demand, respectively.

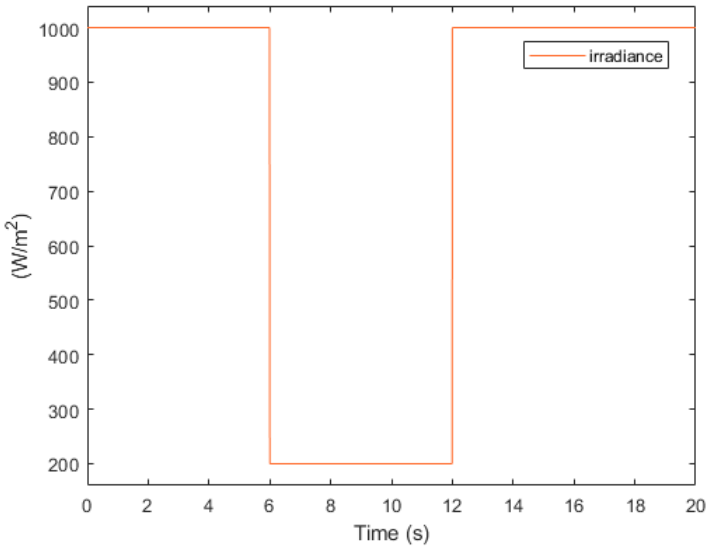

Figure 3.17 – Irradiance test profile.

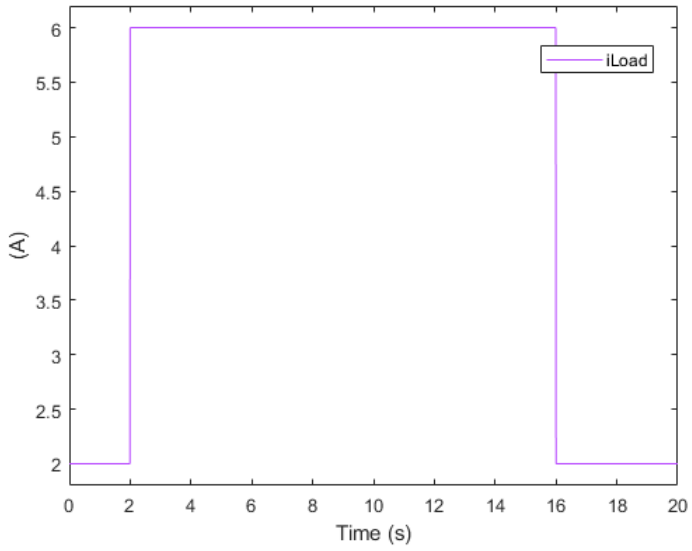

Figure 3.18 – Load current test profile.

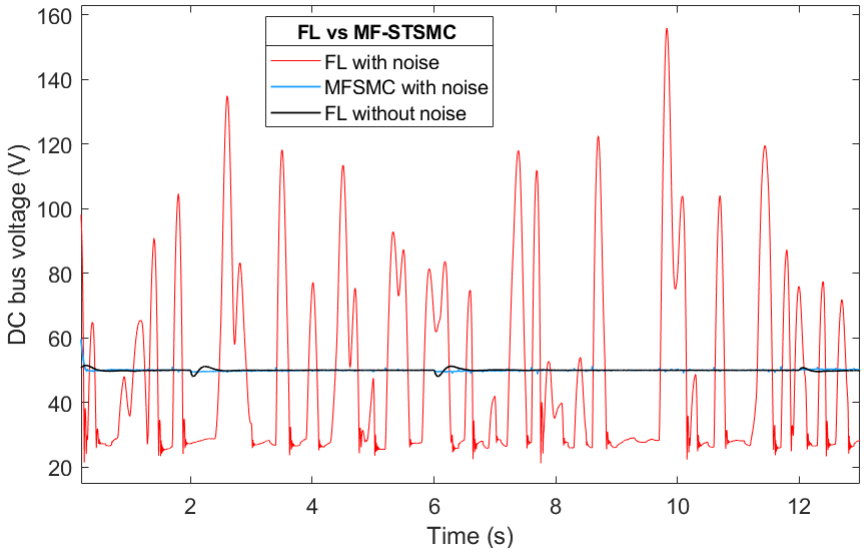

Figure 3.19 – DC bus voltage control under sensor noise: FL vs MF-STSMC.

Figure 3.19 presents a comparison between the FL and the MF-STSMC under an added white gaussian noise to the feedback variable, i.e. the DC bus voltage measurement. The amplitude of the noise is set to approximately ± 2% of the rated DC bus voltage value. Before the noise is introduced, the system controlled by Feedback Linearization shows that it can regulate the DC bus voltage effectively, even when disturbances from irradiance and

load variations occur at 2s, 6s, 12s and 16s. However, when the sensor noise is added, the resulting signal shows how sensitive the controller is to even a small amount of injected noise. This sensitivity leads to a total loss of control, which is a significant concern. It is worth highlighting that the more the system is exposed to noise, the more the DC bus voltage fluctuations will occur. Hence the importance of ensuring robustness against such type of noises. In contrast, the proposed MFSMC demonstrates its robustness against the added noise as it has only a minor impact on the controller's behavior.

3.6 Conclusion

In summary, ensuring stable DC bus voltage and power flow balancing is crucial for the efficient and reliable operation of microgrid systems. Achieving these goals requires the use of advanced control techniques and monitoring systems to maintain the greatest performance and prevent equipment damage. Our proposed hierarchical control structure, which employs the model-free supertwisting sliding mode control technique, offers an effective solution to these challenges. Through three case studies evaluating its performance under various scenarios, including load and irradiance changes, parameter variations, and sensor noise sensitivity, the study has demonstrated the reliability and effectiveness of the proposed control structure. The model-free supertwisting sliding mode control technique was found to outperform conventional SMC and feedback linearization, particularly in handling disturbances and uncertainties. Furthermore, with some modified adaptations, the proposed control structure can be suitable for a range of other applications beyond residential use. This is due to its ability to address the challenges of DC bus voltage stability and power flow balancing in microgrid systems, making it a versatile solution for various energy systems.

In the upcoming chapter, the strategy of the proposed energy management system will be presented, and the results of conducted simulations will be shown. The performance of the proposed strategy will be analyzed, taking into consideration two other EMS strategies from the literature for comparison.

Chapter 4

Microgid Energy Management

4.1 Introduction

The hybrid renewable energy system (HRES) described in chapter 2, is composed of four energy units, two of them are energy sources (the PV panels and the Fuel Cell), the other two are considered as energy storage devices (the Battery and the supercapacitor). In this configuration, the PV panel works as the main energy source, while the Fuel cell serves as a backup energy system. It compensates the power shortage especially at night when there's no solar generation or in case of a partial or total shading in the PV panels. Meanwhile, the complementary hybrid energy storage system (HEES) ensures, besides storing the excess of energy, a high and fast support for the peak demand. It ensures a continuous and smooth fulfilling for the load demand in the long run.

Each unit of the multi-source system has its own specifications, dynamic requirements, feasible flow direction, power limitations in charge and discharge, and other specific constraints. In order to ensure a maximum efficiency of unit's use, the challenge here is to provide a suitable energy management system (EMS). This EMS acts as a power flow coordinator taking into account all the system constraints and requirements. The main objective of such EMS is to efficiently manage in real time the internal energy flows while ensuring healthy and safe operating conditions for Microgrid.

Figure 4.1 pinpoints the emplacement of the EMS within the microgrid's control structure. Located between the high and the low level control, the EMS dispatches the current/power references to be tracked by the corresponding energy units. This output is mainly computed based on the requested total current/power which represents the EMS input signal. In this chapter, two energy management system strategies are presented. First, the classic frequency-decoupling based EMS is detailed and then a new more efficient and economic EMS is proposed.

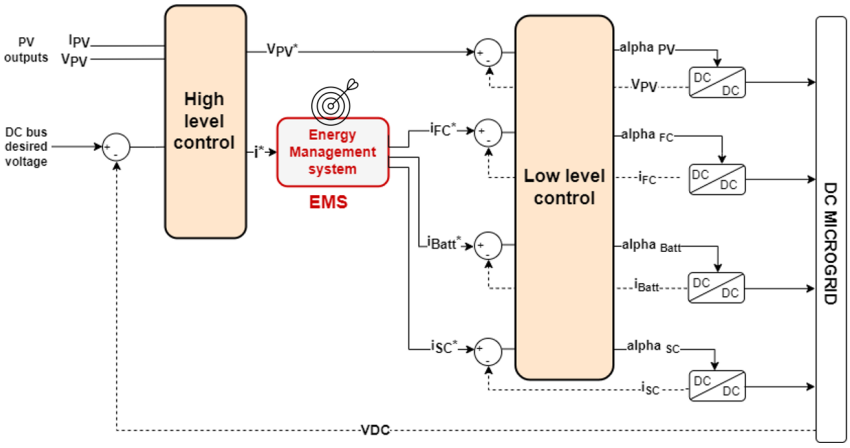

Figure 4.1 – EMS emplacement within the control structure.

4.2 Frequency-decoupling based EMS

As stated in the state of the art chapter, the frequency-decoupling based EMS (frequency separation method) is a widely common approach [131], [188], [91]. It is generally used to protect sensitive resources, such as Fuel Cells, from burst power loads. Basically, it breaks down the requested load power by assigning the convenient share to the corresponding source. Thus a frequency complementarity is ensured between the different sources. Indeed, its principle rests on allocating the high frequency power requests to the fastest energy unit, for example the SCs. Conversely, the low frequency power share will be attributed to the source unit with the slow dynamic, such as the FC. The medium frequencies are dedicated to the batteries. The implementation of this strategy is achieved through low-pass, high-pass and bandwidth pass cascaded filters.

Figure 4.2 illustrates the block diagram of the classic frequency-separation based EMS. This strategy is applied to the proposed microgrid where the managed units are the FC, the Batt and the SC. As shown in this block diagram, the frequency distribution of the energy flow is carried out via two low pass filters assigning two different cut-off frequencies $f_{c_{FC}}$ and $f_{c_{Batt}}$. These filters are used in a cascaded structure to perform a double frequency separation applied on the total requested current i^*. The cut-off frequency value must be chosen according to the characteristics of each source. This implies that a healthy frequency operating range must be wisely chosen for each component. These frequency ranges are obtained by plotting the Ragone diagram in the frequency domain, as portrayed in Figure 4.3 [189].

The Ragone diagram shows that the FC has a higher energy density than the battery

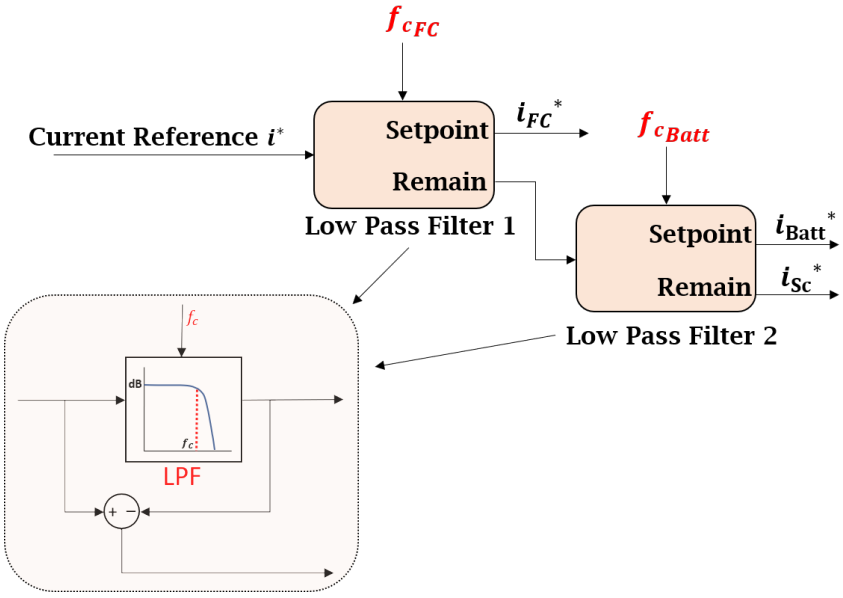

Figure 4.2 – Block diagram of the frequency-decoupling based EMS technique.

but on the other side it presents a slower dynamics and startup time than the battery. The Sc has a fast dynamical response with high power density and low energy density. Consequently, the first filter with a cut-off frequency of $f_{c_{FC}}$ arbitrates the low dynamic currents i^*_{FC} that the fuel cell must provide, and since a smaller cut-off frequency means stronger smoothenning of current, a cut-off frequency of $f_{c_{Batt}} > f_{c_{FC}}$ is attributed to the second filter which distributes the remaining current flows between the battery i^*_{Batt} covering the mid-range frequencies, and the supercapacitor i^*_{SC} that supplies the highest frequencies.

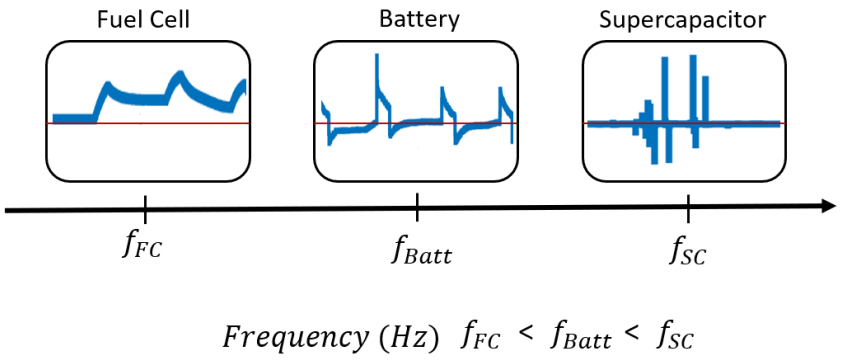

Figure 4.3 – Approximate frequency classification zones of FC, Batt and SC.

Despite the fact that this EMS grants a plug & play approach while protecting the

low dynamic component from a potential damaging due to the high peak load power, the use of such strategy has a key limitation which is the unguaranteed system stability and reliability since the storage's state of charge (SoC) are not taken into account. In point of fact, the battery SoC, which is in theory a number between zero and one, is usually subjected to a minimum and maximum thresholds aiming to prevent the battery abuse and its premature aging. Undoubtedly, a deep discharge of the battery can reduce both its lifespan and its storage capacity. Likewise, fully charging the battery can quickly damage it. According to [190] and [191], when battery is cycled in a SoC range below 20% and above 80% the fastest capacity fade occurs, this means that for an aged battery cell, an apparent 100% SOC would be equivalent to a 75%–80% SOC of a new cell [192].
In the next section 4.3, this double frequency separation strategy is refined to develop the gain scheduled filtering that includes battery SoC management via optimization technique.

4.3 Developed EMS strategy : Gain scheduled Filter

For a multi-source system, the aging process of the different units and the minimization of the fuel consumption cost are two essential criteria to be taken into account in the EMS. On one hand, the degradation of the various components largely affects the cost, the efficiency and then the performance of the whole system. On the other hand, the fuel consumption represents a high share of the system operating cost. Thus, optimizing both the degradation rate of the system units and the hydrogen consumption cost would be of a great interest especially when this is embedded within an EMS designed for battery SoC management. In this context, the proposed management strategy aiming at a better distribution of the requested power, meets these crucial requirements based on a cost optimization between the hydrogen consumption and the battery aging. The strategy fundamentals are first explained, then the design method is next detailed.

4.3.1 Strategy fundamentals

It's worth to recall that one of the main targets of this EMS approach, besides ensuring the power balance in the system, is to keep the battery state of charge within its limits while optimizing the hydrogen consumption and the battery aging. Hence, the battery and the fuel cell are the two specific units concerned by this optimization. Suitably, the main interest is to find a way to directly influence on these low to medium frequency

parts. In fact, the two main factors that influence the output of a low pass filter are its cut-off frequency and its gain. The next subsection compares the impact of changing the filtering frequency from one side with changing the filtering gain from the other side.

Case of frequency variation with fixed gain

Figure 4.4 represents the input and output of a low pass filter undergoing a cut-off frequency variation. On the left in the frequency domain, consider the input of the filter a signal with 3 different frequency components ω_1, ω_2 and ω_3 of the same amplitude. On the right, the output signal is illustrated. Note that green is referred to the filter response when applying ω_{c_1}, while blue represents the filter response when applying ω_{c_2}. Obviously, lowering the cut-off frequency from ω_{c_2} to ω_{c_1} attenuates or rejects only the signals with frequencies higher than ω_{c_1}, where all the frequencies lower than ω_{c_1} maintain their amplitudes, e.g. the frequency component ω_1. We can clearly see that this phenomena have a limited impact especially on the low to medium frequency signals (since no direct effect on the frequency component ω_1).

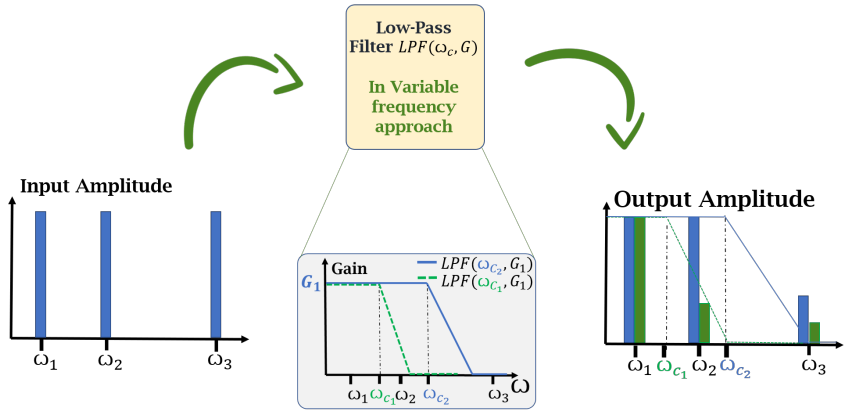

Figure 4.4 – Describing the frequency variation response of a low pass filter.

Case of a gain variation with fixed frequency

Figure 4.5 represents the input and output of a low pass filter undergoing gain variation. Note that orange is referred to the filter response when applying G_2 as a gain, while blue represents the filter response when applying G_1. Needless to say, lowering the gain from $G_1 = 1$ to $G_2 < G_1$ affects straightforwardly the amplitude of signals with all

frequencies and more specifically it targets the low to medium frequency signals by which the fuel cell and the battery are concerned respectively.

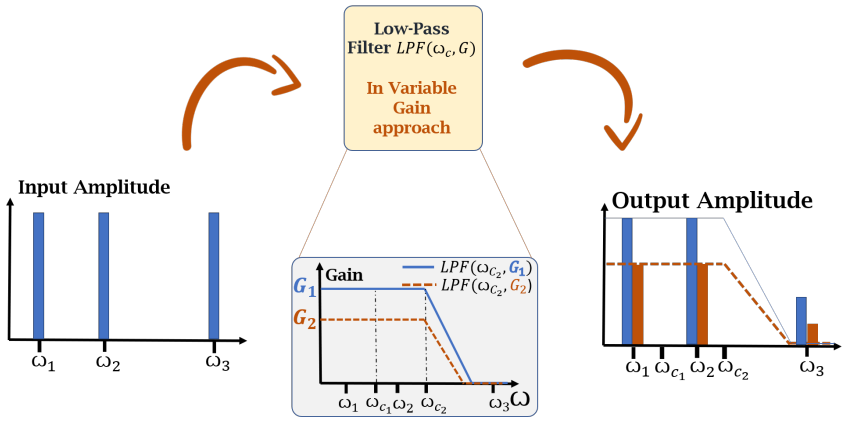

Figure 4.5 – Describing the gain variation response of a low pass filter.

Main EMS strategy principle

As mentioned, in the filtering EMS, the total current reference is distributed over multiple components, i.e, the FC, the Batt and the Sc, each one is meant to achieve its associated task, i.e, tracking its corresponding current reference. Indeed, forcing any of these components to achieve more or less than its assigned task, by varying the gain G, will be at the price of the other component. Hence, in this case an optimization problem should be inevitably considered to select, at a great extent, the best value of gain satisfying the system requirements. Therefore, when the battery SoC calls for an intervention due to an overcharging or deep-discharging, the act of varying the gain in the first low pass filter, i.e, meant to split the power between the fuel cell and the battery, allows to adjust the task's weight between the FC and the Batt. This implies a kind of role shifting between both of the two sources while respecting the following imposed operating constraints on the system:

$$\begin{cases} i_{st}^{*} = i_{FC} + i_{Batt} + i_{SC} \\ \mathrm{i}_{FC}^{min} \leq i_{FC} \leq \mathrm{i}_{FC}^{max} \\ \mathrm{i}_{Batt}^{min} \leq i_{Batt} \leq \mathrm{i}_{Batt}^{max} \\ \mathrm{i}_{SC}^{min} \leq i_{SC} \leq \mathrm{i}_{SC}^{max} \\ \mathrm{SoC}_{min}(20\%) \leq SoC_{Batt} \leq \mathrm{SoC}_{max}(80\%) \\ \mathrm{SoC}_{min} \leq SoC_{SC} \leq \mathrm{SoC}_{max} \end{cases} \tag{4.1}$$

Where i_{st}^{*} is the total reference current generated by the high level controller as explained in chapter 3, section 3.2, SoC_{Batt} and SoC_{SC} are the state of charge of the battery and the supercapacitor respectively.

The main idea of the proposed approach, is to make a gain scheduled filter where the gains are selected online upon operation, for example switched between 1, G_{min} and G_{max}. The gain $G = 1$ is referred to the normal operation when SoC value is lying into its safe defined range, whereas G_{min} and G_{max} are the gain values responsible for managing the battery SoC, those values are to be chosen based on solving an optimization problem that takes into account the battery usage cost and the hydrogen consumption cost. Then, in normal operation mode ($SoC_{min} \leqslant SoC_{battery} \leqslant SoC_{max}$) the selected gain is 1, i.e, as in the passive cascaded filtering. In overcharging case ($SoC_{battery} \geq SoC_{max}$), the fuel cell is called for a less involvement, thus the selected gain is chosen G_{min} (< 1) which translates into a hydrogen saving at the expense of more battery exploitation. In a deep-discharging context ($SoC_{battery} \leqslant SoC_{min}$), a request for increasing the fuel cell contribution is launched, thus the gain is chosen to be G_{max} (> 1), in this way less battery usage is obtained at the price of more hydrogen consumption as long as the hydrogen stock allows.

Figure 4.6 shows the proposed EMS diagram including its battery management, where the gain scheduling is done using two hysteresis relays and a switch. The hysteresis are meant to detect the situation in which the system is and thus generates the appropriate gain value. The Hysteresis Relay 1 helps to manage the battery during an overcharge whereas Hysteresis Relay 2 works in case of the battery deep-discharge. According to the battery SoC value, using the Hysteresis relays 1 and 2, the gain value is either G_{min}, 1 or G_{max}. The switch capture the gain value generated and then feed it to the cascaded filter block.

In general, the hysteresis has an essential role to play, since if the switch point and

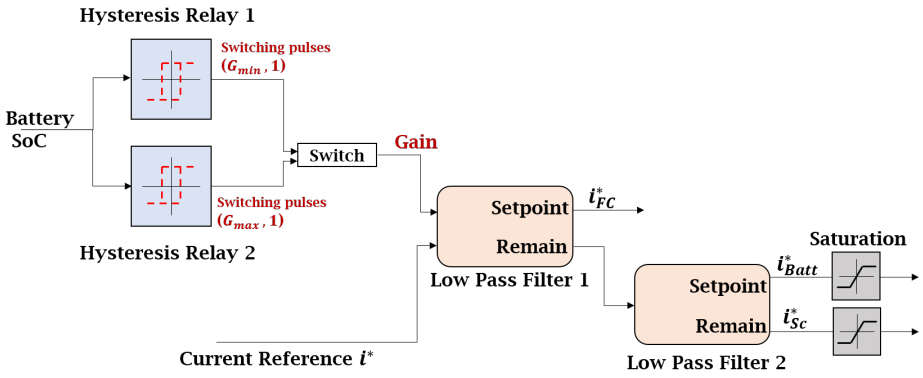

Figure 4.6 – Gain scheduled filtering EMS.

the reset point would be set to the same value, i.e. case of the normal switch, the system being controlled would oscillate and thus becoming unstable. In order to avoid oscillation, one needs to set a switch point different than the reset point suitably to the process, i.e. a defined hysteresis levels that lead to a stable control loop [193]. Therefore, the switching controller used has an integrated hysteresis to perform the gain transition in a smooth way.

In the EMS design, the safe operation range is defined when the battery SoC level is within 40% and 60%. The overcharging range is practically set when the SoC exceeds 75% to avoid considerably reaching the previously defined maximum safe limit in 4.1, i.e. 80%, and the deep-discharging mode is attained when SoC level decreases under 20%. Figure 4.7 illustrates the working principle of the hysteresis band control strategy of the proposed EMS. As already mentioned, the designed controller with hysteresis will not switch around the setpoint but outside the upper and the lower limit. For the overcharging case, when SoC exceeds the upper limit, i.e. 75%, the controller switches ON for the G_{min} value, this gain remains the same until a large enough SoC change, notably when SoC decreases to attains 60%, i.e. the reset point, the controller switches off and the gain value returns to 1 corresponding to the safe operation mode. On the contrary, for some potential operating reasons, when battery SoC level decreases and reaches the lower limit, i.e. 20% the switch point, the controller switches ON for the G_{max} value. It stays in this state until the Battery SoC recovers up to the 40%, i.e. the reset point, the controller switches back off and the gain value returns to 1 (normal and safe operation mode). Therefore, three zones are defined as shown in Figure 4.7, two hysteresis zones are referred to the over-charging and deep-discharging case and one dead zone in between the hysteresis zones is where the hysteresis relays are both inactive, it refers to the battery harmless operation mode.

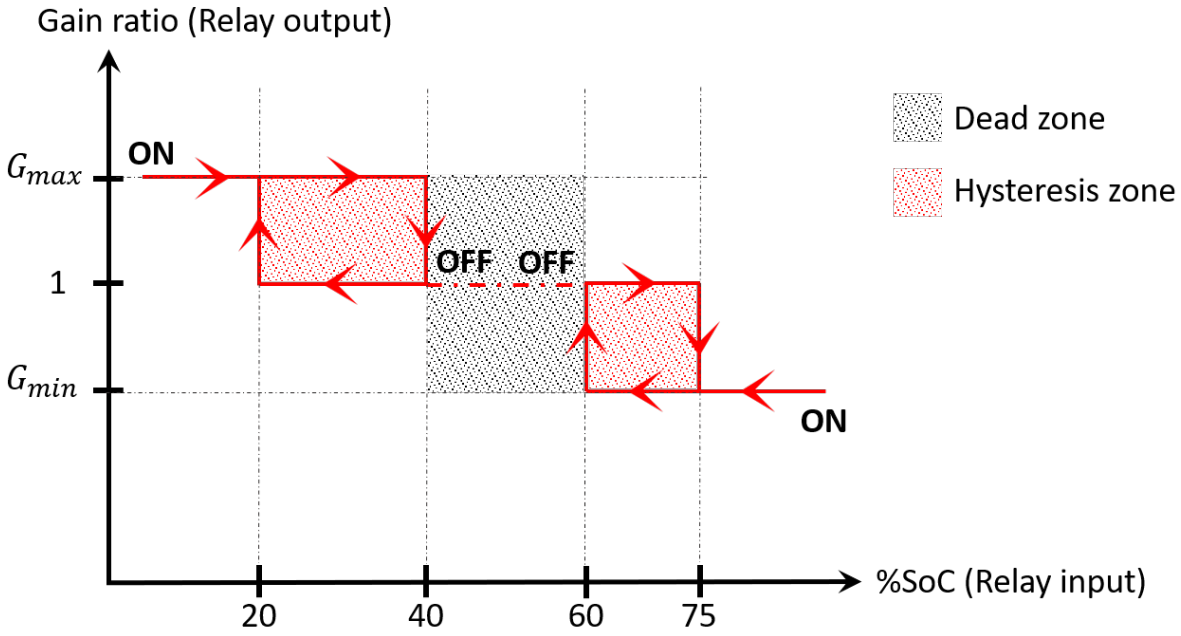

Figure 4.7 – Hysteresis band control strategy.

In order to perform this EMS approach and more specifically determine the relevant values of each of G_{min} and G_{max}, four critical steps are explained in section 4.3.2.

4.3.2 Gain calculation strategy

This section entails the design of the gain scheduled EMS. More explicitly, the three main steps followed to determine G_{min} and G_{max} are detailed. As already stated, each one of G_{min} and G_{max} is obtained through an optimization problem in charge of minimizing a cost function made of two main terms and subject to defined constraints. Three main steps constitutes the design phase of the EMS technique. Figure 4.8 presents a diagram recapping the three core steps to determine the quasi-optimal values for the filter gain, this gain permits the EMS system to handle the power dispatching task while managing the battery and the fuel cell with a fair compromise between the battery degradation and the hydrogen consumption.

Step 1 marks the data collection phase, step 2 and 3 concern the data analysis phase. In step 1, for each of the G_{min} and G_{max} case, a set of candidate gain values (< 1 in the case of G_{min} and > 1 in the case of G_{max}) is selected, then simulation of the controlled system is performed each time with a gain of this set and the data are collected for the

next two steps. In this way, each value of the candidate gain has a data set ready to undergo the optimization problem. Then comes Step 2 which consists on calculating and preparing the cost function terms. These terms express the hydrogen mass consumption cost and the battery usage cost. For the battery usage cost, two essential variables needs to be calculated, the severity factor and the equivalent full cycle of the battery that will be fully explained in the next subsection 4.3.2. The hydrogen consumption cost is estimated based on the current of the fuel cell which correlates with the hydrogen molar rate consumed within the fuel cell.

Finally, Step 3 concerns the normalization of the cost function terms, set the multi-objective cost function with its constraints in order to define the optimization problem. This optimization aims to produce the quasi-optimal values G_{min} and G_{max}. Note that the same design procedure can be done for both of the gain, the set of the candidate gain values is what differs the two cases.

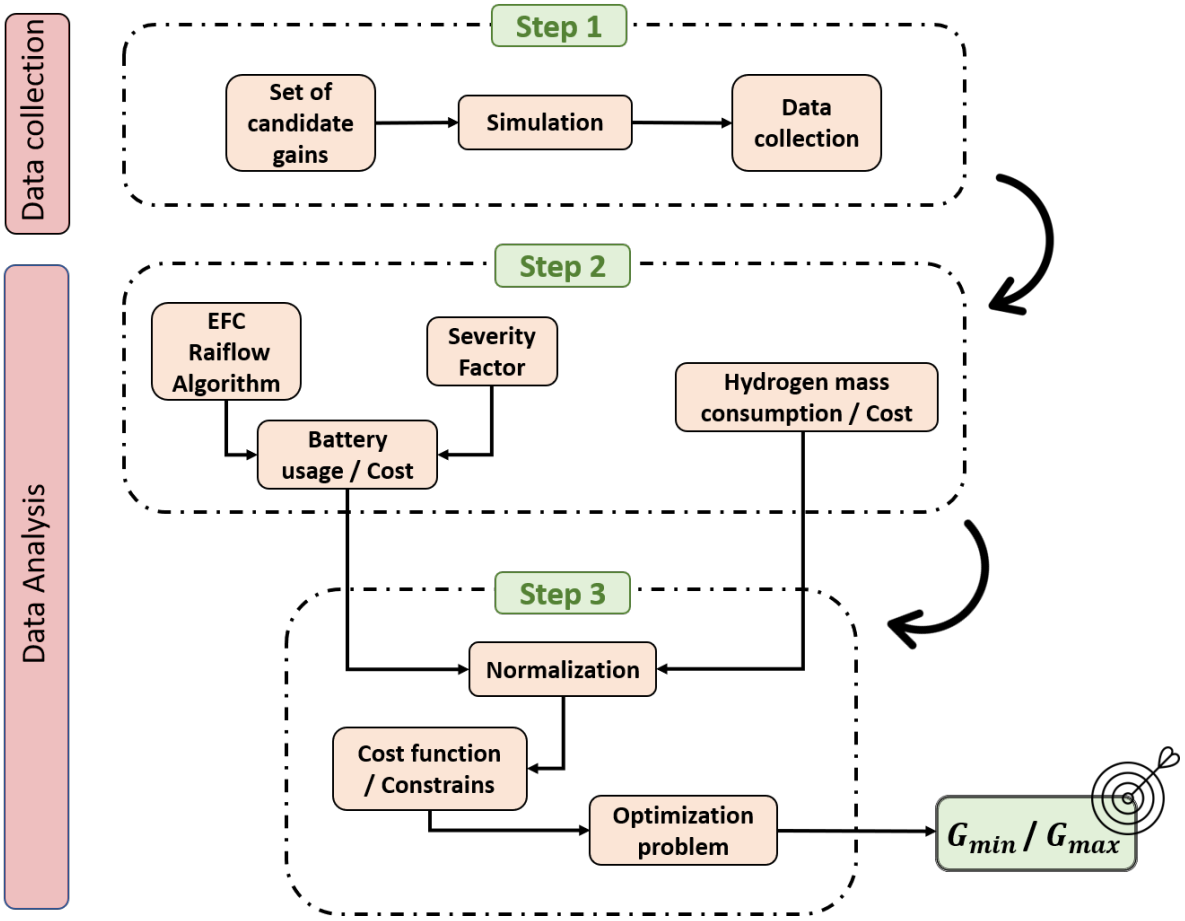

Figure 4.8 – Diagram recapping the followed steps for the gain value decision.

Battery usage

After comparing three categories of battery aging models in Chapter 3, this thesis has opted for the semi-empirical model due to the challenges associated with computation and calibration in the other models in case of limited amount of data.

In this section, the battery usage estimation, based on the equivalent full cycle calculation and the severity factor, is detailed.

Equivalent Full Cycle by the Rainflow Algorithm

Batteries have a finite number of charge-discharge cycles before their performance is expected to vanish. Once the maximum cycle count is reached, a battery replacement is recommended to maintain its performance. Therefore, the charging-discharging cycles along the operational time of a battery are directly responsible for its aging factor. Each cycle causes independent stress and the loss of the battery life is the accumulation of degradation due to all the cycles. To estimate cyclic aging, it is necessary to identify the cycles from the trajectory of the battery's state of charge (SOC). The Depth of Discharge (DOD), which refers to the absolute range of SOC excursion within a cycle, strongly affects the amount of aging [159]. The task of counting the number of cycles in a random dynamic profile might be challenging, as the depths of each cycle are typically quite diverse. This has been explored in [194], who have proposed some optimal solutions. Indeed, several methods for cycle counting are available in the literature ([195], [196]). However, in order to compute successfully the resulting cyclic aging, the counting mechanism has to determine the relevant macro- and micro-cycles where a precise and sophisticated cycle counting mechanism is required. In this work, the Rainflow cycle counting method is used to precisely detect cycles in a fluctuating battery state of charge (SoC) profile. The rainflow algorithm is a commonly used technique for identifying cycles in the analysis of material fatigue [197], as well as battery degradation modeling [198]. According to [199], [200], the Rainflow counting algorithm is very suitable for modelling battery aging. The Rainflow counting method is a generic cycle counting technique that can identify partial cycles from local extremum and extract range information from an irregular time series data, i.e. the battery SOC profile in battery cycles counting case [194], [201]. When used for battery life assessment, the Rainflow algorithm takes a time series of battery's state of charge (SoC) as input, and identifies the depth of all cycles contained in this series [202]. Various attempts have been made to simplify the algorithm process, either by simplifying

the rainflow counting method [203], [204], or by utilizing more straightforward cycle definitions [205], [206]. While these approaches enhance the solvability of the problem, they also introduce more errors and compromise the optimality of solutions. Figure 4.9 illustrates an example of the rainflow cycle identification outcomes for a battery SoC profile. There are three half cycles, one charging half-cycle (the orange one) is discontinuous in time. The green discharging half-cycle and red charging half-cycle are of the same cycle depth.

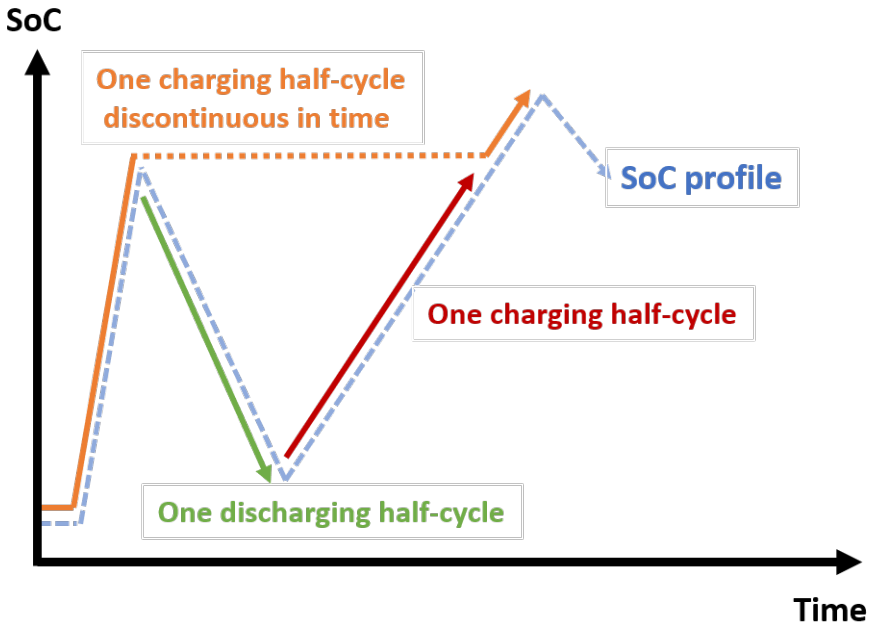

Figure 4.9 – Rainflow cycle counting example.

From the manufacturers point of view, an estimation of the lifespan of a battery is usually given as the total number of full charging-discharging cycles of the battery. Since the algorithm expresses the SoC variations (all the successive increases - decreases) as partial cycles at every given SoC range between 0 and 100%, hence, calculating the equivalent full equivalent charging-discharging cycles (EFC) based on the real partial variations of the battery SoC is then attainable using the rainflow algorithm along with coefficients (SOC range).

As reviewed in Chapter 2, the most popular real-time SoC level estimation, i.e. the coulomb counting method, is used in this EMS approach. By integrating the output

current signal of the battery, the SoC is estimated according to the equation bellow:

$$\mathrm{SoC}(t) = \mathrm{SoC}_0 - \int_0^t \frac{I_{Batt}}{3600 \cdot C_{Battnom}} d(t) \tag{4.2}$$

Where $C_{Battnom}$ is the nominal capacity of the battery, I_{Batt} is the battery current, and SoC_0 is the initial state of charge [207],[208].

Figure 4.10 serves as another example form of the rainflow algorithm output when applied on a random battery SoC profile. Indeed, the algorithm generates a bar graph representing the cycle counts at every SoC range. In this graph, it can be seen that for the near-zero SoC range (i.e for the small SoC variations) the rainflow algorithm counts a high number of cycles (965 cycles for a 0.0001% range) and it also shows, for instance, one cycle count at 55% of SoC range. Consequently, calculating the complete charge-discharge cycle, i.e. which is the equivalent full cycle (EFC) number of the battery, can be simply achieved by accumulating all the partial cycles counts while considering the SoC ranges as conversion coefficients, as generally expressed below in Eq.4.3. In such case, a single cycle count at a SoC range of 55% would contribute by approximately a half of cycle $(1 * 55\% = 0.55)$ to the EFC number.

$$Cycles_{100}\ (EFC) = \sum_{n=1}^{k} \frac{Range_n}{100} \cdot CyclesCount_n \tag{4.3}$$

where $Range_n$ is a given SoC range between 0 and 100, $CyclesCount_n$ is the number of the partial cycles at a given SoC range $Range_n$, $Cycles_{100}$ is the estimated number of the full equivalent cycles (EFC).

Battery usage with severity factor concept

In addition to the cycle counts, another critical factor that can greatly influence the battery life is its discharging/charging current level. The higher the current is, the more the battery is damaged.

Usually, the battery manufacturers define the lifetime of the battery as a number of cycles, the cycle term represent the full cycle (0-100%) under the nominal operating conditions: the nominal charge-discharge rate (C-Rate) $I_c = 1C$, depth of discharge DoD=100 %, the reference ambient temperature of the nominal cycle is $T_{Batt_{nom}} = 25°C$.

The total Ah-throughput symbolized as θ_{nom} under the nominal conditions and over a T period is defined by Eq.4.4:

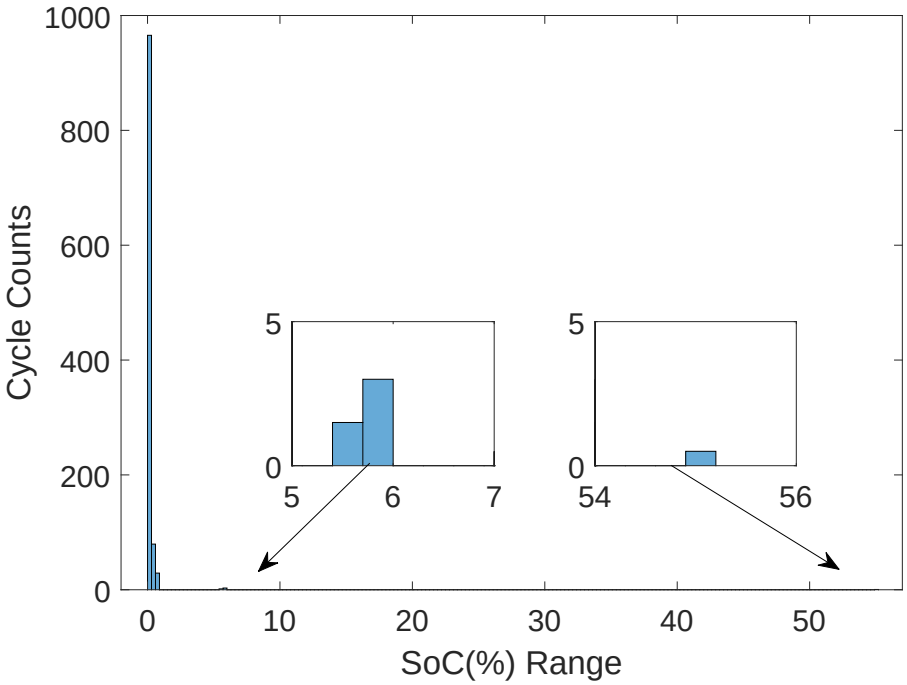

Figure 4.10 – Bar graph representing an output example of the Rainflow algorithm, Cycle counts vs SoC range.

$$\theta_{nom} = \int_0^T |I_{\text{nom}}(t)|\, dt \tag{4.4}$$

where $I_{\text{nom}}(t)$ is the nominal current under standard operating conditions.

For more accuracy in the battery usage estimation, the severity factor ρ, defined by eq. 4.5, is a factor used to characterize the aging effect of whatever cycle the battery goes through in comparison to its predefined nominal cycle. In other term, this factor represents the seriousness or the severity of the cycling usage.

$$\rho(I, T_{batt}, SoC) = \frac{\theta(I, T_{batt}, SoC)}{\theta_{nom}} = \frac{\int_0^T |I(t)|dt}{\int_0^T |I_{nom}(t)|\, dt} \tag{4.5}$$

where $\theta(I, T_{batt}, SoC)$ is the battery cumulative Ah-throughput corresponding to its measured current and temperature. θ_{nom} is the total Ah-throughput corresponding to the nominal cycle mentioned in Eq. 4.4. In view of the fact that the severity factor ρ expresses the relative aging effect with respect to the nominal cycle, a higher value ($\rho > 1$) reflects more severe operating conditions bringing the battery to shorter life and vice versa [209].

Given the equivalent full cycles count EFC calculated by Eq. 4.3 and taking into

account the severity factor given by Eq. 4.5 after ignoring the influences of battery temperature and SOC on the battery decay rate, the ratio of the battery consumption can be expressed in the following equation:

$$Usage_{Batt} = \frac{\rho \cdot Cycles_{100}}{Cycles_{life}} \tag{4.6}$$

Where $Cycles_{100}$ denotes the equivalent full cycles count in T period and $Cycles_{life}$ denotes the battery life cycle, i.e. the number of complete charge discharge cycles a battery can undergo before its capacity degrades to 80% of its initial capacity [210].

It is noteworthy that one of the innovative aspect of this EMS approach is the combination of the severity factor with the rainflow cycle counting for the sake of the battery aging estimation [211].

Hydrogen consumption

Inside the fuel cell stack, the hydrogen H_2 and the oxygen O_2 are consumed by the electrochemical reaction. The molar flow rate $\frac{dn}{dt}$ consumption of both hydrogen and oxygen is defined as follows:

$$\begin{aligned} \dot{n}_{H_2} &= \eta \frac{i_{FC} \cdot Ns}{2F} && [mol.sec^{-1}] \\ \dot{n}_{O_2} &= \eta \frac{i_{FC} \cdot Ns \cdot}{4F} = \frac{1}{2} \cdot \dot{n}_{H_2} && [mol.sec^{-1}] \end{aligned} \tag{4.7}$$

Where i_{FC} is the stack current in Ampere, Ns is the amount of cells mounted in series, F is the Faraday constant and η is the thermodynamic efficiency of the fuel cell (usually $\eta > 90\%$) [136].

The amount of exchanged electrons per mole H_2 is $2e^-$ for the hydrogen half-reaction; respectively $4e^-$ per O_2 mole for the oxygen half-reaction.

For a more intuitive use, the hydrogen consumption can be expressed as mass flow rate in $[kg.sec^{-1}]$ instead of molar flow rate $[mol.sec^{-1}]$. This can be simply achieved by multiplying Eq.4.7 by the molar mass of the dihydrogen $M_{H_2} = 2.016\ g.mol^{-1}$. The total amount of the hydrogen consumed over a specific period T can be obtained by integrating the hydrogen mass flow rate as follows [212]:

$$m_{H_2}(0 \sim T) = \int_0^T M_{H_2} \cdot \eta \cdot \frac{i_{FC}(t) \cdot Ns}{2F \cdot 1000}\ dt \quad [kg] \tag{4.8}$$

Cost function optimization

In this paragraph, the cost function for the optimization problem is first created, then the normalization used for rescaling the cost function terms is detailed.

Cost function

As described in the battery management strategy design, section 4.3.2, it is clear that there is a trade-off to make between the cost of the battery usage and the hydrogen consumption. Thus, the more the hydrogen is used the less the battery is needed and vice-versa. In other words, a higher dependency on the hydrogen of the fuel cell as a backup source implies less cycles and so less battery usage.

In order to optimize the use of each entity, a global multi-objective cost function is defined by eq. 4.9:

$$
\begin{aligned}
Cost_{Glob}(G) &= w_{Batt} \cdot Cost_{Batt}(G) + w_{H_2} \cdot Cost_{optH_2}(G) && (4.9)\\
Cost_{Batt}(G) &= Usage_{Batt} \cdot \varepsilon_{Batt} && (4.10)\\
Cost_{H_2}(G) &= m_{H_2} \cdot \varepsilon_{H_2} \\
Cost_{optH_2}(G) &= \begin{cases} Cost_{H_2}(G) - \phi, & if\ Cost_{H_2}(G) - \phi > 0 \\ 0 & elsewhere \end{cases} && (4.11)
\end{aligned}
$$

G is the filter gain, $Cost_{Batt}(G)$ is the battery consumption cost, ε_{Batt} is the cost of the battery pack in euros, $Cost_{H_2}(G)$ is the hydrogen consumption cost, ε_{H_2} is the cost of one kg of hydrogen in euros, $Cost_{optH_2}(G)$ is the hydrogen consumption cost counted in the optimization problem, Φ is the daily cost of the maximum allocated H_2 consumption with no imposed penalty. The penalty for excessive hydrogen consumption is only applied when the cost of H_2 consumption exceeds the predefined limit, which is the daily allocated budget Φ. The value of Φ is determined by the designer. Hence, H_2 consumption can be involved or not in the optimization problem upon its daily level. w_{bat} and w_{H_2} represent the weight values for each cost term. The choice of the weights values w_{bat} and w_{H_2} in the cost function allows to cast less or more importance on either the battery degradation cost or the hydrogen consumption cost.

In this optimization problem, a minimization of the predefined multi-objective cost

function is carried out, as described in Eq.4.12:

$$\begin{aligned} &\underset{G \in S}{\text{minimize}} \quad Cost_{Glob}(G) \\ &\text{subject to} \\ &x \leq G < 1 \qquad Case\ 1, \\ &1 < G \leq y \qquad Case\ 2 \end{aligned} \tag{4.12}$$

Where S is the proposed set of candidate gain values, for case 1 (battery overcharging situation) $S = [x; 1[$ where x represents the minimum limit that guarantee the fuel cell participation even if the battery is fully charged, e.g. if the designer chooses x=0.2 this implies that the fuel cell is at least involved by 20% in the energetic support with respect to the energy storage system units. For case 2 (battery deep-discharging situation) $S =]1; y]$ where y is the upper limit of the gain set that allows the fuel cell to provide additional power to recharge the battery when needed. One main factor that should be taken into consideration while defining this parameter is the maximum power of the fuel cell ($P_{FC_{max}}$) with respect to its nominal power when in normal operating mode (periods where G=1).

Certainly the more candidate gain values are chosen, the more accurate gain and closer to the optimal is obtained. According to multiple tests conducted on choosing different step sizes, it has been found that a step of 0.1 between each successive element of the gain set S can give sufficient information to localize the optimal value.

Normalization

Basically, the battery usage and the hydrogen mass consumption terms, as measured, are extremely difficult to compare to each other and optimize, since they are measured in a different way and thus each one has a different unit. Therefore, the conversion of the battery usage and the hydrogen consumption into cost terms is a way to unify the units and hence facilitate the comparison. In spite of that, the different range of values of both terms can still inhibit the feasibility of comparison. This means that some items will count for more in the computation of the final score. For example, an average daily consumption cost of a habitat may be less than 0.009 euros for the battery use, and more than 10 euros for the hydrogen mass consumption. Therefore, minimizing the total cost logically reveals the fact of using an insignificant quantity of hydrogen or even cut it off, which is not meaningful. Consequently, transforming the optimization problem into a form that is more suitable to solution is be made by converting the scales into

a common measurement scale, so that the terms' magnitudes become more comparable. Normalization is a scaling technique in which values are shifted and re-scaled so that they end up ranging between the same lower and upper limit, i.e. 0 and 1 (Min-Max scaling). This solution involves adjusting the scale on each variable like "stretching" some measures and "squeezing" others. For the studied terms, the conversion is achieved using these formulas:

$$Ncost_{optH2} = \frac{cost_{optH2} - Min(cost_{optH2})}{Max(cost_{optH2}) - Min(cost_{optH2})} \tag{4.13}$$

$$Ncost_{Batt} = \frac{cost_{Batt} - Min(cost_{Batt})}{Max(cost_{Batt}) - Min(cost_{Batt})} \tag{4.14}$$

The numerator term, i.e. $cost - Min(cost)$, helps refining the manipulation of the data in the optimization procedure. By reducing the minimum value from the all data values, only the data which are directly affected by the the gain variation are redirected into the optimization. While the denominator term, i.e. $Max(cost) - Min(cost)$ represents the range value of the term and works as a scaling weight.

4.4 Simulations and results

Numerical simulations have been carried out using MATLAB/Simulink, more specifically SimPower-Systems™ Toolbox, in order to evaluate the performance of the proposed EMS algorithm. System model specifications for this case study are all listed in the Appendix 5.12, and the load profile is the one used for the first case study in control simulation, Chapter 3, section 3.5.1, Figure 3.4.

4.5 Case Study

It should be stated that the proposed EMS concept is not exclusively for the studied system, it can be designed and adapted for any application regardless the microgrid structure or architecture. Without loss of generality, in the following some hypothesis and conditions are adopted for the simulation tests:

— This case study concerns the battery management in case of overcharging situation, since the battery deep-discharging situation is unlikely to happen with the

studied microgrid. But it should be recalled that the same concept and steps can be repeated for the deep-discharging management case in order to have a complete battery management system.

— The parameter x stated in Eq. 4.12 has been chosen to be equal to 0.2, i.e. an assumption of a minimum involvement of 20% of hydrogen fuel cell is considered since the FC is a mandatory backup source in this microgrid configuration.

— Φ is considered zero, thus the full H_2 consumption is always a part of the optimization problem (for simplification purpose).

— $\mathrm{SoC}_{min}(20\%) \leq SoC_{Batt} \leq \mathrm{SoC}_{max}(80\%)$ as a result, only 60% of the battery capacity is allowed to be used, this ensures optimal operating conditions in terms of aging ([213],[68]).

— Hysteresis limit values are selected as indicated in Figure 4.7 (Hysteresis ON state is at 75% SoC, Hysteresis OFF state is at 60% SoC).

— For an accurate study, one fixed value of initial battery state of charge SoC_0 is attributed to all the simulations (60%).

As reported in the summary diagram in Figure 4.8, in the first step simulations are performed for each value of the gain set [0.2-0,9] fulfilling the role of G_{min} in overcharging periods and $G = 1$ used in normal operation periods. At this stage, all data (e.g. Battery current, Battery SoC, Fuel cell stack current) are collected to be analysed in the following step . Figure 4.11 shows the profiles of the battery SoC obtained over 5 days of simulation. As shown in this figure, when the SoC value exceeds 75% the hysteresis control takes the ON action and starts forcing the battery to discharge until reaching 60%, where the hysteresis control takes the OFF action and reset the system in normal operation mode by applying $G = 1$. These profiles proves that the smaller the gain value is, the more deep and forceful battery discharge is performed.

A reasonable explanation is that when a lower gain is used in battery overcharging situation, the current reference of the fuel cell gets lower. Indeed this causes more involvement of the battery storage and therefore more deep discharge of the battery. Besides, the results show a nonlinear impact of the gain value on the battery SoC. By lowering the gain value from 0.9 to 0.7 the SoC variations are far more significant than lowering the gain value from 0.5 to 0.2.

Now in the data analysis part, the rainflow algorithm is applied on the SoC profiles represented in Figure 4.11. Figure 4.12 illustrates the outcome of the rainflow algorithm as a bar graph, i.e. the EFC the is calculated for each SoC profile over 5 days. The results

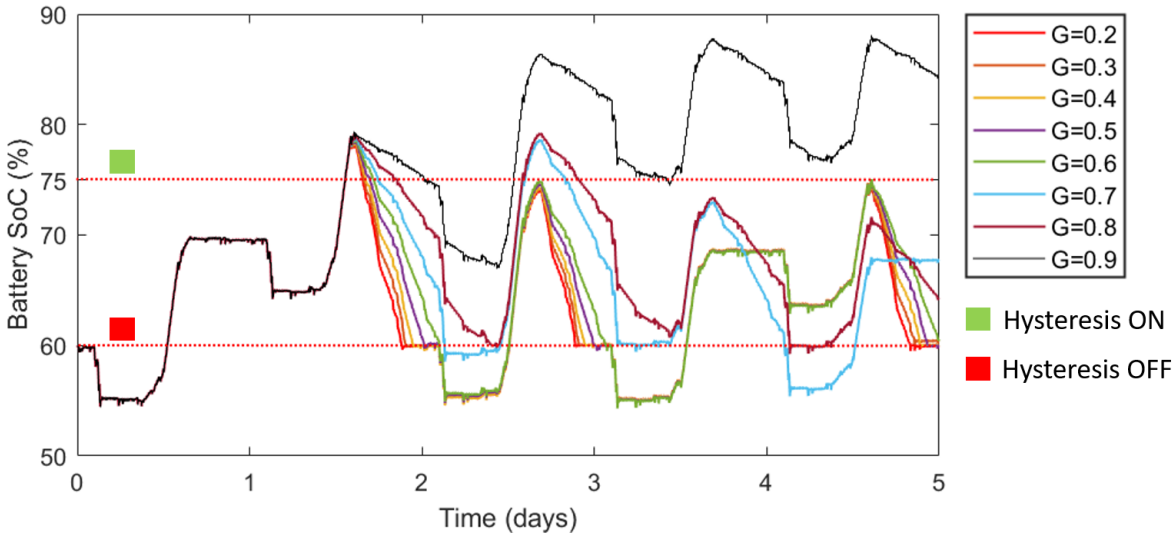

Figure 4.11 – Battery SoC profiles under different gain values of the set S.

show the impact of each gain value on the battery cycles. As already analysed, lowering the gain implies more battery participation, this is revealed by more equivalent full cycles associated to the lower gains.

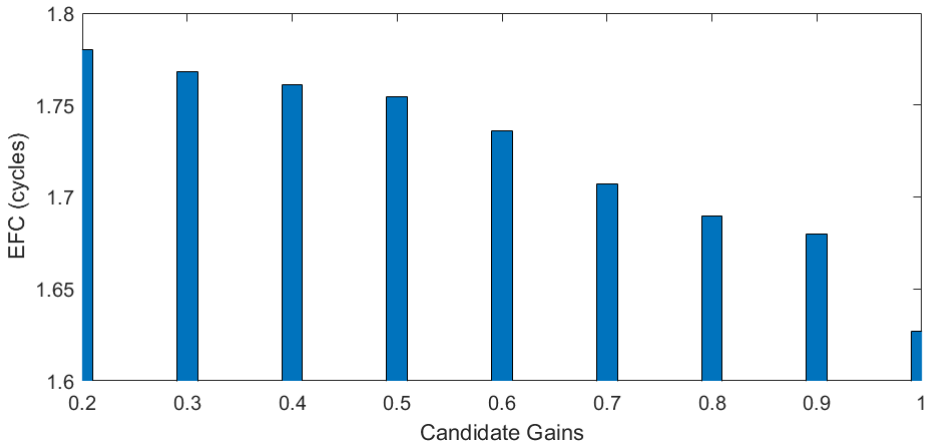

Figure 4.12 – Equivalent full cycles over 5 days.

Based on the battery usage, the battery cost equations defined by Eq.(4.6, 4.10) and the market price of the battery pack, the battery usage cost (in euros) is estimated for each gain value. And likewise, using Eq.(4.8, 4.11) for hydrogen mass consumption and the market price of the hydrogen [214],[215]), the hydrogen mass consumption cost (in euros) is estimated for each gain value. In the third step, the normalization of both cost

terms are executed, then the global cost is derived.

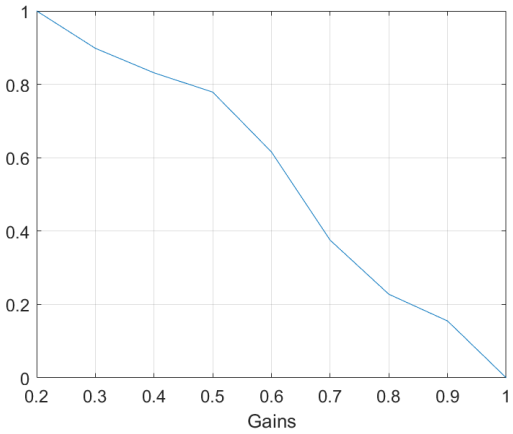

Figure 4.13 – Daily normalized battery usage cost.

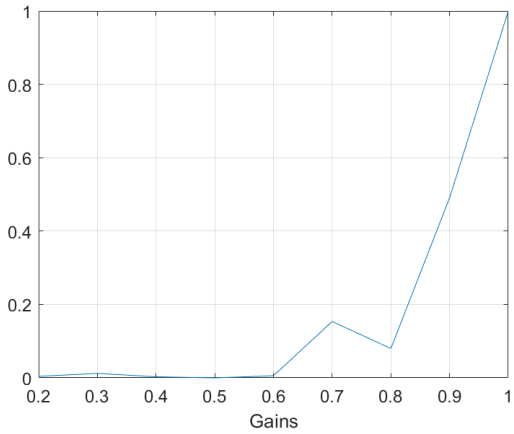

Figure 4.14 – Daily normalized hydrogen consumption cost.

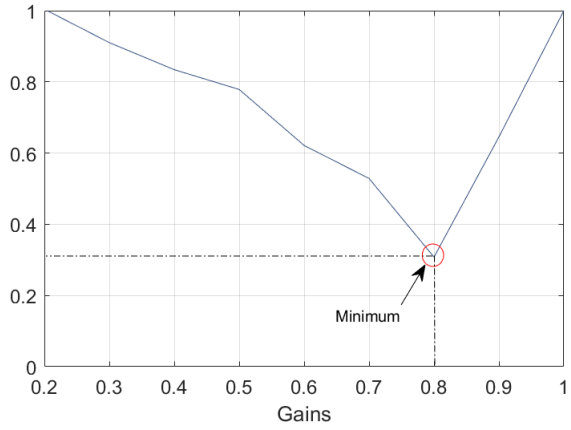

Figure 4.15 – Global normalized cost.

Figure 4.13 shows the daily normalized battery usage cost, while Figure 4.14 shows the daily normalized hydrogen consumption cost. Decreasing the gain from 1 to 0.2 has two opposite effects on the battery and the hydrogen consumption, an increasing curve is assigned for the battery usage whereas a decreasing curve is assigned for the hydrogen consumption. From these two figures, one notice that decreasing the gain value from 1 to 0.8 significantly reduce the hydrogen consumption while slightly increasing the battery usage. Beyond G=0.8, decreasing the gain value has a minor effect on the hydrogen consumption reduction, while on the other hand a great affection is recorded on the

battery usage. This highlights a more interest in lowering the gain from 1 to 0.8 since it leads to a drop in the hydrogen consumption cost while maintaining an almost steady battery cycling. An optimal choice of the gain value must take into account a trade off between the battery usage cost and the hydrogen consumption cost. Figure 4.15 shows the global normalized cost profile that should be minimized according to its corresponding constraints. The weights for each term have been chosen to be equal to one ($w_{Batt} = w_{H_2} = 1$), this does not mean that equal importance are given to both of the cost function terms, but on the contrary what is considered is the scaling weight in the normalization process indicated in Eq. 4.14 and 4.13. The gain value $G_{min} = 0.8$ pinpointed in this figure minimizes the global cost function. It corresponds to the closest to the optimal gain value. Eventually, in this study a switch between the gain value 0,8 and 1 is the best to be performed in order to manage the battery SoC while compromising the hydrogen consumption and the battery usage.

Figure 4.16 presents the online gain scheduling profile that refers to the studied case. This profile is the output of the switch block illustrated in Figure 5.30, it represents how the gain is being switched between 1 and the previously obtained quasi optimal value, i.e. 0.8, according to the system status. In other terms, it shows the periods when the gain is selected as $G = 1$ referring to the filter action in normal operation mode and when the gain is selected as $G = 0.8$ denoting the filter action in overcharging mode.

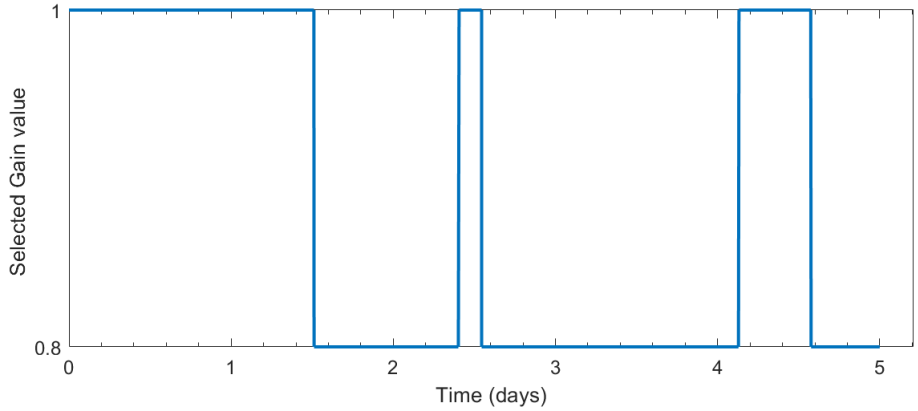

Figure 4.16 – Online gain scheduling profile.

To sum up the overall EMS strategy, Figure 4.17 represents a flow chart summarizing the working principle of the gain scheduled EMS. In the first part, an offline optimization problem is executed in order to find the best gain value fitting the demand for the battery SoC management according to the studied system. In the second part, an online measure-

ment of the battery state of charge is performed, analysed and then the gain is adapted to the right value that corresponds to the battery situation, this is done by the use of a hysteresis band control strategy. At each sample time, a measurement of the battery SoC is fed back to the control system to be managed.

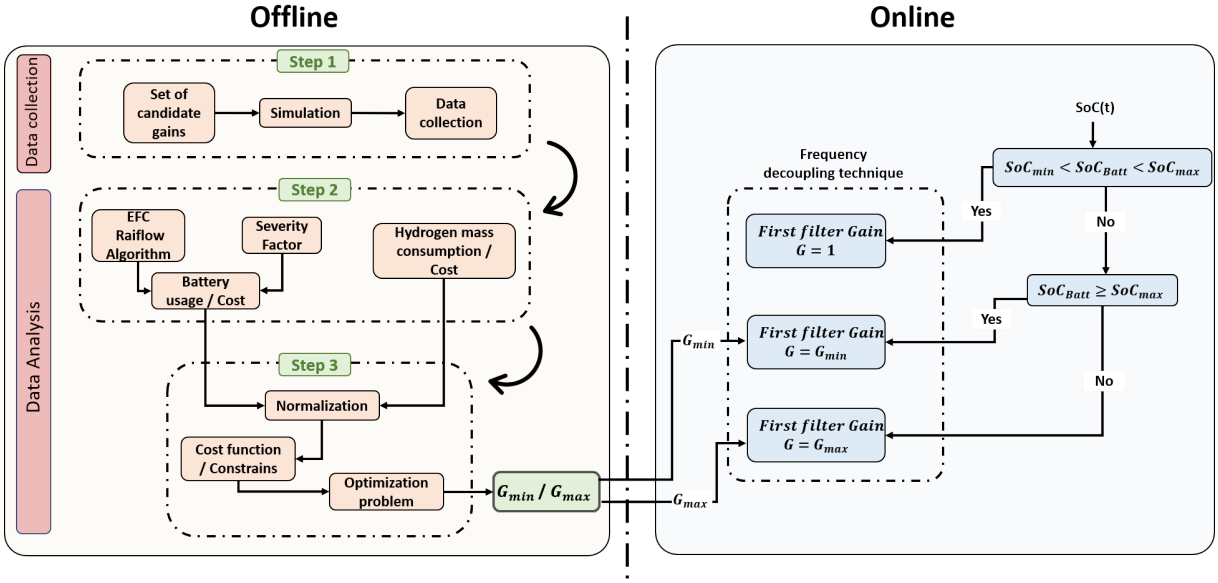

Figure 4.17 – Flow chart describing the working principle of the proposed EMS.

Figure 5.29 in Appendix 5.12 reports the overall diagram of the controlled microgrid produced on Simulink, where the proposed EMS strategy is implemented.

4.6 Performance evaluation of the proposed EMS

In order to assess the performance of the proposed EMS approach, comparison with respect to other EMS used in the literature is carried out. Two different EMS approaches, previously reviewed in the Chapter 1, are elected to be compared with the one studied in this thesis. These two EMS are the frequency decoupling approach, i.e. the classical EMS presented in [29] and the Rate-limiter based EMS developed in [131]. It should be pointed out that an identical simulation environment has been considered seeking a faithful comparison. Therefore, the same microgrid architecture, hypothesis and operating conditions were same applied on each of the simulated EMS approach.

Rate-Limiter EMS :

The theoretical framework of the Rate-limiter based EMS allows to achieve more efficient use of the different ESS components. According to [131], the Rate-limiter based EMS approach achieves better performance in terms of components' ageing rate compared to the frequency-decoupling EMS. This is achieved with less processing complexity by using a simple limiter in the algorithm. The basic principle is explained in Figure 4.18 through an example of power splitting between the Batt and the SC. Its main concept is to split the power demanded from the storage system $Pss(t)$ between the battery $P_{bat}(t)$ and the supercapacitor $P_{sc}(t)$ in such a way that the maximal power variation limitation is satisfied for each unit. This limitation is achieved by the saturation block defined by the parameter S_{bat} which is inherent to the technology used in the battery representing the battery's dynamical handling, i.e, the maximal power variation that can be achieved to make it working in its safe range.

$$\left|\frac{dP_{bat}}{dt}\right| \leq S_{bat} \quad \forall t \tag{4.15}$$

where ϵ is a time constant parameter that depends on the MG dimension. Note that, in this work this strategy is used in terms of current instead of power.

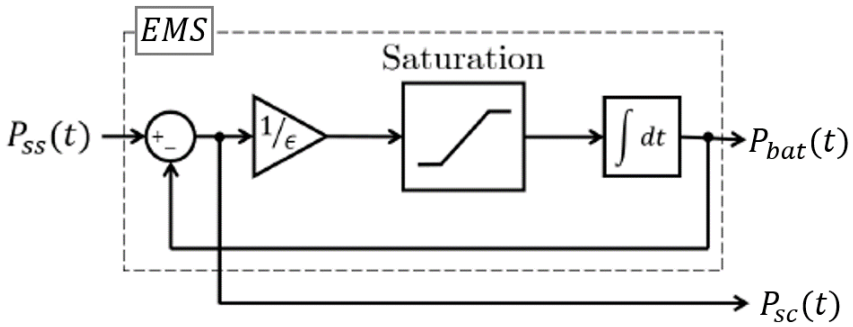

Figure 4.18 – Rate-limiter based EMS [131].

The comparison of the proposed EMS performance with the candidate ones is perceived in terms of battery usage and hydrogen consumption. Figure 4.19 is a comparative bar graph that shows the level of the annual battery usage (%) for each of the simulated EMS, the Rate-limiter based EMS shows the least annual battery usage 0.2% while the value recorded for the passive EMS is 1.75%. The proposed approach leads to a slightly increased value 1.8% with respect to the two other methods. On the other hand, Figure 4.20 represents a comparative bar graph for the H_2 mass consumption, the striking

difference between the proposed approach and the Rate-limiter based EMS can be crucially assigned to serve the proposed approach. Compared with the classical filtering EMS and the rate-limiter EMS, the proposed approach registers an annual hydrogen consumption usage of 35 kg while 40 kg is the H_2 consumption of the classical filtering EMS and 60 kg for the rate-limiter EMS. As demonstrated, the minor increase in the battery usage is nothing comparable to the significant decrease in the hydrogen consumption, hence the valuable advantage of the proposed strategy.

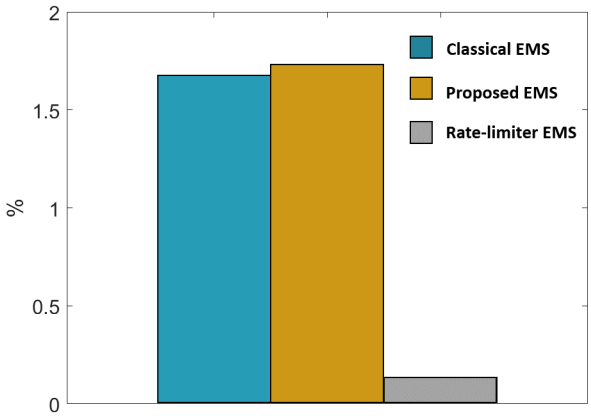

Figure 4.19 – Comparative bar graph for the annual battery usage.

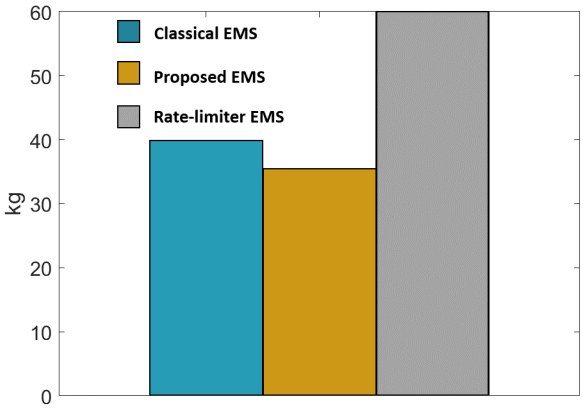

Figure 4.20 – Comparative bar graph for the annual hydrogen consumption.

4.7 Conclusion

In this chapter, an EMS strategy is proposed for the purpose of ensuring the balanced power distribution in the system and keeping up with the battery state of charge within defined target values. This is being addressed while optimizing the hydrogen consumption and the battery aging.

Simulation results prove that the proposed EMS has a satisfactory performance and confirms the theoretical expectation, this has been endorsed by comparative tests with two other EMS strategies already existing in the literature.

In the upcoming chapter, a hardware-in-the-loop (HIL) implementation of the proposed control structure will be applied on a test bench in the IREENA lab, considering multiple scenarios. The results of the experimental validation will be presented and analyzed to assess the performance and effectiveness of the proposed control structure.

Chapter 5

Implementation and experimental Validation

5.1 Introduction

In this chapter, an experimental validation of the MFSMC control algorithm is presented. The MFSMC control algorithm is discussed in Chapter 3 and is used to control a multiple sources system. The main objective of this chapter is to demonstrate that the control method is practical and can be implemented in real-time effectively. The chapter begins by introducing the architecture of the multi-source system. The different types of sources that will be used in the experimental implementation are discussed in detail. The second part of the chapter focuses on the test bench used for the experimental implementation. The design and construction of the test bench are described in detail, including the different types of sensors and measuring equipment used to monitor the performance of the system. The following section covers the implementation of the entire system using MATLAB/SIMULINK, dSPACE, and the real-time interface ControlDesk. The energy sources are connected to the Simulink model through the ControlDesk interface, which enables real-time data exchange between the hardware and software. Finally, the chapter presents the results of the experimental scenarios that were conducted to validate the control algorithm.

5.2 Microgrid architecture considered for the experimental validation

First of all, it is necessary to clearly define the hardware architecture of the microgrid system considered for the experimental validation. Since the purpose is to validate the control structure of the MFSMC algorithm, a microgrid setup with three controllable

devices (emulated fuel cell, battery and supercapacitor) is considered as enough for control system evaluation. Thereby, both of the outer voltage control loops and the inner current control loops are tested. A synoptic schematic of the hardware and the software of the HIL testing is shown in Figure 5.1.

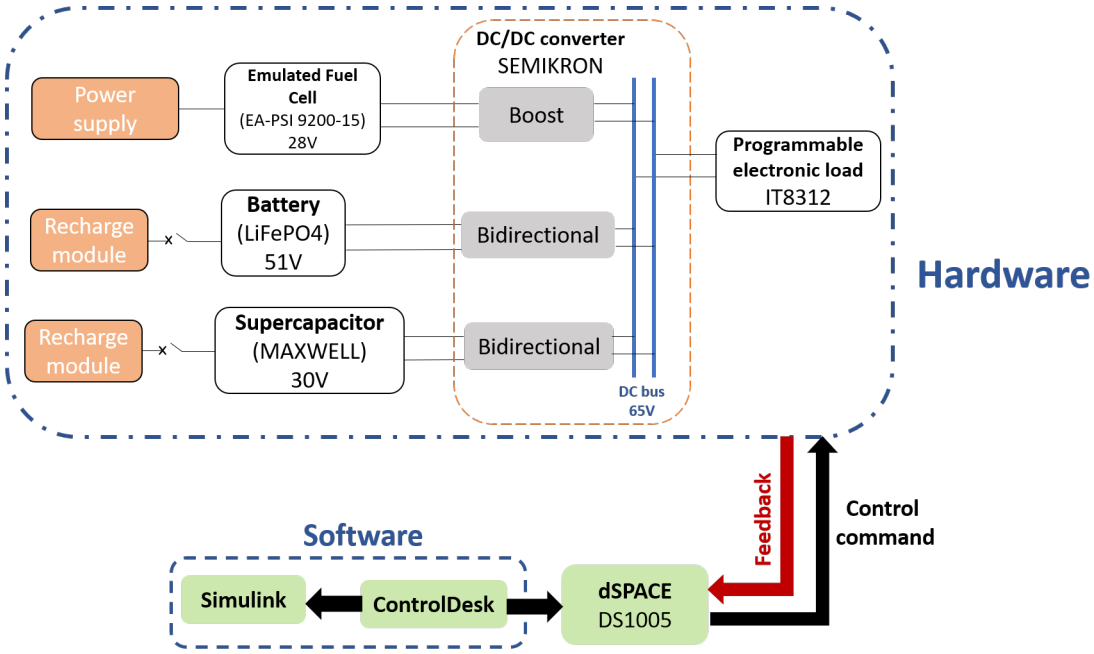

Figure 5.1 – Configuration of the experimental reduced-scale microgrid.

5.3 Test bench description

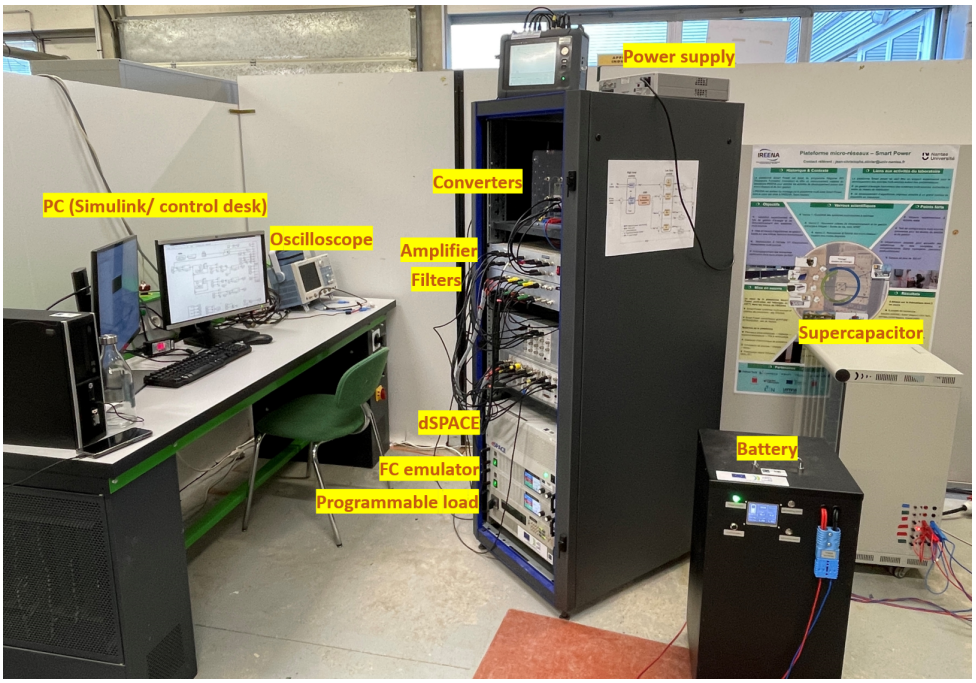

Figure 5.2 – Test bench overview.

In order to experimentally validate the obtained simulation results, we built up a test bench in our laboratory. It is important to highlight the hands-on involvement that was invested in building the testing bench. This involved designing the overall MG and assembling every component, from wiring connections to the integration of various hardware elements, ensuring that the testing bench was tailored to the specific requirements of our research. This direct engagement enhanced the validity and reliability of the results presented in this thesis. Figure 5.2 shows an overview of the test bench carried out. The IREENA laboratory test hall is already equipped with an emulated fuel cell emulator, a Lithium-ion battery and a supercapacitor bank. However, their energy dimensions are all different than those determined during the theoretical phase. These existing sources have been exploited in order to make use of the available equipment.

In terms of software, MATLAB/SIMULINK is used for the real-time implementation of the algorithm. Communication between Simulink and the real hardware is provided by a prototyping platform based on the dSPACE ds1005 system.

In the following section, a detailed description of the main elements used is provided.

5.4 Real equipment description

5.4.1 Energy sources

As previously mentioned, the energy sources used for the test bench are the ones that are already available. This includes an emulated fuel cell emulator system, a supercapacitor pack and a lithium-ion battery.

Fuel Cell Figure 5.3 represents the fuel cell emulator system (EA-PSI 9200-15) manufactured by EA Elektro-Automatik company. This system mimics the behavior and performance of a fuel cell without actually using one. Generally, it is cost-effective and safe alternative to using a real fuel cell. This emulator can simulate the electrical output, current and voltage, and other characteristics of a fuel cell, allowing to study the performance of a fuel cell system. For emulation, two emulators of the same type are used in parallel. The total emulator system has a maximum output power of 2 kW, and it can provide a voltage range of 0-200V and a current range of 0-30A.

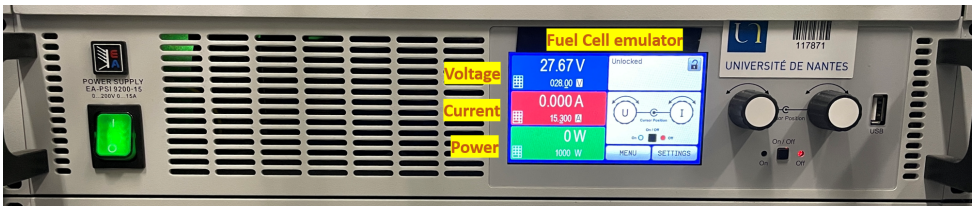

Figure 5.3 – Fuel Cell emulator.

Battery A LifePO4 lithium battery with a capacity of 100 Ah and a voltage of 51.2V, as seen in Figure 5.4, is used. Lithium iron phosphate (LiFePO4) batteries are known for their long cycle life, high thermal stability, and good safety performance. This type of battery is typically used to cover medium power demands.

Supercapacitor The utilized supercapacitor pack consists of 8 individual MAXWELL modules with a capacity of 58 F/15 V. They are organized into four pairs connected in series. Together, the assembly forms a pack of 116 F with a voltage range of 0 to 30 V. Figure 5.5 displays the specific module and pack configuration used.

Figure 5.4 – LifePO4 lithium battery.

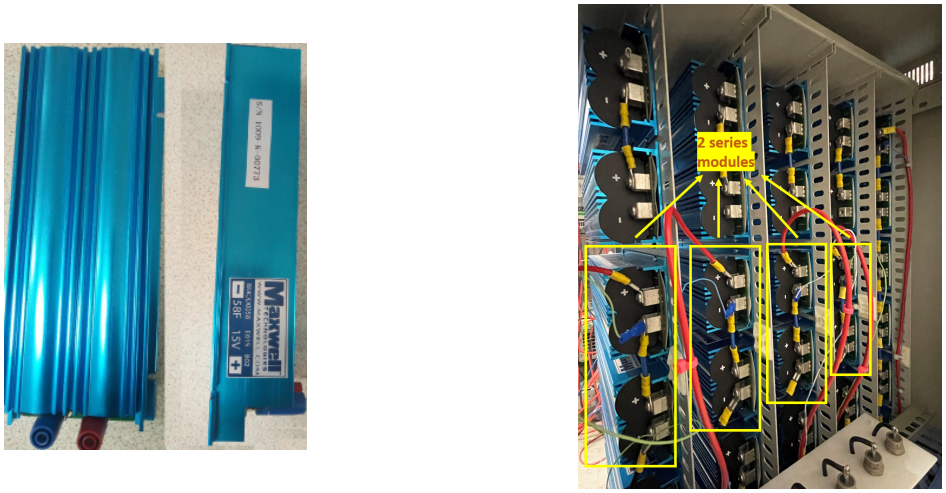

Figure 5.5 – Supercapacitor module (left) [161] and supercapacitor pack (right).

5.4.2 Electronic power converters

The DC bus is connected to all energy sources through specific DC-DC converters. The fuel cell is connected to a unidirectional converter to protect it from reverse currents, while the battery and the supercapacitor are linked to the DC bus through two bidirectional converters. A SEMIKRON educational inverter, as shown in Figure 5.6, has been modified and used as three parallel DC-DC converters that are connected to the DC bus on the test platform.

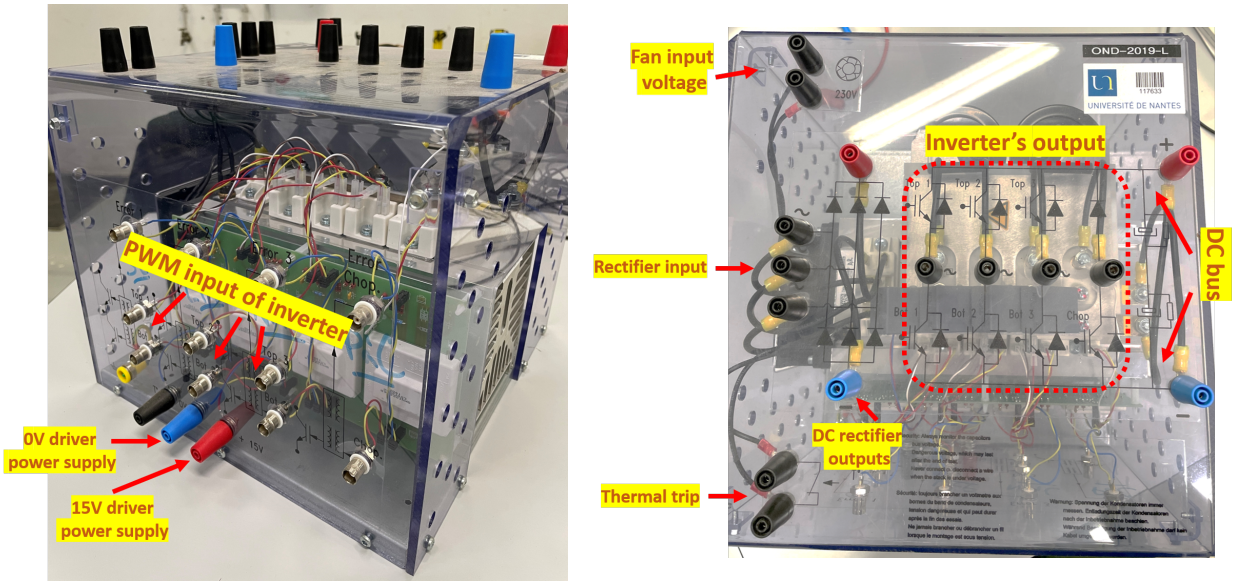

Figure 5.6 – Side and top view of the SEMIKRON inverter.

5.4.3 dSPACE system

Figure 5.7 – dSPACE system DS1005.

dSpace is an interface that connects the simulation environment provided by Simulink to the physical hardware system. This hardware-in-the-loop (HIL) simulation platform, developed by dSpace company, is a powerful, flexible, and compact platform for the development and testing of electronic control systems. In our test bench, the dSPACE version used is the DS1005 shown in Figure 5.7.

The dSpace DS1005 platform features a variety of interfaces as represented in input/output cards in Figure 5.8. There are two types of interfaces:

— Analog interfaces that can be used, depending on the chosen configuration, as inputs for acquiring signals from analog sensors or as outputs for actuators generating

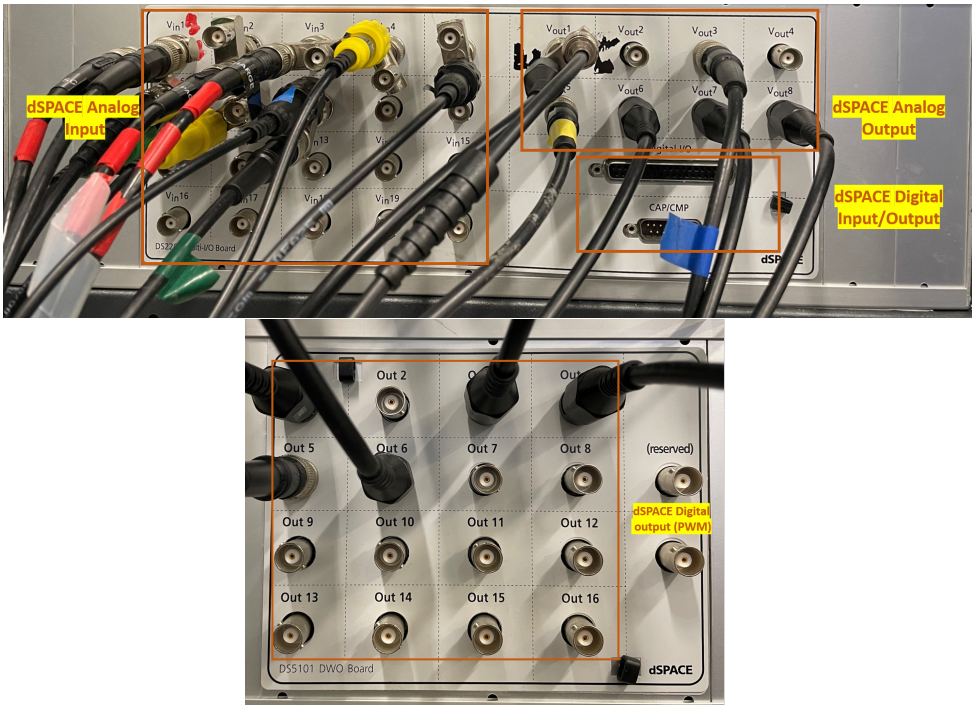

Figure 5.8 – Digital and analog dSPACE input/output

signals in analog control systems. Each port of this interface has a 12-bit analog-to-digital converter (ADC) for an input configuration and a digital-to-analog converter (DAC) for an output configuration (8 analog outputs and 20 analog inputs).

— Digital interfaces can be employed for both input and output, depending on the configuration. When configured as outputs, digital interfaces can also act as PWM generators, to control the power transistors of converters (16 PWM outputs).

5.5 Programmable electronic load

In order to impose a given load consumption profile, a controllable electronic load shown in Figure 5.9 is used. The regenerative electronic load IT8312, manufactured by ITECH electronics, is a versatile and powerful programmable load controller that can be used to simulate a wide range of electrical loads. It can simulate different types of loads such as resistive, inductive, and capacitive loads, and it can be programmed to simulate different load scenarios, such as constant power, constant current, and constant voltage. It has a maximum power of 3.5 kW. It can absorb up to 20 A. Its maximum voltage is 800 V.

Figure 5.9 – Programmable electronic load.

The current absorbed by the load can be controlled by an external potential difference applied to the EXT PRG analog terminals located on the back side of the programmable load, as shown in Figure 5.10, where a voltage of 10 V corresponds to the maximum charging current (20 A).

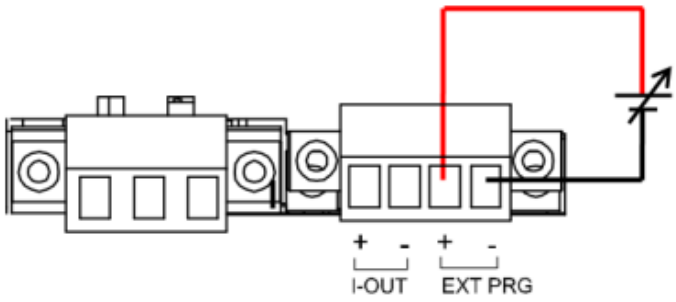

Figure 5.10 – Adjustable voltage connection for load current control.

This adjustable voltage is sent by an analog output of the dSpace system using the DAC (Digital to Analog Converter) module.

5.6 Sensors

Voltage and current control loops requires real-time measurement and magnitude acquisition. In our test bench, these measurements are ensured by different types of sensors. Thereby:

— Four LEM LA25-NP type sensors grouped on an acquisition card are used to measure currents for the the load and the three source. These sensors, with a current-to-voltage gain, provide output voltages between -10 and +10 V.

— Two MTX 1032-C differential probes are type of voltage sensors developed by the company Measurement Technology (MTX). Each sensor box has two differential

probes. These are used to measure DC bus voltage and source's voltage. With an input-output gain of 1:100, these sensors also provide a range of measurements between -10 and +10 V.

Figure 5.11 shows the types of current and voltage sensors used. These sensors are connected to the dSpace analog input cards through suitable conditioning circuits. The analog inputs are transformed into 12-bit digital signals for their usage with the dSPACE numerical computing system.

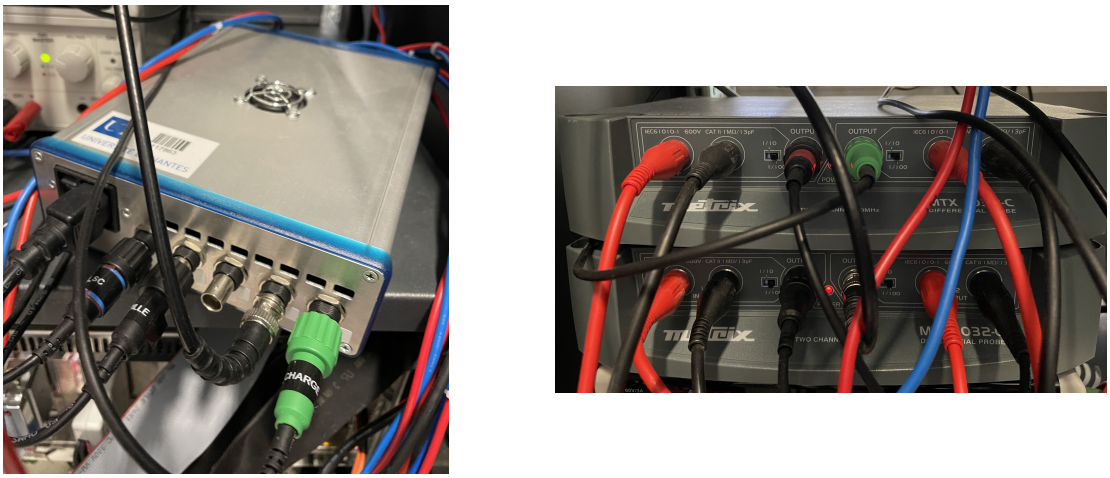

Figure 5.11 – Current sensors (left), Voltage sensors (right).

5.6.1 Inductance

As shown in Figure 5.12, three self-inductances 4mH with a maximum current of 10A each, are used to build the electrical circuits between the three sources and the DC bus.

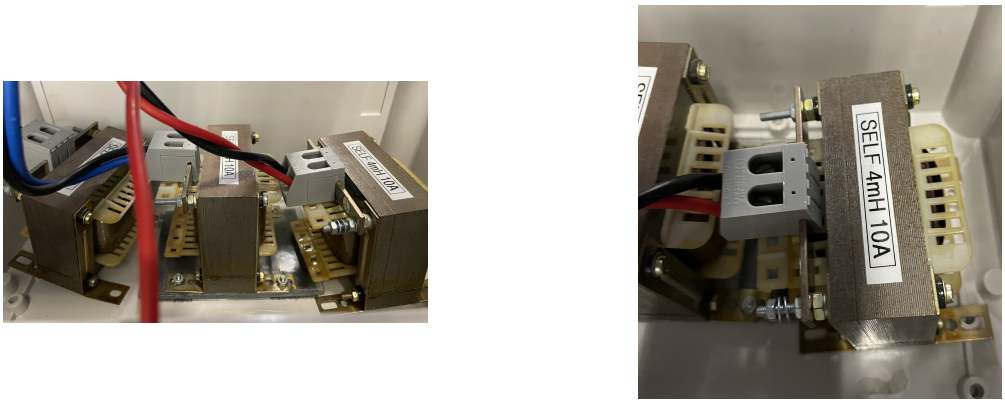

Figure 5.12 – The three inductance used (left) and the inductance unit (right).

5.6.2 Amplifier and filters

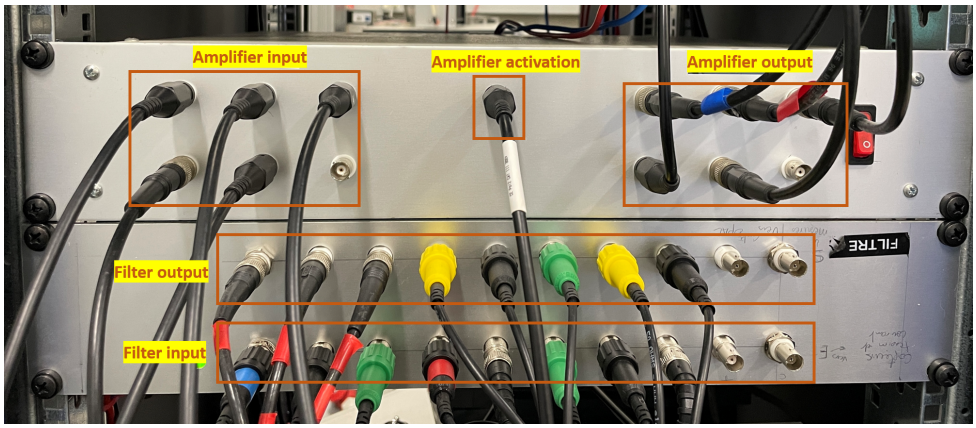

Figure 5.13 – Amplifier and filters.

Figure 5.13 shows both of the amplifier and the filters used.

Amplifier: In order to drive SEMIKRON DC-DC converters, which require a 15V turn-on voltage, an amplifier is necessary to amplify the digital PWM output signals from the dSpace DS1005's digital output pins, which only supply +5V DC voltage. This is because the amplitude of the digital PWM signals from the dSpace DS1005 needs to be increased before they can be used to effectively drive the SEMIKRON DC-DC converters. The amplifier activation is controlled by a command signal that will cause the RUN/Stop of the entire hardware system.

Filters: Anti-aliasing filters are commonly used in real-time interface (RTI) systems to remove high-frequency noise or "aliases" from a signal before it is digitized. By setting the cutoff frequency slightly lower than the highest frequency of interest, the anti-aliasing filter avoids the aliasing effect, thus improving the accuracy and integrity of the data acquired by the RTI system. It is typically used to improve the accuracy and integrity of the data acquired by the RTI system.

5.7 Real time Implementation

In terms of software, MATLAB/SIMULINK modeling tool is used for the real-time implementation of the algorithm. It helps to pose the problem in a graphical way using

the interconnected blocks.

The real time implementation can be grouped into four crucial steps

— Creating the control system by utilizing blocks from MATLAB/SIMULINK.

— Testing the system in various scenarios through simulation.

— Connecting and interfacing the inputs and outputs with the relevant sensors and actuators of the physical system.

— Running the model in real-time using the dSPACE board.

Once the program has been loaded onto the card, the user can modify certain parameters in real time, acquire and record data using a Human-Machine Interface developed with the ControlDesk software and supplied with the dSPACE system.

5.7.1 Simulink Scheme for the RTI Implementation

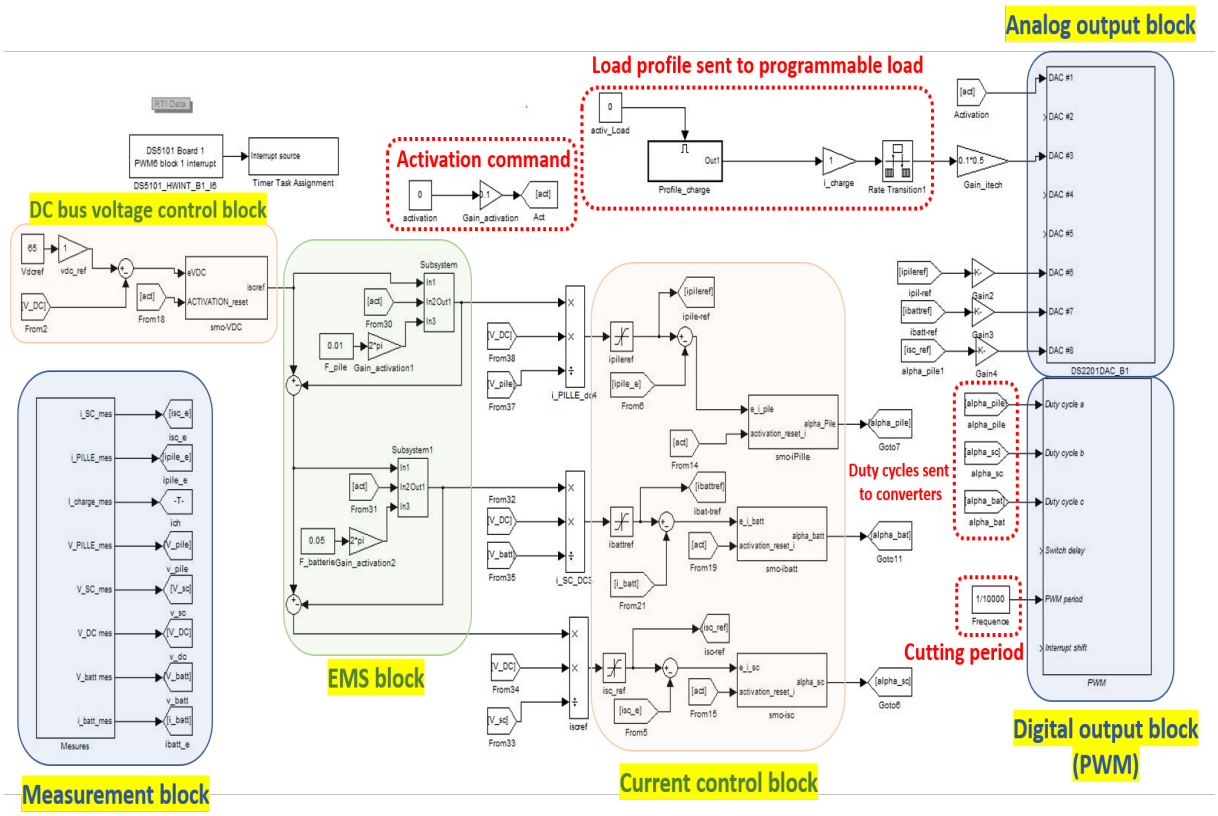

Figure 5.14 – Simulink diagram for dSPACE.

In order to test and evaluate the performance of the MFSMC control strategies developed in Chapter 3 on the test bench, it is necessary to adapt the control-command

diagrams created on SIMULINK by integrating the input-output interaction information of the dSPACE system. Figure 5.14 shows the final adapted SIMULINK model with input-output interfaces. This model has, in addition to the voltage and the current Control loops (Made up with the proposed MFSMC) and the EMS blocks, the following blocks:

— An analog output block for sending the load profile to the programmable load and the activation command directly to the amplifier.

— A digital PWM output block for controlling the converters associated with the different sources.

— A data acquisition block, or measurement block, that ensures the acquisition of sensor data.

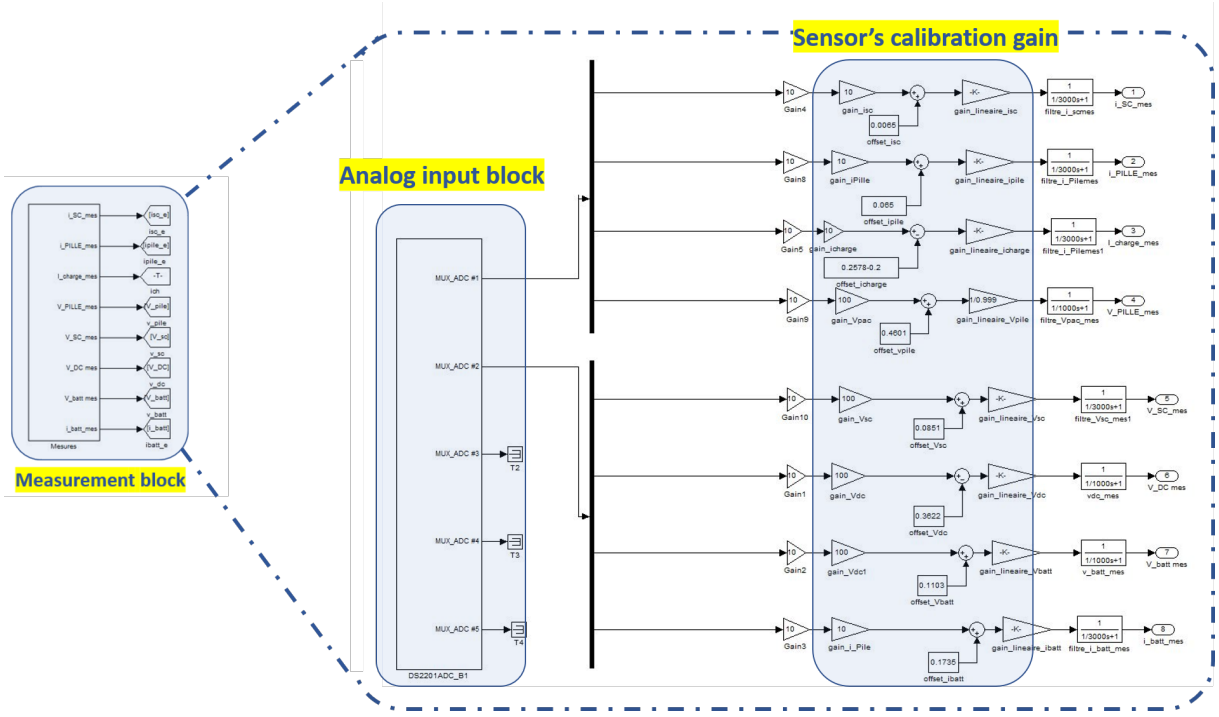

Figure 5.15 – Data acquisition block.

The data acquisition block, illustrated in Figure 5.15, is basically built of an analog input block. This latter includes 8 inputs for current and voltage sensors from the three sources (fuel cell, battery, and supercapacitor), the voltage of the DC bus, and the load current.

Without proper calibration, a sensor can produce inaccurate or inconsistent readings, which can lead to incorrect decisions or actions based on the sensor's output. Therefore, a series of test measurements taken over a range of conditions for each sensor are made

in order to adjust it. The results are used to generate a calibration curve then extract the corresponding linear gain and offset to be applied to the sensor's output.

5.7.2 ControlDesk

ControlDesk is the software development tool that is used in conjunction with the dSpace ds1005 hardware platform. It provides a graphical user interface that allows users to quickly set up and test control systems by giving a single working environment, from the start of experimentation right to the end.

ControlDesk provides a number of features that make it easy to develop and test control algorithms, such as:

— Real-time execution: ControlDesk allows control algorithms to be executed in real-time on the dSpace hardware platform, which enables an accurate testing and validation of the control algorithms.

— Data logging and visualization: ControlDesk provides a range of tools for logging and visualizing data, which can be used to analyze the performance of the control algorithms and identify any issues that need to be addressed.

— Parameter tuning: ControlDesk also provides tools for tuning the parameters of the control algorithms, which can be used to optimize the performance of the control algorithms.

Figure 5.16 represents an annotated configuration when controlDesk software was used for the experimental validation.

5.8 Real-time experimental results

This section is dedicated for presenting the experimental results of the real-time control testing scenarios carried out on the test bench. The adopted strategy of work consists of starting off by validating the current (low-level) control loops, then moving on to validate the whole cascaded (voltage-current) loops.

It is worth noting that since the goal of these real-time tests is to evaluate the performance of the proposed controller independently of any energy management strategy, a simplified energy management system technique, such as classical filtering, is used.

It is important to note that this test was carried out after making adjustments to certain controller parameters.

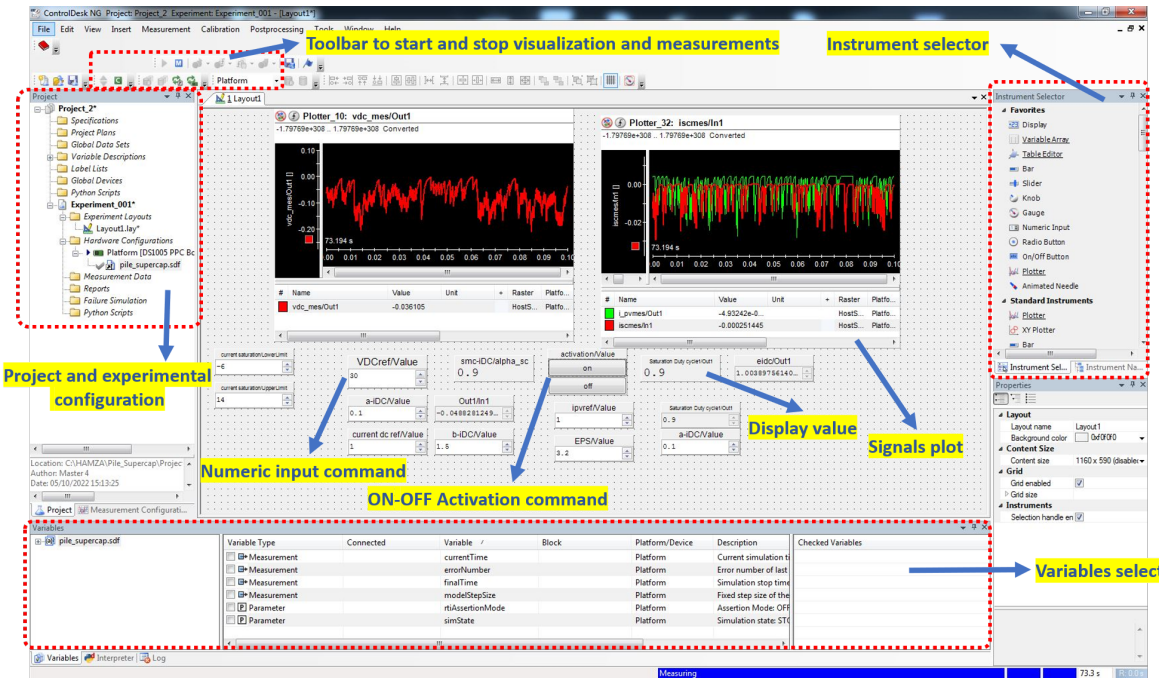

Figure 5.16 – ControlDesk configuration.

5.9 Scenario 1

This first scenario has been made in order to evaluate the performance of the DC bus voltage controller as well as the corresponding current controllers in tracking their assigned reference.

This test involves varying the DC bus voltage setpoint as the only testing factor on the system. This is associated in parallel with a constant load current. A DC bus reference signal of a a square pulse is sent to the DC bus voltage controller as illustrated in Figure 5.17. It is changing from 65V to 90V and back again to 65V after a period of approximately 30s. Figure 5.18 shows the second condition of this test, i.e. the measured load current after imposing a constant signal at approximately 5A for the entire duration of the test.

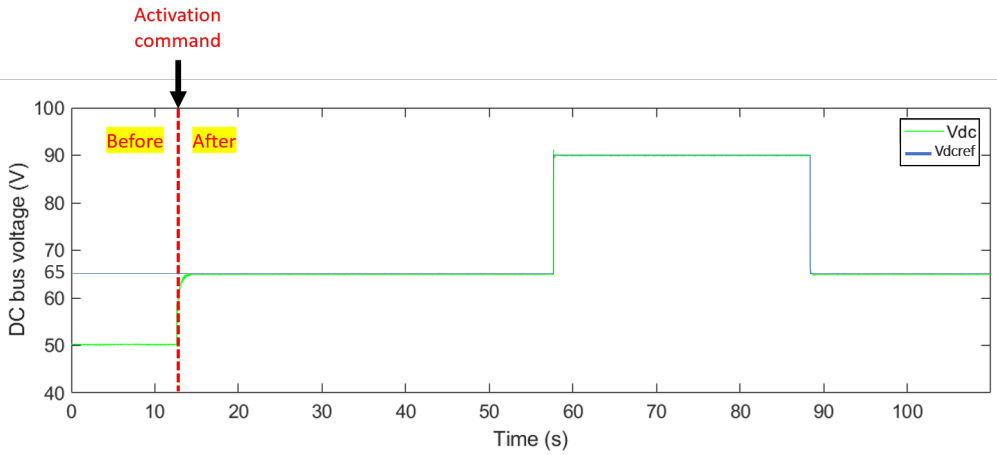

Figure 5.17 – DC bus voltage.

On Figure 5.17 it is pointed out the moment of the system activation, and it can be clearly seen how the system control was lost before the activation is ON (DC bus voltage is 50V where it should be 65V according to the setpoint). But when the activation command is ON, the DC bus is powered up and then the voltage starts rapidly responding to the imposed setpoint. The MFSMC controller demonstrates a strong capability to respond to changes in the setpoint, showcasing its high damping ability and system stabilization during the transient phase. Additionally, the controller exhibits accurate performance in the steady-state by closely following the desired reference value.

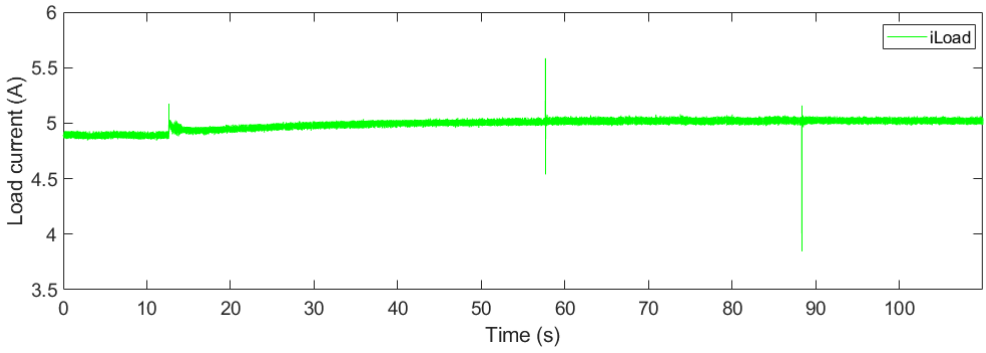

Figure 5.18 – Load current.

The currents provided by the emulated fuel cell, battery, and supercapacitor and their corresponding references are respectively represented in Figures 5.19, 5.20 and 5.21. The overall performance of the energy sources can be seen in the figures, with the emulated fuel cell supplying the lowest frequency current variations and showing a great tracking

performance. The battery and supercapacitor also show acceptable tracking performance, but with some tracking errors in the two phases of the DC bus voltage transition. The lack of sufficient supercapacitor current in the transient phase is partly compensated by the battery's response, as the measured current exceeds the reference values during these phases. Despite these tracking errors, they do not significantly impact the overall performance of the control structure, which is primarily focused on stabilizing the DC bus voltage. It is important to note that the initial transient response of the sources at around 13 seconds is a result of the system activation.

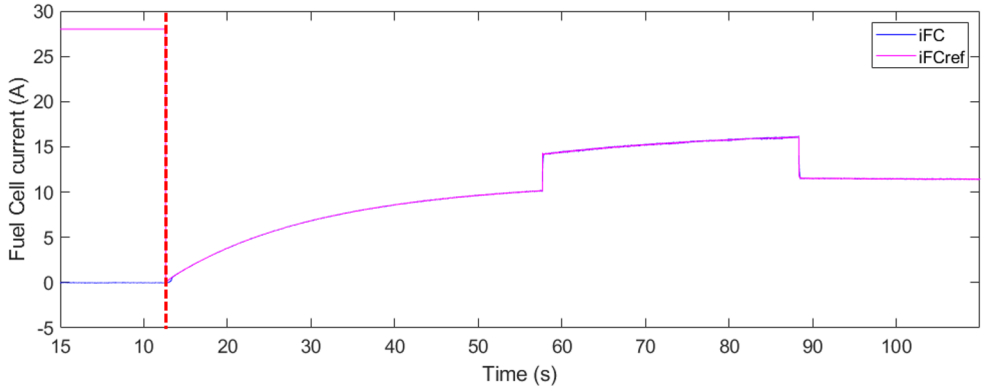

Figure 5.19 – Emulated Fuel cell current variations.

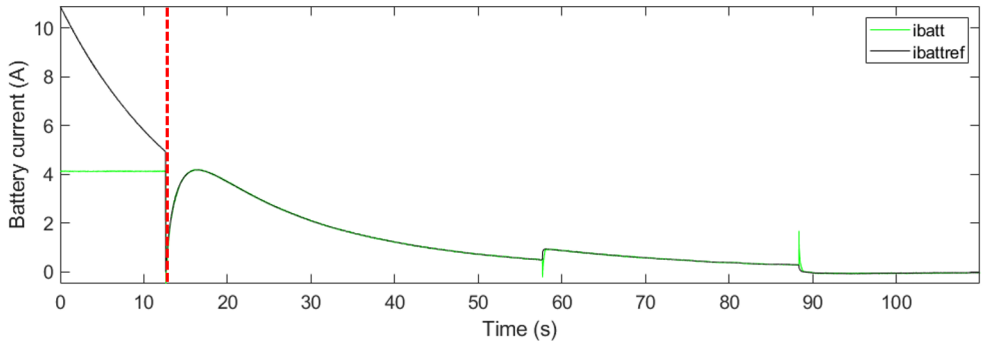

Figure 5.20 – Battery current variations.

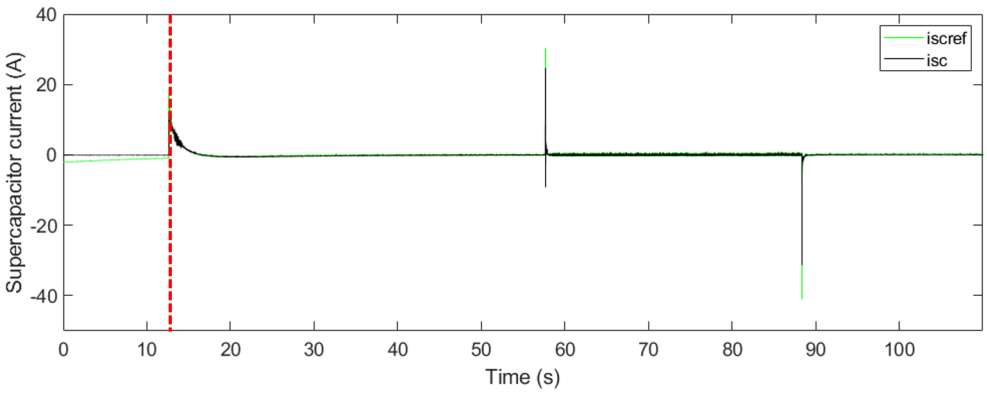

Figure 5.21 – Supercapacitor current variations.

Figure 5.22 shows the load power and the power distribution between the different sources. It is evident that during times of high power demand, the supercapacitor quickly supplies the majority of the power needed. The emulated fuel cell and battery, on the other hand, take longer to react, supplying the remaining power needed, all while also satisfying medium and low frequency power demands. The results of the experiments demonstrate that the EMS effectively allows a distribution of the power demand across the three energy sources in accordance with the chosen cutting frequency.

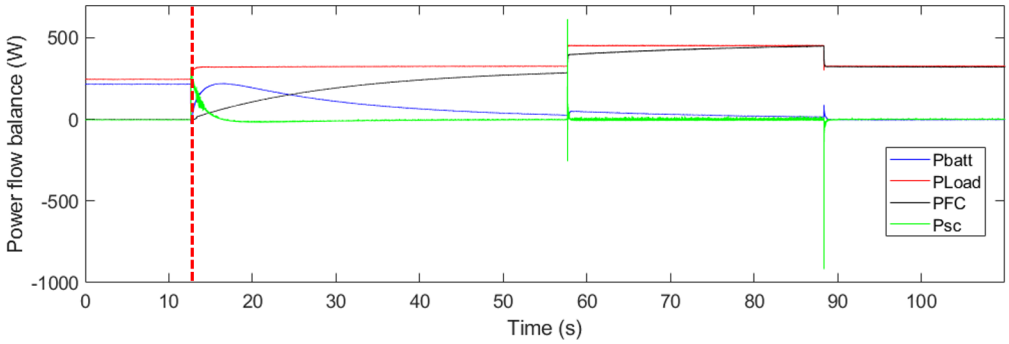

Figure 5.22 – Power flows distribution.

5.10 Scenario 2

The load current perturbation signal is depicted in Figure 5.23. The first disturbance, which ranges from 0.8A to 5.3A, is applied at 9 seconds. After about 100 seconds, another disturbance is imposed, where the current is dropped back from 5.3A to 0.8A.

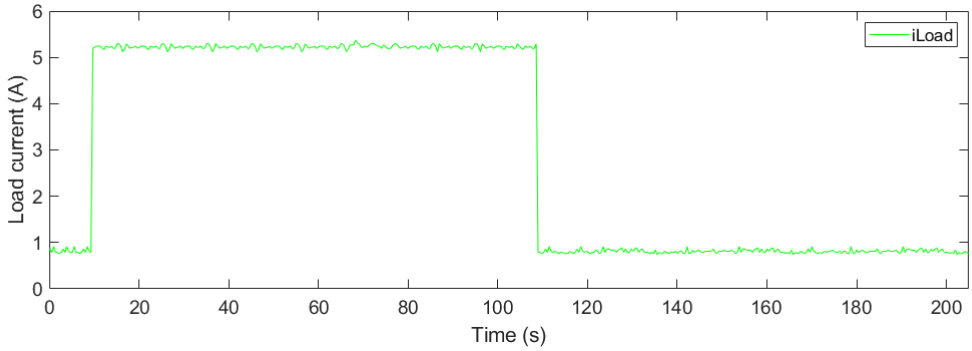

Figure 5.23 – Load current perturbation signal.

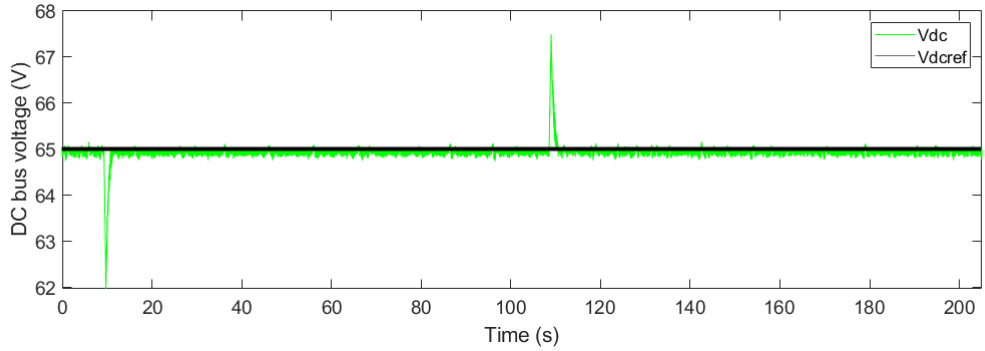

Figure 5.24 – DC bus voltage.

It is clear from the Figure 5.24 that the DC bus voltage controller is able to follow the changes in the load current with good tracking performance. The maximum tracking error in overshoots and undershoots is around 3V, which corresponds to a percentage error of approximately 4%. This level of error is considered acceptable for this type of system as it falls within the acceptable range (0-10%) for DC bus voltage controllers. This is due to the fact that the DC bus voltage controller is able to maintain the voltage within a certain range, ensuring the stability and reliability of the system. Additionally, the good tracking performance can be attributed to the controller's ability to quickly respond to changes in the load current.

Figures 5.25, 5.26 and 5.27 illustrate the current references of each of the emulated fuel cell, the battery and the supercapacitor respectively. It can be observed that the local controllers of each of the energy sources demonstrate excellent tracking performance. The emulated fuel cell exhibits the lowest frequency signal, the battery responds to moderately more frequent current variations, and the supercapacitor effectively manages peak current

demands during transient moments.

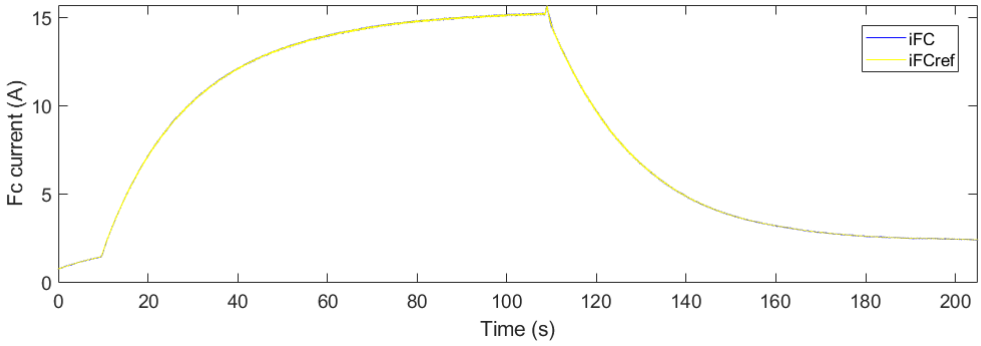

Figure 5.25 – emulated fuel cell current variations.

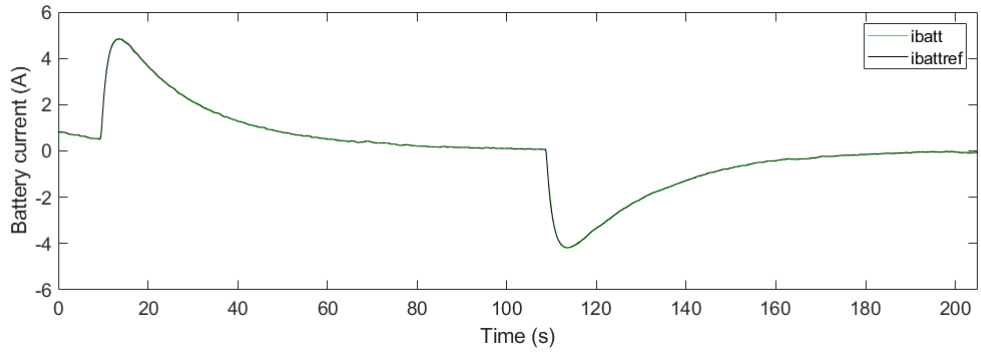

Figure 5.26 – Battery current variations.

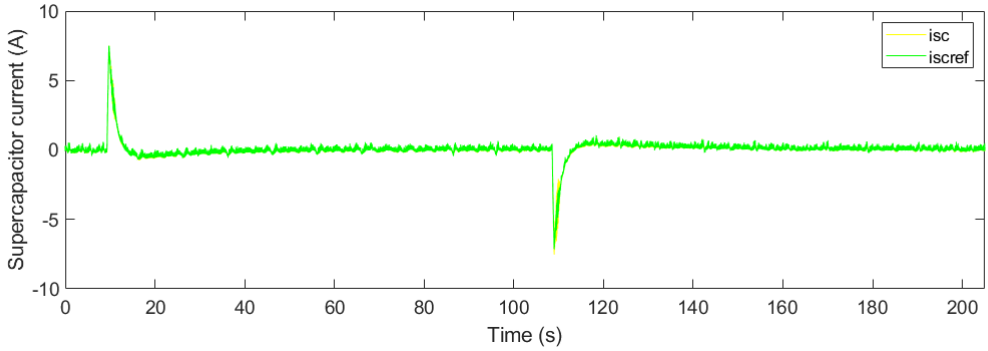

Figure 5.27 – Supercapacitor current variations.

The duty cycles generated by these controllers to drive the respective converters are represented in Figure 5.28. These cyclic ratios, with a difference in scale, reflect the behaviour of the currents provided by the various energy sources.

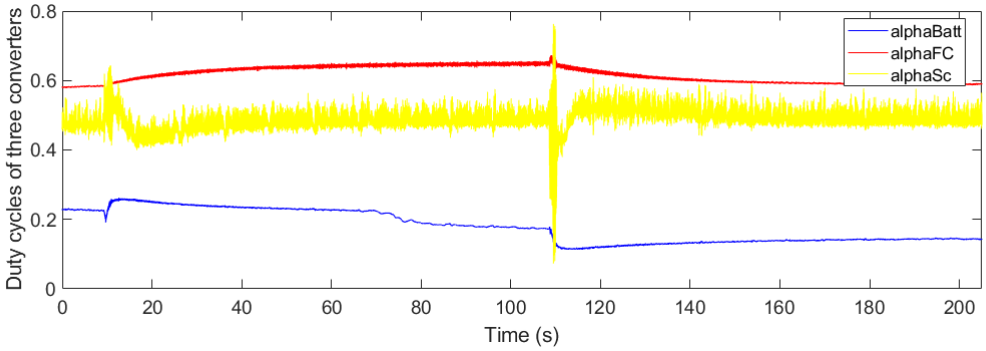

Figure 5.28 – Duty cycles of the power converters.

In the context of real-time applications, it is important to acknowledge that the SMC technique in general may not always be the most ideal option due to the inherent chattering effect that is commonly associated with it. In practical scenarios where switching in converters is real and high-frequency noises can potentially be generated from any other equipment, the chattering effect can be detrimental to system performance. However, the results of the experiments conducted on the proposed model-free Super-Twisting SMC have shown promising results in mitigating this issue and also enhancing the performance of the system. This is done by generating smooth control signals that are responsible for the consistent smoothness observed in all other current and voltage signals.

5.11 Conclusion

Hardware-in-the-loop (HIL) simulation is a valuable tool for developing and testing complex control systems. It offers a realistic testing environment by incorporating real-world hardware components and is a cost-effective alternative to field testing. HIL simulation also reduces development time by allowing for early testing of the control system. In this final chapter, a description of an experimental test bench is constructed using a dSPACE system is described, The electric architecture used in the experiments comprised three energy sources: an emulated fuel cell, battery, and supercapacitor. Two control scenarios were carried out on the bench in order to test the performance of the MFSMC structure at both lower and higher levels of control.

Based on the experimental evidence provided, the MFSMC has been shown to be highly effective in terms of ease of implementation and performance, while also effectively addressing the problem of sliding mode chattering, resulting in a more stable and accurate

control system.

The effectiveness of the proposed control structure is further enhanced by the implementation of an Energy Management System (EMS), which allows for an appropriate distribution of the power demand between the sources. The combination of the MFSMC and the Energy Management System allows for the creation of a control structure that is highly robust and effective, making it a promising solution for various applications, including residential systems.

General Conclusion

The energy transition revolution has prompted a growing interest in renewable energy sources such as solar, wind, geothermal and hydrogen power. Microgrids have emerged as a promising solution for integrating these sources into the power grid in a controlled and efficient manner. A microgrid is a small-scale power grid that can operate independently or in conjunction with the main power grid. It typically consists of a collection of distributed energy resources such as solar panels, wind turbines, batteries, and generators, as well as the necessary control and communication systems to manage and optimize their operation. Once the DERs and microgrid architecture and topology have been selected and designed, the control structure becomes a crucial task. The control structure is responsible for managing and directing the DERs and energy storage units, as well as ensuring that the microgrid operates in a stable and reliable manner. The choice of control structure can have a significant impact on the performance and efficiency of the microgrid, as well as its ability to respond to changes in energy demand and supply.

In this thesis work, the focus is on two key areas of control, i.e. global control and energy management of DC MGs. Global control involves the control of the DC bus voltage by controlling the individual DERs and energy storage units within the microgrid. Effective global control is essential for maintaining the stability and reliability of the microgrid, as well as ensuring that the DERs operate within their specified limits and parameters. Energy management, on the other hand, concerns the coordination and management of energy flow between the DERs in the microgrid. This involves optimizing the use of available energy sources and storage units to meet energy demand, while also ensuring that the microgrid remains stable and reliable. Effective energy management requires a combination of advanced control algorithms, forecasting techniques, and real-time monitoring and communication systems.

The thesis begins with a comprehensive review of literature on MicroGrid technology, aimed at gaining a solid understanding of their topologies and the various forms of Distributed Generation that can be incorporated. Additionally, the literature review introduces multiple existing control structures for MicroGrids.

Chapter 2 of the thesis focuses on examining the mathematical model of a MicroGrid

consisting of renewable source, green source, load, and storage systems. The analysis employs two modelling technique for the converters, the first on is the modeling by the electrical components, the second one is the averaging model for energy management system simulation purpose. time-averaged modeling technique, which is the commonly used approach in power converter applications.

The microgrid under study is a four units system. It is composed of the PV panel system as the main energy source, the fuel cell as an auxiliary energy source and a hybrid energy storage system composed of two complementary units the battery and the supercapacitor. The different physical characteristics of the storage components ensure power generation and load demand balance in variable power and energy time frames. In addition, two boost converters are employed for the PV panel system and the fuel cell while two bidirectional converters are used for the energy storage units.

In Chapter 3, we present a detailed account of the control structure designed for the microgrid, in order to ensure stability, reliability and resilience. The structure is hierarchical, consisting of two levels of control, with the energy management system serving as the main managing element between these two levels. The higher level is responsible for DC bus voltage control, while the lower level is represented by local controllers for the different units in the microgrid (four controllers, each one corresponding to a converter). These local controllers must track the references generated by the high-level controllers. To achieve the desired control, we propose the use of a model-free Supertwisting sliding mode control equipped with an anti-windup technique for both types of controllers (low and high). We conduct three case studies, taking into account multiple scenarios to evaluate the performance of this control structure. The first case study evaluates the system's response under irradiance and load changes. The second case study evaluates the controlled system under control input disturbance and parameter variations and compares the performance of the system to the conventional model-based sliding mode control. In the third case study, we evaluate the system's sensitivity to sensor noise and compare its performance to that of the feedback linearization control technique. The simulations results provide compelling evidence of the reliability and effectiveness of the proposed control structure.The robustness of the adopted control action is validated during both transient and steady-state operation modes. One of the main advantages of the structure is that it is not dependent on the model, allowing it to treat the system like a black box. As a result, it is highly adaptable to changes in the system parameters. making it robust and less sensitive to sensor noise. This means that any parameter variations that

may occur during the operation of the microgrid can be easily handled by the control structure, without any loss of performance. The anti-windup feature helped the controller maintaining the control input within their predefined limits.

Chapter 4 focuses on the proposed energy management strategy, the Gain-Scheduled Filtering Technique. The chapter begins by recalling the frequency-decoupling technique, as the proposed technique is an adaptive version of it. The proposed EMS not only aims to share power or current between MG units, but also aims to regulate the state of charge (SoC) of the battery by adjusting the filter gain online. The key principle of the strategy is that, based on the battery's state of charge, the EMS selects the appropriate gain to either charge or discharge the battery. An optimization problem is built and solved using data collected from system simulations over a one-year period, considering both battery usage and hydrogen consumption. The most suitable gains are then generated from a set of candidate gains and implemented into the EMS structure. Simulations were conducted to test the performance of the EMS technique. The results confirm the effectiveness of the proposed EMS strategy, as it ensures continuous system supply while managing the battery SoC. A comparison to two other candidate EMS strategies used in literature was performed. The results demonstrate that the Gain-Scheduled Filtering Technique offers superior performance, as it can save much more hydrogen consumption than the two other strategies while causing only a minor increase in battery usage. This means that implementing the Gain-Scheduled Filtering Technique can lead to a more efficient and sustainable energy management system, with reduced hydrogen consumption and potential cost savings in the long term.

Besides the simulation, Hardware-in-the-loop (HIL) tests were conducted in the IREENA Lab on a test bench in order to evaluate the performance of the developped control structure. The results of the tests in Chapter 5 corroborate with the theoretical analysis and demonstrated that the proposed controller structure with the implemented model-free supertwisting sliding mode control technique performed well and could handle high perturbations while minimizing chattering. This real-time implementation on a test bench confirms the applicability of the proposed control philosophy for operating DC MicroGrids with high reliability and performance.

5.12 Perspectives

Regarding the future, there are several potential areas of growth and innovation. Some perspectives that can be envisaged are:

— Expanding the EMS approach to include the second filter into the optimization problem. Thereby, redefining the cost function to take into account parameters such as supercapacitor aging as well as the fuel cell degradation in the optimization problem.

— Aiming for the real-time operation of the EMS approach by incorporating online load profile prediction and weather forecasting.

— Developing a continuous variable gain instead of the actual discrete one, where a curve of optimal gains vs SoC can be derived, and as expectation, this should give more accurate and precise way for scheduling rather than the hysteresis concept.

— To get as close as possible to the optimal gain values, it would be beneficial to increase the number of potential gain values being considered.

— Including an electrolyzer in the architecture: Evaluate the integration feasibility and develop a model for the electrolyzer within the control and EMS framework.

— Evaluate the adaptability of the developed algorithms for handling more complex MG configurations (like radial or meshed MG) by analyzing their characteristics and constraints.

APPENDIX

Appendix 1

	Parameters	Description	Simulation value	Units
DC bus	V_{dc}	DC bus voltage	48	V
	C_{dc}	DC bus capacitance	0.001	F
PV	V_{oc}	Open circuit voltage	36.3	V/module
	I_{sc}	Short circuit current	7.84	A/module
	N_{cell}	Number of cell	60	cell/module
	R_{sh}	Shunt resistance	313.0553	$\Omega/module$
	R_{se}	Series resistance	0.39381	$\Omega/module$
	P_{max}	Maximum power	213.5	W/module
	N_p	Number of parallel	5	module
	N_s	Number of series	1	module
	L_{PV}	PV converter inductance	0.0001	H
Batt	E_{Batt}	Open circuit voltage	28	V
	R_{Batt}	Ohmic resistance	0.001	Ω
	$R_{p_{Batt}}$	Polarization resistance	0.0008	Ω
	$C_{p_{Batt}}$	Polarization capacitance	$7X10^4$	F
	L_{Batt}	Batt converter inductance	0.0001	H
Sc	C_{sc}	Sc capacitance	165	F
	R_s	Series resistance	0.0014	Ω
	R_p	Parallel resistance	$9.6x10^2$	Ω
	L_{sc}	Sc converter inductance	0.0001	H
Filter frequency	$F_{c_{FC}}$	Cutting frequency LPF1	0.1	Hz
	$F_{c_{Batt}}$	Cutting frequency LPF2	0.001	Hz

Appendix 2

	Parameters	Description	Simulation value	Units
DC bus	V_{dc}	DC bus voltage	48	V
	C_{dc}	DC bus capacitance	1.00E-03	F
PV	V_{oc}	Open circuit voltage	43.5	V/module
	I_{sc}	Short circuit current	5.25	A/module
	N_{cell}	Number of cell	72	cell/module
	R_{sh}	Shunt resistance	125.0069	$\Omega/module$
	R_{se}	Series resistance	0.62818	$\Omega/module$
	P_{max}	Maximum power	164.85	W/module
	N_p	Number of parallel	2	module
	N_s	Number of series	1	module
FC	P_{max}	Maximal power	2.80E+02	W
	E_{FC}	Open circuit voltage	2.80E+01	V
	R_{con}	Concentration resistance	5.00E-03	Ω
	R_{act}	Activation resistance	1.00E-02	Ω
	R_{Ω}	Ohmic resistance	1.30E-02	Ω
	C_{dl}	Double-layer equivalent capacitor	1.00E-06	F
	$I_{FC_{max}}$	Maximal FC current	1.00E+01	A
	N_s	Number of series cell	28	cell
Batt	E_{Batt}	Open circuit voltage	24	V
	R_{Batt}	Ohmic resistance	0.013	Ω
	R_{pBatt}	Polarization resistance	0.0008	Ω
	C_{pBatt}	Polarization capacitance	8x10^4	F
	Q_{Batt}	Battery capacitance	150	Ah
Sc	C_{sc}	Sc capacitance	100	F
	E_{sc}	Sc initial voltage	24	V
	R_s	Series resistance	0.0014	Ω
	R_p	Parallel resistance	9.6x10^2	Ω
Filtering frequency	$f_{c_{FC}}$	Cutting frequency LPF1	0.1	Hz
	$f_{c_{Batt}}$	Cutting frequency LPF2	0.001	Hz

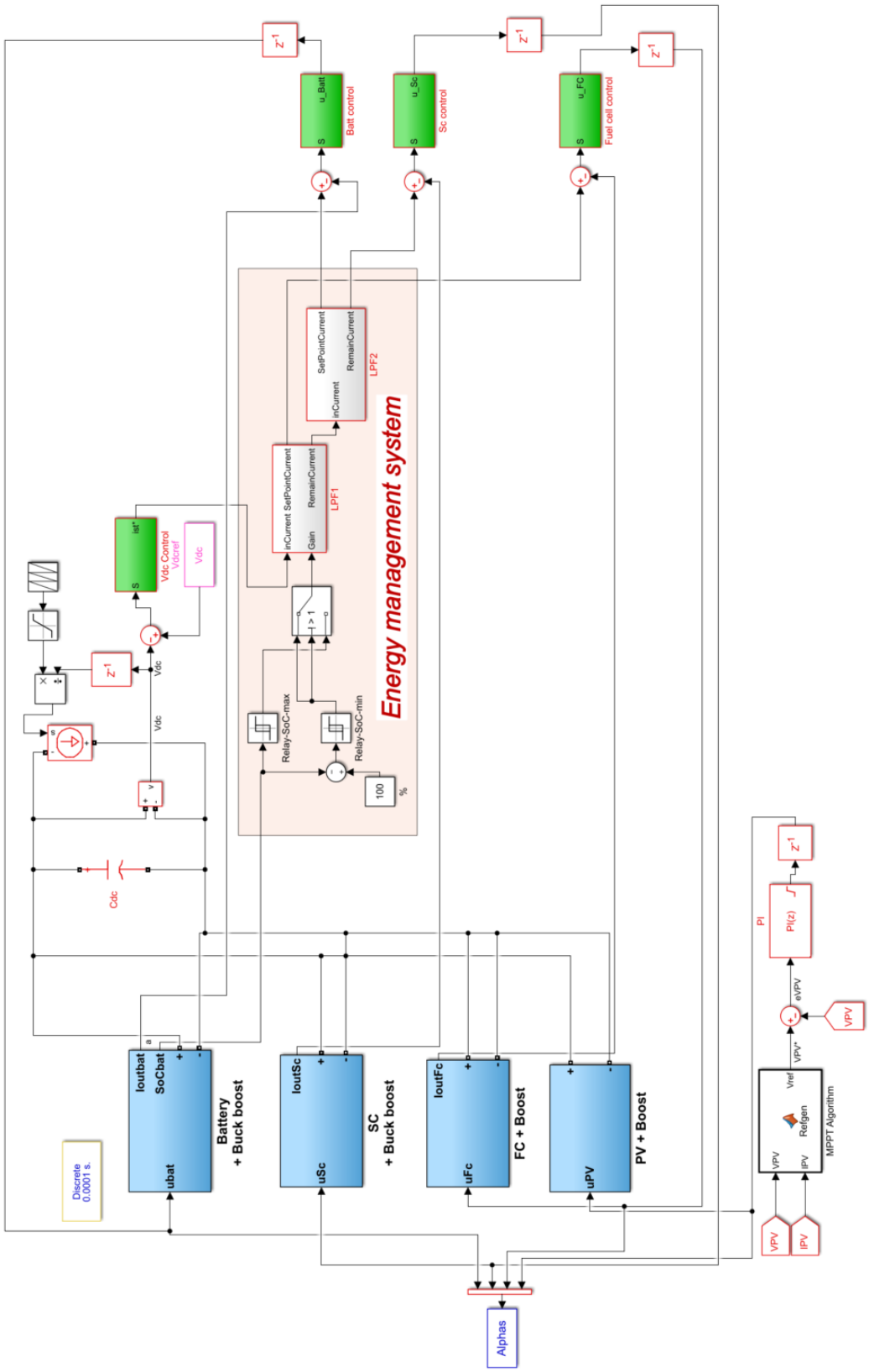

Figure 5.29 – Overview of EMS inside the electrical system made on Simulink.

References

[1] IEA. « For the first time in decades, the number of people without access to electricity is set to increase in 2022 », International Energy Agency (IEA). (2022), [Online]. Available: https://www.iea.org/commentaries/for-the-first-time-in-decades-the-number-of-people-without-access-to-electricity-is-set-to-increase-in-2022 (visited on 04/16/2023).

[2] *Développement durable description — legrandgroup.com*, https://www.legrandgroup.com/fr/developpement-durable-description, [Accessed 14-May-2023].

[3] French Ministry of Ecological Transition, *Compensation of greenhouse gas emissions related to domestic flights*, Website, Accessed in 2023. [Online]. Available: https://www.ecologie.gouv.fr/en/compensation-greenhouse-gas-emissions-related-domestic-flights.

[4] S. Manes and M. M. Vale, « Achieving the paris agreement would substantially reduce climate change risks to biodiversity in central and south america », *Regional Environmental Change*, vol. 22, *2*, p. 60, 2022.

[5] T. Capurso, M. Stefanizzi, M. Torresi, and S. Camporeale, « Perspective of the role of hydrogen in the 21st century energy transition », *Energy Conversion and Management*, vol. 251, p. 114 898, 2022.

[6] T. Gaudiaut, *Infographie: les énergies renouvelables ont dépassé les énergies fossiles en europe*. [Online]. Available: https://fr.statista.com/infographie/24079/part-energies-renouvelables-fossiles-nucleaire-dans-le-mix-energique-en-europe-ue/.

[7] *Renewable power remains cost-competitive amid fossil fuel crisis*, Jul. 2022. [Online]. Available: https://www.irena.org/news/pressreleases/2022/Jul/Renewable-Power-Remains-Cost-Competitive-amid-Fossil-Fuel-Crisis.

[8] M. Shafiullah, A. M. Refat, M. E. Haque, *et al.*, « Review of recent developments in microgrid energy management strategies », *Sustainability*, vol. 14, *22*, p. 14 794, 2022.

[9] *The differences between ac microgrids and dc microgrids*, Jan. 2023. [Online]. Available: `https://www.veckta.com/2021/05/27/the-differences-between-ac-microgrids-and-dc-microgrids/`.

[10] H. Li, Z. Ren, A. Trivedi, P. P. Verma, D. Srinivasan, and W. Li, « A noncooperative game-based approach for microgrid planning considering existing interconnected and clustered microgrids on an island », *IEEE Transactions on Sustainable Energy*, vol. 13, *4*, pp. 2064–2078, 2022.

[11] Q. T. Tran, K. Davies, and S. Sepasi, « Isolation microgrid design for remote areas with the integration of renewable energy: a case study of con dao island in vietnam », *Clean Technologies*, vol. 3, *4*, pp. 804–820, 2021.

[12] E. Konečná, S. Y. Teng, and V. Máša, « New insights into the potential of the gas microturbine in microgrids and industrial applications », *Renewable and Sustainable Energy Reviews*, vol. 134, p. 110 078, 2020.

[13] S. Ferahtia, A. Djeroui, H. Rezk, A. Houari, S. Zeghlache, and M. Machmoum, « Optimal control and implementation of energy management strategy for a dc microgrid », *Energy*, vol. 238, p. 121 777, 2022.

[14] M. Hu, F. Xiao, and S. Wang, « Neighborhood-level coordination and negotiation techniques for managing demand-side flexibility in residential microgrids », *Renewable and Sustainable Energy Reviews*, vol. 135, p. 110 248, 2021.

[15] K. T. Akindeji, R. Tiako, and I. E. Davidson, « Use of renewable energy sources in university campus microgrid–a review », *in 2019 International Conference on the Domestic Use of Energy (DUE)*, IEEE, 2019, pp. 76–83.

[16] D. Zhang and J. Wang, « Adaptive sliding-mode control in bus voltage for an islanded dc microgrid », *Mathematical Problems in Engineering*, vol. 2017, 2017.

[17] S. Carley and D. M. Konisky, « The justice and equity implications of the clean energy transition », *Nature Energy*, vol. 5, *8*, pp. 569–577, 2020.

[18] I. Abdallah, « Event-driven hybrid bond graph: application: hybrid renewable energy system for hydrogen production and storage », Ph.D. dissertation, Université de Lille, 2017.

[19] M. Cucuzzella, R. Lazzari, S. Trip, S. Rosti, C. Sandroni, and A. Ferrara, « Sliding mode voltage control of boost converters in dc microgrids », *Control Engineering Practice*, vol. 73, pp. 161–170, 2018.

[20] J. Lian, Y. Zhang, C. Ma, Y. Yang, and E. Chaima, « A review on recent sizing methodologies of hybrid renewable energy systems », *Energy Conversion and Management*, vol. 199, p. 112 027, 2019.

[21] R. Saidi, J. C. Olivier, M. Machmoum, and E. Chauveau, « Cascaded centered moving average filters for energy management in multisource power systems with a large number of devices », *Energies*, vol. 14, *12*, p. 3627, 2021.

[22] J. Marqusee, W. Becker, and S. Ericson, « Resilience and economics of microgrids with pv, battery storage, and networked diesel generators », *Advances in Applied Energy*, vol. 3, p. 100 049, 2021.

[23] M. F. Ishraque, S. A. Shezan, J. N. Nur, and M. S. Islam, « Optimal sizing and assessment of an islanded photovoltaic-battery-diesel generator microgrid applicable to a remote school of bangladesh », *Engineering Reports*, vol. 3, *1*, e12281, 2021.

[24] Y. Liu, Y. Hu, Y. Wang, *et al.*, « A novel adaptive model predictive control for proton exchange membrane fuel cell in dc microgrids », *IEEE Transactions on Smart Grid*, 2022.

[25] J. J. Lamb and B. Austbø, « Current use of bioenergy and hydrogen », *in Hydrogen, Biomass and Bioenergy*, Elsevier, 2020, pp. 9–20.

[26] M. Zaibi, G. Champenois, X. Roboam, J. Belhadj, and B. Sareni, « Smart power management of a hybrid photovoltaic/wind stand-alone system coupling battery storage and hydraulic network », *Mathematics and Computers in Simulation*, vol. 146, pp. 210–228, 2018.

[27] L. Kouchachvili, W. Yaıci, and E. Entchev, « Hybrid battery/supercapacitor energy storage system for the electric vehicles », *Journal of Power Sources*, vol. 374, pp. 237–248, 2018.

[28] A. G. S. Al-Salloomee, S. Khosroabadi, and A. A. A. Albukariat, « Study of power management of standalone dc microgrids with battery supercapacitor hybrid energy storage system », *International Journal of Electrical and Computer Engineering*, vol. 12, *1*, p. 114, 2022.

[29] S. B. Siad, A. Iovine, G. Damm, L. Galai-Dol, and M. Netto, « Nonlinear hierarchical easy-to-implement control for dc microgrids », *Energies*, vol. 15, *3*, p. 969, 2022.

[30] A. A. Kamel, H. Rezk, N. Shehata, and J. Thomas, « Energy management of a dc microgrid composed of photovoltaic/fuel cell/battery/supercapacitor systems », *Batteries*, vol. 5, *3*, p. 63, 2019.

[31] J. Castro-Gutiérrez, A. Celzard, and V. Fierro, « Energy storage in supercapacitors: focus on tannin-derived carbon electrodes », *Frontiers in materials*, vol. 7, p. 217, 2020.

[32] M. Quashie, F. Bouffard, and G. Joós, « Business cases for isolated and grid connected microgrids: methodology and applications », *Applied Energy*, vol. 205, pp. 105–115, 2017.

[33] R. Logesh *et al.*, « Resources, configurations, and soft computing techniques for power management and control of pv/wind hybrid system », *Renewable and Sustainable Energy Reviews*, vol. 69, pp. 129–143, 2017.

[34] S. M. Mohiuddin and J. Qi, « Optimal distributed control of ac microgrids with coordinated voltage regulation and reactive power sharing », *IEEE Transactions on Smart Grid*, vol. 13, *3*, pp. 1789–1800, 2022.

[35] L. Zhang, H. Peng, Z. Ning, Z. Mu, and C. Sun, « Comparative research on rc equivalent circuit models for lithium-ion batteries of electric vehicles », *Applied Sciences*, vol. 7, *10*, p. 1002, 2017.

[36] K. Jithin, P. Haridev, N. Mayadevi, R. H. Kumar, and V. Mini, « A review on challenges in dc microgrid planning and implementation », *Journal of Modern Power Systems and Clean Energy*, 2022.

[37] V. F. Pires, A. Pires, and A. Cordeiro, « Dc microgrids: benefits, architectures, perspectives and challenges », *Energies*, vol. 16, *3*, p. 1217, 2023.

[38] M. Fotopoulou, D. Rakopoulos, D. Trigkas, F. Stergiopoulos, O. Blanas, and S. Voutetakis, « State of the art of low and medium voltage direct current (dc) microgrids », *Energies*, vol. 14, *18*, p. 5595, 2021.

[39] T. Dragičević, X. Lu, J. C. Vasquez, and J. M. Guerrero, « Dc microgrids—part ii: a review of power architectures, applications, and standardization issues », *IEEE Transactions on Power Electronics*, vol. 31, *5*, pp. 3528–3549, 2016. DOI: 10.1109/TPEL.2015.2464277.

[40] P. Singh and J. S. Lather, « Power management and control of a grid-independent dc microgrid with hybrid energy storage system », *Sustainable Energy Technologies and Assessments*, vol. 43, p. 100 924, 2021.

[41] Z. Alhadrawi, M. N. Abdullah, and H. Mokhlis, « Review of microgrid protection strategies: current status and future prospects », *TELKOMNIKA (Telecommunication Computing Electronics and Control)*, vol. 20, *1*, pp. 173–184, 2022.

[42] G. S. Rawat and Sathans, « Survey on dc microgrid architecture, power quality issues and control strategies », *in 2018 2nd International Conference on Inventive Systems and Control (ICISC)*, 2018, pp. 500–505. DOI: 10.1109/ICISC.2018.8399123.

[43] R. Asad and A. Kazemi, « A novel distributed optimal power sharing method for radial dc microgrids with different distributed energy sources », *Energy*, vol. 72, pp. 291–299, 2014.

[44] R. Mohanty and A. K. Pradhan, « Protection of smart dc microgrid with ring configuration using parameter estimation approach », *IEEE Transactions on Smart Grid*, vol. 9, *6*, pp. 6328–6337, 2018. DOI: 10.1109/TSG.2017.2708743.

[45] S. A. Wakode, A. A. Sheikh, R. R. Deshmukh, and M. S. Ballal, « Oscillation frequency based protection scheme for ring type dc microgrid », *in 2020 IEEE International Conference on Power Electronics, Smart Grid and Renewable Energy (PESGRE2020)*, 2020, pp. 1–5. DOI: 10.1109/PESGRE45664.2020.9070592.

[46] R. D. Silveira, S. A. O. da Silva, and L. P. Sampaio, « Dynamic modeling and stability analysis of radial and ring dc microgrid topologies », *in 2021 Brazilian Power Electronics Conference (COBEP)*, 2021, pp. 1–8. DOI: 10.1109/COBEP53665.2021.9684036.

[47] A. M. Sallam, H. M. Ahmed, and M. Salama, « A planning framework for ac-dc bilayer microgrids », *Electric Power Systems Research*, vol. 188, p. 106 524, 2020.

[48] G.-Y. Lee, B.-S. Ko, J.-S. Lee, and R.-Y. Kim, « An off-line design methodology of droop control for multiple bi-directional distributed energy resources based on voltage sensitivity analysis in dc microgrids », *International Journal of Electrical Power & Energy Systems*, vol. 118, p. 105 754, 2020.

[49] X. Feng, K. L. Butler-Purry, and T. Zourntos, « Real-time electric load management for dc zonal all-electric ship power systems », *Electric Power Systems Research*, vol. 154, pp. 503–514, 2018.

[50] J. Ciezki and R. Ashton, « Selection and stability issues associated with a navy shipboard dc zonal electric distribution system », *IEEE Transactions on Power Delivery*, vol. 15, *2*, pp. 665–669, 2000. DOI: 10.1109/61.853002.

[51] C. Liu, S. Zhang, X. Chen, W. Xu, and K. Wang, « A comprehensive study of the potential and applicability of photovoltaic systems for zero carbon buildings in hainan province, china », *Solar Energy*, vol. 238, pp. 371–380, 2022.

[52] A. LaPotin, K. L. Schulte, M. A. Steiner, *et al.*, « Thermophotovoltaic efficiency of 40% », *Nature*, vol. 604, *7905*, pp. 287–291, 2022.

[53] M. Mohammadinodoushan, R. Abbassi, H. Jerbi, F. W. Ahmed, A. Rezvani, *et al.*, « A new mppt design using variable step size perturb and observe method for pv system under partially shaded conditions by modified shuffled frog leaping algorithm-smc controller », *Sustainable Energy Technologies and Assessments*, vol. 45, p. 101 056, 2021.

[54] D. Verma, S. Nema, R. Agrawal, Y. Sawle, and A. Kumar, « A different approach for maximum power point tracking (mppt) using impedance matching through non-isolated dc-dc converters in solar photovoltaic systems », *Electronics*, vol. 11, *7*, p. 1053, 2022.

[55] Ö. F. TOZLU and H. ÇALIK, « A review and classification of most used mppt algorithms for photovoltaic systems », *Hittite Journal of Science and Engineering*, vol. 8, *3*, pp. 207–220, 2021.

[56] A. Charaabi, O. Barambones, A. Zaidi, and N. Zanzouri, « A novel two stage controller for a dc-dc boost converter to harvest maximum energy from the pv power generation », *in Actuators*, MDPI, vol. 9, 2020, p. 29.

[57] C. Lupangu, A. Saha, R. C. Bansal, and J. Justo, « Critical performance comparison between single-stage and two-stage incremental conductance mppt algorithms for dc/dc boost-converter applied in pv systems », *Electric Power Components and Systems*, vol. 50, *4-5*, pp. 207–222, 2022.

[58] H. J. Undertaking, « Hydrogen roadmap europe: a sustainable pathway for the european energy transition », 2019.

[59] Z. Lu, H. Zhang, L. Duan, Q. Wang, R. Zhang, and C. Lu, « An experimental study of the effects of key operating parameters on the molten carbonate fuel cell performance », *Sustainable Energy & Fuels*, 2023.

[60] M. Carmo, D. L. Fritz, J. Mergel, and D. Stolten, « A comprehensive review on pem water electrolysis », *International journal of hydrogen energy*, vol. 38, *12*, pp. 4901–4934, 2013.

[61] D. Crawford, *Guide to hydrogen fuel cell*, `https://www.theautochannel.com/news/2015/09/10/141185-guide-to-hydrogen-fuel-cell-by-douglas-crawford.html`, Accessed on May 12, 2023, Sep. 2015.

[62] Unknown, *How will the super duper tesla battery work and more on the price of electricity*, `https://ussromantics.com/2017/07/19/how-will-the-super-duper-tesla-battery-work-and-more-on-the-price-of-electricity/`, Accessed on May 12, 2023, Jul. 2017.

[63] G. L. Soloveichik, « Battery technologies for large-scale stationary energy storage », *Annual review of chemical and biomolecular engineering*, vol. 2, pp. 503–527, 2011.

[64] M. M. Biswas, M. S. Azim, T. K. Saha, U. Zobayer, and M. C. Urmi, « Towards implementation of smart grid: an updated review on electrical energy storage systems », 2013.

[65] M. E. Şahin, F. Blaabjerg, and A. Sangwongwanich, « A comprehensive review on supercapacitor applications and developments », *Energies*, vol. 15, *3*, p. 674, 2022.

[66] S. Zhang and N. Pan, « Supercapacitors performance evaluation », *Advanced Energy Materials*, vol. 5, *6*, p. 1 401 401, 2015.

[67] M. Aslani, *Electrochemical double layer capacitors (supercapacitors)*, Accessed on December 14, 2012, 2012. [Online]. Available: `http://large.stanford.edu/courses/2012/ph240/aslani1/`.

[68] C. Mahjoubi, « Modélisation multi-physique et gestion d'énergie d'un micro-réseau résidentiel », Ph.D. dissertation, Nantes, 2019.

[69] H. Vaikund *et al.*, « Cost mitigation strategy for microgrid using an advanced energy management system with an intelligent controller », *Electric Power Systems Research*, vol. 210, p. 108 116, 2022.

[70] R. Kaluthanthrige and A. D. Rajapakse, « Demand response integrated day-ahead energy management strategy for remote off-grid hybrid renewable energy systems », *International journal of electrical power & energy systems*, vol. 129, p. 106 731, 2021.

[71] A. Hasankhani and S. M. Hakimi, « Stochastic energy management of smart microgrid with intermittent renewable energy resources in electricity market », *Energy*, vol. 219, p. 119 668, 2021.

[72] S. Kassir, M. Doumiati, M. Machmoum, M. El Rafei, and C. Francis, « Robust control and energy management in a hybrid dc microgrid using second-order smc », *in IECON 2022–48th Annual Conference of the IEEE Industrial Electronics Society*, IEEE, 2022, pp. 1–6.

[73] M. Mehdi, C.-H. Kim, and M. Saad, « Robust centralized control for dc islanded microgrid considering communication network delay », *IEEE Access*, vol. 8, pp. 77 765–77 778, 2020. DOI: 10.1109/ACCESS.2020.2989777.

[74] J. Kumar, A. Agarwal, and V. Agarwal, « A review on overall control of dc microgrids », *Journal of energy storage*, vol. 21, pp. 113–138, 2019.

[75] R. A. Ferreira, H. A. Braga, A. A. Ferreira, and P. G. Barbosa, « Analysis of voltage droop control method for dc microgrids with simulink: modelling and simulation », *in 2012 10th IEEE/IAS International Conference on Industry Applications*, IEEE, 2012, pp. 1–6.

[76] X. Huang, K. Wang, J. Qiu, L. Hang, G. Li, and X. Wang, « Decentralized control of multi-parallel grid-forming dgs in islanded microgrids for enhanced transient performance », *IEEE Access*, vol. 7, pp. 17 958–17 968, 2019.

[77] G. Lin, W. Zuo, Y. Li, J. Liu, S. Wang, and P. Wang, « Comparative analysis on the stability mechanism of droop control and vid control in dc microgrid », *Chinese Journal of Electrical Engineering*, vol. 7, *1*, pp. 37–46, 2021.

[78] M. Boukerdja, A. Chouder, and K. Louassaa, « Realizing the accurate power sharing in dc microgrid using droop control strategy. », *in 2019 International Conference on Advanced Electrical Engineering (ICAEE)*, IEEE, 2019, pp. 1–5.

[79] J. Ma and X. Ma, « Distributed control of battery energy storage system in a microgrid », *in 2019 8th International Conference on Renewable Energy Research and Applications (ICRERA)*, IEEE, 2019, pp. 320–325.

[80] C. Li, T. Dragicevic, M. G. Plaza, F. Andrade, J. C. Vasquez, and J. M. Guerrero, « Multiagent based distributed control for state-of-charge balance of distributed energy storage in dc microgrids », *in IECON 2014-40th Annual Conference of the IEEE Industrial Electronics Society*, IEEE, 2014, pp. 2180–2184.

[81] A. Abhishek, A. Ranjan, S. Devassy, B. Kumar Verma, S. K. Ram, and A. K. Dhakar, « Review of hierarchical control strategies for dc microgrid », *IET Renewable Power Generation*, vol. 14, *10*, pp. 1631–1640, 2020.

[82] Z. Shuai, J. Fang, F. Ning, and Z. J. Shen, « Hierarchical structure and bus voltage control of dc microgrid », *Renewable and Sustainable Energy Reviews*, vol. 82, pp. 3670–3682, 2018.

[83] A. Chokor, « Design of several centralized and decentralized multilayer robust control architectures for global chassis control », Ph.D. dissertation, Compiègne, 2019.

[84] I. Alhamrouni, M. Hairullah, N. Omar, M. Salem, A. Jusoh, and T. Sutikno, « Modelling and design of pid controller for voltage control of ac hybrid micro-grid », *International Journal of Power Electronics and Drive Systems*, vol. 10, *1*, p. 151, 2019.

[85] R. K. Chauhan, B. Rajpurohit, R. Hebner, S. N. Singh, and F. Longatt, « Design and analysis of pid and fuzzy-pid controller for voltage control of dc microgrid », *in 2015 IEEE Innovative Smart Grid Technologies-Asia (ISGT ASIA)*, IEEE, 2015, pp. 1–6.

[86] S. B. Siad, A. Malkawi, G. Damm, L. Lopes, and L. G. Dol, « Nonlinear control of a dc microgrid for the integration of distributed generation based on different time scales », *International Journal of Electrical Power & Energy Systems*, vol. 111, pp. 93–100, 2019.

[87] M. A. Mahmud, T. K. Roy, S. Saha, M. E. Haque, and H. R. Pota, « Robust nonlinear adaptive feedback linearizing decentralized controller design for islanded dc microgrids », *IEEE transactions on industry applications*, vol. 55, *5*, pp. 5343–5352, 2019.

[88] T. K. Roy and M. A. Mahmud, « Dynamic stability analysis of hybrid islanded dc microgrids using a nonlinear backstepping approach », *IEEE Systems Journal*, vol. 12, *4*, pp. 3120–3130, 2017.

[89] T. Huang, S. Gao, and L. Xie, « A neural lyapunov approach to transient stability assessment of power electronics-interfaced networked microgrids », *IEEE Transactions on Smart Grid*, vol. 13, *1*, pp. 106–118, 2021.

[90] P. Thounthong, P. Mungporn, S. Pierfederici, *et al.*, « Robust hamiltonian energy control based on lyapunov function for four-phase parallel fuel cell boost converter for dc microgrid applications », *IEEE Transactions on Sustainable Energy*, vol. 12, *3*, pp. 1500–1511, 2021.

[91] M. Doumiati, B. Traore, J.-C. Olivier, and C. Morel, « Adaptive power sharing algorithm combined with robust control for a multi-source electric vehicle: experimental validation », *International Review of Electrical Engineering*, vol. 17, *1*, 2022.

[92] B. He, S. Wang, and Y. Liu, « Underactuated robotics: a review », *International Journal of Advanced Robotic Systems*, vol. 16, *4*, p. 1 729 881 419 862 164, 2019.

[93] X. Zhang, B. Wang, D. Gamage, and A. Ukil, « Model predictive control based dynamic power loss prediction for hybrid energy storage system in dc microgrids », *IEEE Transactions on Industrial Electronics*, vol. 69, *8*, pp. 8080–8090, 2021.

[94] J. Hu, Y. Shan, J. M. Guerrero, A. Ioinovici, K. W. Chan, and J. Rodriguez, « Model predictive control of microgrids–an overview », *Renewable and Sustainable Energy Reviews*, vol. 136, p. 110 422, 2021.

[95] C. Bordons, F. Garcia-Torres, and M. A. Ridao, *Model predictive control of microgrids*. Springer, 2020, vol. 358.

[96] J. R. Nelson and N. G. Johnson, « Model predictive control of microgrids for real-time ancillary service market participation », *Applied Energy*, vol. 269, p. 114 963, 2020.

[97] P. S. Prasad, A. M. Parimi, and L. Renuka, « Control of hybrid ac/dc microgrids », *in Microgrids*, Elsevier, 2022, pp. 191–225.

[98] N. Ebrahimi, S. Ozgoli, and A. Ramezani, « Model-free sliding mode control, theory and application », *Proceedings of the Institution of Mechanical Engineers, Part I: Journal of Systems and Control Engineering*, vol. 232, *10*, pp. 1292–1301, 2018.

[99] J. Han, J. Wang, J. Xiao, Z. Chen, and B. Wen, « Super twisting sliding mode control with compensated current controller dynamics on active magnetic bearings with large air gap », *IEEE Transactions on Industrial Electronics*, vol. 65, *4*, pp. 3206–3215, 2018.

[100] A. Saleh-Ahmadi, M. Moattari, A. Gahedi, and E. Pouresmaeil, « Droop method development for microgrids control considering higher order sliding mode control approach and feeder impedance variation », *Applied Sciences*, vol. 11, *3*, p. 967, 2021.

[101] Z. Wang, S. Li, and Q. Li, « Continuous nonsingular terminal sliding mode control of dc–dc boost converters subject to time-varying disturbances », *IEEE Transactions on Circuits and Systems II: Express Briefs*, vol. 67, *11*, pp. 2552–2556, 2019.

[102] M. T. Rizi and H. Eliasi, « Nonsingular terminal sliding mode controller for voltage and current control of an islanded microgrid », *Electric Power Systems Research*, vol. 185, p. 106 354, 2020.

[103] L. Setyawan, W. Peng, and X. Jianfang, « Implementation of sliding mode control in dc microgrids », *in 2014 9th IEEE Conference on Industrial Electronics and Applications*, IEEE, 2014, pp. 578–583.

[104] Y. Pimpale and B. Parvat, « Design of sliding mode control for nonlinear uncertain system », *Int. J. Adv. Res. Innov. Ideas Educ*, vol. 4, *5*, pp. 331–336, 2018.

[105] H. Saied, A. Chemori, M. El Rafei, and C. Francis, « A novel model-based robust super-twisting sliding mode control of pkms: design and real-time experiments », *in 2021 IEEE/RSJ International Conference on Intelligent Robots and Systems (IROS)*, IEEE, 2021, pp. 8029–8035.

[106] C. Zheng, T. Dragičević, J. Zhang, R. Chen, and F. Blaabjerg, « Composite robust quasi-sliding mode control of dc–dc buck converter with constant power loads », *IEEE Journal of Emerging and Selected Topics in Power Electronics*, vol. 9, *2*, pp. 1455–1464, 2020.

[107] N. Ullah, A. Ibeas, A. J. Babqi, H. I. Alkhammash, and A. Usman, « Super-twisting sliding mode control of dc microgrids involving renewable sources and storage devices », *CONTROL ENGINEERING AND APPLIED INFORMATICS*, vol. 24, *3*, pp. 64–75, 2022.

[108] M. Dai, R. Qi, and X. Cheng, « Super-twisting sliding mode control design for electric dynamic load simulator », *in 2019 Chinese Control Conference (CCC)*, IEEE, 2019, pp. 3078–3083.

[109] K. Zeb, T. D. C. Busarello, S. Ul Islam, *et al.*, « Design of super twisting sliding mode controller for a three-phase grid-connected photovoltaic system under normal and abnormal conditions », *Energies*, vol. 13, *15*, p. 3773, 2020.

[110] A. K. Pati and N. Sahoo, « Adaptive super-twisting sliding mode control for a three-phase single-stage grid-connected differential boost inverter based photovoltaic system », *ISA transactions*, vol. 69, pp. 296–306, 2017.

[111] Y. M. Alharbi, A. A. Al Alahmadi, N. Ullah, H. Abeida, M. S. Soliman, and Y. S. H. Khraisat, « Super twisting fractional order energy management control for a smart university system integrated dc micro-grid », *IEEE Access*, vol. 8, pp. 128 692–128 704, 2020.

[112] I. Sami, S. Ullah, Z. Ali, N. Ullah, and J.-S. Ro, « A super twisting fractional order terminal sliding mode control for dfig-based wind energy conversion system », *Energies*, vol. 13, *9*, p. 2158, 2020.

[113] I. Sami, S. Ullah, N. Ullah, and J.-S. Ro, « Sensorless fractional order composite sliding mode control design for wind generation system », *ISA transactions*, vol. 111, pp. 275–289, 2021.

[114] S. Emelyanov, S. Korovin, and A. Levant, « High-order sliding modes in control systems », *Computational Mathematics and Modeling*, vol. 7, *3*, pp. 294–318, 1996.

[115] A. Levant, « Universal single-input-single-output (siso) sliding-mode controllers with finite-time convergence », *IEEE Transactions on Automatic Control*, vol. 46, *9*, pp. 1447–1451, 2001.

[116] J. A. Moreno, « On strict lyapunov functions for some non-homogeneous super-twisting algorithms », *Journal of the Franklin Institute*, vol. 351, *4*, pp. 1902–1919, 2014.

[117] Z. Feng and J. Fei, « Design and analysis of adaptive super-twisting sliding mode control for a microgyroscope », *PloS one*, vol. 13, *1*, e0189457, 2018.

[118] R. Svečko, D. Gleich, and A. Sarjaš, « The effective chattering suppression technique with adaptive super-twisted sliding mode controller based on the quasi-barrier function; an experimentation setup », *Applied Sciences*, vol. 10, *2*, p. 595, 2020.

[119] Y. Li and F. Nejabatkhah, « Overview of control, integration and energy management of microgrids », *Journal of Modern Power Systems and Clean Energy*, vol. 2, *3*, pp. 212–222, 2014.

[120] S. Ali, Z. Zheng, M. Aillerie, J.-P. Sawicki, M.-C. Pera, and D. Hissel, « A review of dc microgrid energy management systems dedicated to residential applications », *Energies*, vol. 14, *14*, p. 4308, 2021.

[121] A. Florescu, S. Bacha, I. Munteanu, A. I. Bratcu, and A. Rumeau, « Adaptive frequency-separation-based energy management system for electric vehicles », *Journal of Power Sources*, vol. 280, pp. 410–421, 2015.

[122] T. Mesbahi, « Influence des stratégies de gestion d'une source hybride de véhicule électrique sur son dimensionnement et sa durée de vie par intégration d'un modèle multi-physique », Ph.D. dissertation, Ecole centrale de Lille, 2016.

[123] B. Traoré, M. Doumiati, C. Morel, J.-C. Olivier, and O. Soumaoro, « Energy management strategy design based on frequency separation, fuzzy logic and lyapunov control for multi-sources electric vehicles », *in IECON 2019-45th Annual Conference of the IEEE Industrial Electronics Society*, IEEE, vol. 1, 2019, pp. 2676–2681.

[124] F. Vitale, N. Rispoli, M. Sorrentino, M. Rosen, and C. Pianese, « On the use of dynamic programming for optimal energy management of grid-connected reversible solid oxide cell-based renewable microgrids », *Energy*, vol. 225, p. 120 304, 2021.

[125] R. Abdelhedi, A. Lahyani, A. C. Ammari, A. Sari, and P. Venet, « Reinforcement learning-based power sharing between batteries and supercapacitors in electric vehicles », *in 2018 IEEE International Conference on Industrial Technology (ICIT)*, IEEE, 2018, pp. 2072–2077.

[126] R. Abdelhedi, « Optimisation d'un système de stockage hybride de l'énergie électrique avec batterie et supercondensateurs pour véhicule électrique », Ph.D. dissertation, Université de Lyon; Institut National des Sciences Appliquées et de ..., 2018.

[127] M. Mroueh, M. Doumiati, M. Machmoum, and C. Francis, « A real-time evidential time series prediction method applied on residential electrical load forecasting », *Available at SSRN 4052634*,

[128] H. Hou, C. Liu, Q. Wang, *et al.*, « Review of load forecasting based on artificial intelligence methodologies, models, and challenges », *Electric Power Systems Research*, vol. 210, p. 108 067, 2022.

[129] Z.-H. Zhao, « Improved fuzzy logic control-based energy management strategy for hybrid power system of fc/pv/battery/sc on tourist ship », *International Journal of Hydrogen Energy*, vol. 47, *16*, pp. 9719–9734, 2022.

[130] P. Bedi, S. Goyal, A. S. Rajawat, R. N. Shaw, and A. Ghosh, « Application of ai/iot for smart renewable energy management in smart cities », *AI and IoT for Smart City Applications*, pp. 115–138, 2022.

[131] M. Mroueh, S. Kassir, M. Doumiati, C. Francis, and M. Machmoum, « A new time scale based energy management strategy for a hybrid energy storage system in electrical microgrids », *in IECON 2021–47th Annual Conference of the IEEE Industrial Electronics Society*, IEEE, 2021, pp. 1–6.

[132] B. Traoré, M. Doumiati, C. Morel, J.-C. Olivier, and O. Soumaoro, « Energy management strategy based on a new adaptive filtering algorithm for battery-ultracapacitor electric vehicles », *in 2020 15th IEEE Conference on Industrial Electronics and Applications (ICIEA)*, IEEE, 2020, pp. 392–396.

[133] H. Chen, R. Xiong, C. Lin, and W. Shen, « Model predictive control based real-time energy management for a hybrid energy storage system », *CSEE Journal of Power and Energy Systems*, 2020.

[134] M.-H. Laraki, B. Brahmi, C. Z. El-Bayeh, and M. H. Rahman, « Energy management system for a stand-alone wind/diesel/bess/fuel-cell using dynamic programming », *in 2021 18th International Multi-Conference on Systems, Signals & Devices (SSD)*, IEEE, 2021, pp. 1258–1263.

[135] A. L. Bukar, C. W. Tan, L. K. Yiew, R. Ayop, and W.-S. Tan, « A rule-based energy management scheme for long-term optimal capacity planning of grid-independent microgrid optimized by multi-objective grasshopper optimization algorithm », *Energy conversion and management*, vol. 221, p. 113 161, 2020.

[136] P. Garcia, J. P. Torreglosa, L. M. Fernandez, and F. Jurado, « Optimal energy management system for stand-alone wind turbine/photovoltaic/hydrogen/battery hybrid system with supervisory control based on fuzzy logic », *International Journal of Hydrogen Energy*, vol. 38, *33*, pp. 14 146–14 158, 2013.

[137] M. C. Joshi and S. Samanta, « Improved energy management algorithm with time-share-based ultracapacitor charging/discharging for hybrid energy storage system », *IEEE Transactions on Industrial Electronics*, vol. 66, *8*, pp. 6032–6043, 2018.

[138] P. Bajpai and V. Dash, « Hybrid renewable energy systems for power generation in stand-alone applications: a review », *Renewable and Sustainable Energy Reviews*, vol. 16, *5*, pp. 2926–2939, 2012.

[139] M. Rasheed, O. Alabdali, H. H. Hassan, *et al.*, « Parameters extraction of a single-diode model of photovoltaic cell using false position iterative method », *in Journal of Physics: Conference Series*, IOP Publishing, vol. 1879, 2021, p. 032 113.

[140] V. Stornelli, M. Muttillo, T. De Rubeis, and I. Nardi, « A new simplified five-parameter estimation method for single-diode model of photovoltaic panels », *Energies*, vol. 12, *22*, p. 4271, 2019.

[141] S. B. Siad, « Dc microgrids control for renewable energy integration », Ph.D. dissertation, Université Paris-Saclay; Université d'Evry, 2019.

[142] B. J. Restrepo-Cuestas, M. Durango-Flórez, L. A. Trejos-Grisales, and C. A. Ramos-Paja, « Analysis of electrical models for photovoltaic cells under uniform and partial shading conditions », *Computation*, vol. 10, *7*, p. 111, 2022.

[143] A. Alkhalidi and N. Hussain Al Dulaimi, « Design of an off-grid solar pv system for a rural shelter », *School of Natural Resources Engineering and Management, Department of Energy Engineering Design of an Off-Grid Solar PV system for a rural shelter. Presented by Noor Hussain Al Dulaimi–2008203032 F*, 2018.

[144] A. H. Al-Waeli, H. A. Kazem, M. T. Chaichan, and K. Sopian, *Photovoltaic/thermal (PV/T) systems: principles, design, and applications*. Springer Nature, 2019.

[145] W.-Y. Chang, « Equivalent circuit parameters estimation for pem fuel cell using rbf neural network and enhanced particle swarm optimization », *Mathematical Problems in Engineering*, vol. 2013, 2013.

[146] F. Z. Belhaj, H. El Fadil, Z. El Idrissi, A. Intidam, M. Koundi, and F. Giri, « New equivalent electrical model of a fuel cell and comparative study of several existing models with experimental data from the pemfc nexa 1200 w », *Micromachines*, vol. 12, *9*, p. 1047, 2021.

[147] C. Restrepo, T. Konjedic, A. Garces, J. Calvente, and R. Giral, « Identification of a proton-exchange membrane fuel cell's model parameters by means of an evolution strategy », *IEEE Transactions on Industrial Informatics*, vol. 11, *2*, pp. 548–559, 2015. DOI: 10.1109/TII.2014.2317982.

[148] A. Alyakhni, L. Boulon, J.-M. Vinassa, and O. Briat, « A comprehensive review on energy management strategies for electric vehicles considering degradation using aging models », *IEEE Access*, vol. 9, pp. 143 922–143 940, 2021.

[149] K. Deng, Y. Liu, D. Hai, *et al.*, « Deep reinforcement learning based energy management strategy of fuel cell hybrid railway vehicles considering fuel cell aging », *Energy Conversion and Management*, vol. 251, p. 115 030, 2022.

[150] K. Chen, S. Laghrouche, and A. Djerdir, « Aging prognosis model of proton exchange membrane fuel cell in different operating conditions », *International Journal of Hydrogen Energy*, vol. 45, *20*, pp. 11 761–11 772, 2020.

[151] M. Gallo, P. Polverino, J. Mougin, B. Morel, and C. Pianese, « Coupling electrochemical impedance spectroscopy and model-based aging estimation for solid oxide fuel cell stacks lifetime prediction », *Applied Energy*, vol. 279, p. 115 718, 2020.

[152] S. S. Madani, E. Schaltz, and S. K. Kær, « A review of different electric equivalent circuit models and parameter identification methods of lithium-ion batteries », *ECS Transactions*, vol. 87, *1*, p. 23, 2018.

[153] R. R. Thakkar, « Electrical equivalent circuit models of lithium-ion battery », *Management and Applications of Energy Storage Devices*, 2021.

[154] X. He, B. Sun, W. Zhang, X. Fan, X. Su, and H. Ruan, « Multi-time scale variable-order equivalent circuit model for virtual battery considering initial polarization condition of lithium-ion battery », *Energy*, p. 123 084, 2022.

[155] Z. Wei, J. Hu, H. He, Y. Li, and B. Xiong, « Load current and state-of-charge coestimation for current sensor-free lithium-ion battery », *IEEE Transactions on Power Electronics*, vol. 36, *10*, pp. 10 970–10 975, 2021.

[156] I. Baccouche, S. Jemmali, B. Manai, N. Omar, and N. E. B. Amara, « Improved ocv model of a li-ion nmc battery for online soc estimation using the extended kalman filter », *Energies*, vol. 10, *6*, p. 764, 2017.

[157] W.-Y. Chang, « The state of charge estimating methods for battery: a review », *International Scholarly Research Notices*, vol. 2013, 2013.

[158] P. Ningrum, N. A. Windarko, and S. Suhariningsih, « Estimation of state of charge (soc) using modified coulomb counting method with open circuit compensation for battery management system (bms) », *JAREE (Journal on Advanced Research in Electrical Engineering)*, vol. 5, *1*, 2021.

[159] S. Loew, A. Anand, and A. Szabo, « Economic model predictive control of li-ion battery cyclic aging via online rainflow-analysis », *Energy Storage*, vol. 3, *3*, e228, 2021.

[160] S. Pelletier, O. Jabali, G. Laporte, and M. Veneroni, « Battery degradation and behaviour for electric vehicles: review and numerical analyses of several models », *Transportation Research Part B: Methodological*, vol. 103, pp. 158–187, 2017.

[161] B. Traore, « Gestion optimisée et coordonnée des flux énergétiques dans les systèmes multi-sources: applications aux véhicules électriques », Ph.D. dissertation, Nantes, 2021.

[162] J. Solano, S. Jemei, L. Boulon, L. Silva, D. Hissel, and M.-C. Pera, « Ieee vts motor vehicles challenge 2020-energy management of a fuel cell/ultracapacitor/lead-acid battery hybrid electric vehicle », *in 2019 IEEE Vehicle Power and Propulsion Conference (VPPC)*, IEEE, 2019, pp. 1–6.

[163] E. G. Amaya, H. Chiacchiarini, C. De Angelo, and M. Asensio, « The energy management strategy of fc/battery vehicles winner of the 2017 ieee vts motor vehicles challenge », *in 2017 IEEE Vehicle Power and Propulsion Conference (VPPC)*, IEEE, 2017, pp. 1–6.

[164] F. Naseri, S. Karimi, E. Farjah, and E. Schaltz, « Supercapacitor management system: a comprehensive review of modeling, estimation, balancing, and protection techniques », *Renewable and Sustainable Energy Reviews*, p. 111 913, 2021.

[165] F. Corti, M.-S. Gulino, M. Laschi, *et al.*, « Time-domain circuit modelling for hybrid supercapacitors », *Energies*, vol. 14, *20*, p. 6837, 2021.

[166] K. Subasinghage, K. Gunawardane, N. Padmawansa, N. Kularatna, and M. Moradian, « Modern supercapacitors technologies and their applicability in mature electrical engineering applications », *Energies*, vol. 15, *20*, p. 7752, 2022.

[167] N. Ma, D. Yang, S. Riaz, L. Wang, and K. Wang, « Aging mechanism and models of supercapacitors: a review », *Technologies*, vol. 11, *2*, p. 38, 2023.

[168] C. T. Sarr, M. B. Camara, and B. Dakyo, « Supercapacitors aging assessment in wind/tidal intermittent energies application with variable temperature », *Journal of Energy Storage*, vol. 46, p. 103 790, 2022.

[169] D. Li, S. Li, S. Zhang, J. Sun, L. Wang, and K. Wang, « Aging state prediction for supercapacitors based on heuristic kalman filter optimization extreme learning machine », *Energy*, vol. 250, p. 123 773, 2022.

[170] Z. Yi, K. Zhao, J. Sun, L. Wang, K. Wang, and Y. Ma, « Prediction of the remaining useful life of supercapacitors », *Mathematical Problems in Engineering*, vol. 2022, pp. 1–8, 2022.

[171] E. Hleihel, M. Fadel, and H. Y. Kanaan, « Simulation of an islanded dc microgrid using instantaneous and average modeling approaches », *ELECTRIMACS 2019: Selected Papers-Volume 1*, vol. 615, p. 193, 2020.

[172] M. J. Carrizosa, F. D. Navas, G. Damm, and F. Lamnabhi-Lagarrigue, « Optimal power flow in multi-terminal hvdc grids with offshore wind farms and storage devices », *International Journal of Electrical Power & Energy Systems*, vol. 65, pp. 291–298, 2015.

[173] A. Benchaib, *Advanced Control of AC/DC Power Networks: System of Systems Approach Based on Spatio-temporal Scales*. John Wiley & Sons, 2015.

[174] C. Mahjoubi, J.-C. Olivier, S. Skander-Mustapha, M. Machmoum, and I. Slama-Belkhodja, « An improved thermal control of open cathode proton exchange membrane fuel cell », *International Journal of Hydrogen Energy*, vol. 44, *22*, pp. 11 332–11 345, 2019.

[175] J.-J. E. Slotine, W. Li, *et al.*, *Applied nonlinear control*. Prentice hall Englewood Cliffs, NJ, 1991, vol. 199.

[176] V. Utkin and J. Shi, « Integral sliding mode in systems operating under uncertainty conditions », *in Proceedings of 35th IEEE conference on decision and control*, IEEE, vol. 4, 1996, pp. 4591–4596.

[177] A.-J. Munoz-Vazquez, V. Parra-Vega, A. Sanchez, and H. Ramirez-Rodriguez, « A passive velocity field for navigation of quadrotors with model-free integral sliding mode control », *in 2013 International Conference on Unmanned Aircraft Systems (ICUAS)*, IEEE, 2013, pp. 49–58.

[178] E. Schulken and A. Crassidis, « Model-free sliding mode control algorithms including application to a real-world quadrotor », *in Pro-ceedings of the 5th International Conference of Control, Dynamic Systems, and Robotics (CDSR'18), Niagara Falls, Canada—June 7–9*, 2018.

[179] Y. Shtessel, C. Edwards, L. Fridman, A. Levant, *et al.*, *Sliding mode control and observation*. Springer, 2014, vol. 10.

[180] S.-D. Lee, B.-K. Lee, and S.-S. You, « Sliding mode control with super-twisting algorithm for surge oscillation of mooring vessel system », *Journal of the Korean Society of Marine Environment & Safety*, vol. 24, 7, pp. 953–959, 2018.

[181] Y. B. Shtessel, J. A. Moreno, and L. M. Fridman, « Twisting sliding mode control with adaptation: lyapunov design, methodology and application », *Automatica*, vol. 75, pp. 229–235, 2017.

[182] V. I. Utkin, *Sliding modes in control and optimization*. Springer Science & Business Media, 2013.

[183] M. A. Golkani, S. Koch, R. Seeber, M. Reichhartinger, and M. Horn, « An anti-windup scheme for the super-twisting algorithm », *in 2019 IEEE 58th Conference on Decision and Control (CDC)*, IEEE, 2019, pp. 6947–6952.

[184] L. Oliveira, A. Bento, V. J. Leite, and F. Gomide, « Evolving granular feedback linearization: design, analysis, and applications », *Applied Soft Computing*, vol. 86, p. 105 927, 2020.

[185] R. Saidi, J.-C. Olivier, M. Machmoum, and E. Chauveau, « Energy management and sizing algorithm applied on a hybrid power system suppliying an isolated residential application », *in IECON 2018-44th Annual Conference of the IEEE Industrial Electronics Society*, IEEE, 2018, pp. 1783–1788.

[186] S. Sze and K. K. Ng, « Physics of semiconductor devices. hoboken, new jersey: john wiley & sons », *Inc.–2007*, 2006.

[187] R. Bravo and M. Dokainish, « Non-linear trajectory control of flexible joint manipulators », *in Current Advances in Mechanical Design and Production VII*, Elsevier, 2000, pp. 37–44.

[188] N. Ghanbari and S. Bhattacharya, « A droop control algorithm with frequency partitioning capability and soc balancing for different energy storage systems », *in 2022 IEEE Applied Power Electronics Conference and Exposition (APEC)*, IEEE, 2022, pp. 1931–1938.

[189] R. T. Bambang, A. S. Rohman, C. J. Dronkers, R. Ortega, A. Sasongko, *et al.*, « Energy management of fuel cell/battery/supercapacitor hybrid power sources using model predictive control », *IEEE Transactions on Industrial Informatics*, vol. 10, *4*, pp. 1992–2002, 2014.

[190] E. D. Kostopoulos, G. C. Spyropoulos, and J. K. Kaldellis, « Real-world study for the optimal charging of electric vehicles », *Energy Reports*, vol. 6, pp. 418–426, 2020.

[191] Y. Preger, H. M. Barkholtz, A. Fresquez, *et al.*, « Degradation of commercial lithium-ion cells as a function of chemistry and cycling conditions », *Journal of The Electrochemical Society*, vol. 167, *12*, p. 120 532, 2020.

[192] K. Ogura and M. L. Kolhe, « Battery technologies for electric vehicles », *in Electric Vehicles: Prospects and Challenges*, Elsevier, 2017, pp. 139–167.

[193] J.-G. Muñoz, F. Angulo, and D. Angulo-Garcia, « Designing a hysteresis band in a boost flyback converter », *Mechanical Systems and Signal Processing*, vol. 147, p. 107 080, 2021.

[194] Y. Shi, B. Xu, Y. Tan, D. Kirschen, and B. Zhang, « Optimal battery control under cycle aging mechanisms in pay for performance settings », *IEEE Transactions on Automatic Control*, vol. 64, *6*, pp. 2324–2339, 2018.

[195] B. Gundogdu and D. T. Gladwin, « A fast battery cycle counting method for grid-tied battery energy storage system subjected to microcycles », *in 2018 International Electrical Engineering Congress (iEECON)*, IEEE, 2018, pp. 1–4.

[196] R. Dufo-López, T. Cortés-Arcos, J. S. Artal-Sevil, and J. L. Bernal-Agustín, « Comparison of lead-acid and li-ion batteries lifetime prediction models in stand-alone photovoltaic systems », *Applied Sciences*, vol. 11, *3*, p. 1099, 2021.

[197] V. Samavatian, H. Iman-Eini, and Y. Avenas, « An efficient online time-temperature-dependent creep-fatigue rainflow counting algorithm », *International Journal of Fatigue*, vol. 116, pp. 284–292, 2018.

[198] T. Dragičević, H. Pandžić, D. Škrlec, I. Kuzle, J. M. Guerrero, and D. S. Kirschen, « Capacity optimization of renewable energy sources and battery storage in an autonomous telecommunication facility », *IEEE Transactions on Sustainable Energy*, vol. 5, *4*, pp. 1367–1378, 2014.

[199] V. Muenzel, J. de Hoog, M. Brazil, A. Vishwanath, and S. Kalyanaraman, « A multi-factor battery cycle life prediction methodology for optimal battery management », *in Proceedings of the 2015 ACM Sixth International Conference on Future Energy Systems*, 2015, pp. 57–66.

[200] J. Fleer, S. Zurmühlen, J. Badeda, P. Stenzel, J.-F. Hake, and D. U. Sauer, « Model-based economic assessment of stationary battery systems providing primary control reserve », *Energy Procedia*, vol. 99, pp. 11–24, 2016.

[201] M. Alam and T. Saha, « Cycle-life degradation assessment of battery energy storage systems caused by solar pv variability », *in 2016 IEEE Power and Energy Society General Meeting (PESGM)*, IEEE, 2016, pp. 1–5.

[202] Y. Shi, B. Xu, Y. Tan, and B. Zhang, « A convex cycle-based degradation model for battery energy storage planning and operation », *in 2018 Annual American Control Conference (ACC)*, IEEE, 2018, pp. 4590–4596.

[203] G. He, Q. Chen, C. Kang, P. Pinson, and Q. Xia, « Optimal bidding strategy of battery storage in power markets considering performance-based regulation and battery cycle life », *IEEE Transactions on Smart Grid*, vol. 7, *5*, pp. 2359–2367, 2015.

[204] K. Abdulla, J. De Hoog, V. Muenzel, *et al.*, « Optimal operation of energy storage systems considering forecasts and battery degradation », *IEEE Transactions on Smart Grid*, vol. 9, *3*, pp. 2086–2096, 2016.

[205] M. Koller, T. Borsche, A. Ulbig, and G. Andersson, « Defining a degradation cost function for optimal control of a battery energy storage system », *in 2013 IEEE Grenoble Conference*, IEEE, 2013, pp. 1–6.

[206] D. Tran and A. M. Khambadkone, « Energy management for lifetime extension of energy storage system in micro-grid applications », *IEEE Transactions on Smart Grid*, vol. 4, *3*, pp. 1289–1296, 2013.

[207] J. Jeewandara, J. Karunadasa, and K. Hemapala, « Comprehensive study of kalman filter based state of charge estimation method for battery energy management system in microgrid », *in 2021 International Conference on Electrical, Computer, Communications and Mechatronics Engineering (ICECCME)*, IEEE, 2021, pp. 01–06.

[208] K. Movassagh, A. Raihan, B. Balasingam, and K. Pattipati, « A critical look at coulomb counting approach for state of charge estimation in batteries », *Energies*, vol. 14, *14*, p. 4074, 2021.

[209] L. Serrao, S. Onori, A. Sciarretta, Y. Guezennec, and G. Rizzoni, « Optimal energy management of hybrid electric vehicles including battery aging », *in Proceedings of the 2011 American control conference*, IEEE, 2011, pp. 2125–2130.

[210] J. Porzio and C. D. Scown, « Life-cycle assessment considerations for batteries and battery materials », *Advanced Energy Materials*, vol. 11, *33*, p. 2 100 771, 2021.

[211] S. Kassir, M. Doumiati, M. Machmoum, C. Francis, and E. Elrafei, « Energy management system based on cost optimization of battery aging and hydrogen consumption in a microgrid », *International Review of Electrical Engineering*, 2022.

[212] I. Abdallah, A.-L. Gehin, and B. O. Bouamama, « Hybrid bond graph modelling of multi-source system for green hydrogen production », *in 2017 25th Mediterranean Conference on Control and Automation (MED)*, IEEE, 2017, pp. 1398–1403.

[213] D.-I. Stroe, V. Knap, M. Swierczynski, A.-I. Stroe, and R. Teodorescu, « Operation of a grid-connected lithium-ion battery energy storage system for primary frequency regulation: a battery lifetime perspective », *IEEE Transactions on Industry Applications*, vol. 53, *1*, pp. 430–438, 2017. DOI: 10.1109/TIA.2016.2616319.

[214] E. Haghi, M. Fwoler, and K. Raahemifar, « Economic analysis of hydrogen production in context of a microgrid », *in 2017 IEEE International Conference on Smart Energy Grid Engineering (SEGE)*, IEEE, 2017, pp. 79–84.

[215] H. Council, « Path to hydrogen competitiveness: a cost perspective », 2020.

Résumé

La crise environnementale conduit à l'intégration des sources d'énergie renouvelable dans les réseaux, ce qui entraîne l'émergence de micro-réseaux (MR) pour l'alimentation électrique des zones rurales et urbaines. Cependant, les micro-réseaux sont confrontés à des défis lors de l'intégration de sources d'énergie renouvelable en raison de leur caractère intermittent et de leur connexion via des convertisseurs électroniques de puissance. Cela peut rendre le réseau électrique plus vulnérable et instable. Des systèmes de stockage d'énergie tels que des batteries, des volants d'inertie, des réservoirs d'hydrogène et des systèmes de stockage hydraulique sont utilisés pour stocker l'énergie excédentaire pendant les périodes de surproduction. En combinant les sources d'énergie renouvelable avec le stockage d'énergie et les générateurs de secours, les micro-réseaux deviennent des systèmes d'énergie autonomes qui produisent, stockent et distribuent l'électricité. Pour gérer efficacement la puissance à travers les différents composants, une stratégie de contrôle globale est nécessaire. Il existe plusieurs topologies des micro-réseaux connectés ou isolés avec un courant continu ou alternatif ou mixte. L'étude dans ce travail de thése concerne les micro-réseaux isolés et en courant continu (DC). Dans ces micro-réseaux, la régulation de tension et le partage de courant/puissance sont des objectifs de contrôle clés pour assurer un bon fonctionnement et éviter la surcharge des sources d'énergie. Le principal objectif de cette thèse qui est divisé en deux parties principales, est d'assurer la stabilité, la résilience et la fiabilité d'un micro-réseau. La première partie concerne le contrôle du bus DC et des unités locales, tandis que la deuxième partie se concentre sur le système de gestion de l'énergie. Ces deux parties relèvent du système de contrôle global du micro-réseau. Dans la littérature, différentes approches de contrôle et de gestion de l'énergie ont été proposées, chacune ayant ses propres objectifs, avantages et compromis en fonction de l'architecture du système. À ce jour, aucune technique ou stratégie unique n'a émergé comme solution universellement optimale pour toutes les situations réelles, et un travail considérable doit être réalisé pour comparer les différentes stratégies.

Cette thèse se compose de cinq chapitres. Le premier chapitre débute par une introduction générale et se concentre ensuite sur la définition d'un système hybride d'énergie renouvelable (HRES). La première partie aborde l'hybridation des sources d'énergie et

des systèmes de stockage, mettant en évidence leurs modalités, leur importance et les différentes combinaisons possibles. Elle explore également les complémentarités entre ces sources. Ce chapitre comprend également une revue de la littérature sur les topologies des micro-réseaux, qui fait référence à l'arrangement physique des composants au sein d'un micro-réseau. Le premier chapitre présente aussi une revue de la littérature sur les éléments fondamentaux qui composent le micro-réseau étudié, notamment les systèmes PV, les piles à combustible, les batteries, les supercondensateurs et les convertisseurs électroniques de puissance. L'étude analyse de manière critique les techniques de contrôle et de gestion de l'énergie mises en œuvre dans les systèmes multi-sources. Elle discute en détail des avantages et des limitations de chaque approche. Cette analyse permet de situer le travail de thèse et de définir les objectifs de recherche.

En fait, les stratégies de contrôle et de gestion de l'énergie pour le Micro-réseau dépendent fortement de l'architecture du Micro-réseau étudié. Par conséquent, la conception de l'architecture du Micro-réseau est un aspect critique du projet dans son ensemble. Ainsi, pour une mise en œuvre réussie de toute application, cela nécessite un système multi-source correctement conçu pour le soutenir en termes de sa topologie, du nombre de sources, des caractéristiques et de l'interface électrique. Le deuxième chapitre est consacré à la modélisation du micro-réseau. L'architecture du Micro-réseau étudié est présentée, y compris les principaux éléments constructifs tels que le système photovoltaïque, la pile à combustible, la batterie, le supercondensateur et leurs convertisseurs électriques correspondants. Deux types de convertisseurs sont utilisés, des convertisseurs bidirectionnel pour les sources réversibles (unités de stockage d'énergie : batterie et supercondensateur) et des convertisseurs de type boost unidirectionnels pour les sources irréversibles, qui sont le système PV et la pile à combustible. Le chapitre présente également la modélisation de chacun de ces composants. De plus, une brève revue de littérature sur les modèles de vieillissement de la pile à combustible, de la batterie et du supercondensateur est présentée. La modélisation des convertisseurs électroniques de puissance est présentée de deux manières différentes. Le modèle choisi pour simuler et évaluer la structure de contrôle dans le système MR étudié est le modèle instantané, qui représente de manière précise les signaux électriques dans le convertisseur. Cependant, le système MR est catégorisé comme complexe en raison de ses multiples composants, de ses interactions non linéaires et de sa conception de contrôle hiérarchique. La simulation d'un système complexe avec des profils réalistes sur une période étendue pose des défis de calcul et nécessite une mémoire significative. Pour concilier une modélisation détaillée et une simulation efficace, la méthode

de modélisation moyenne est utilisée pour les convertisseurs boost et bidirectionnels dans la simulation du système de gestion de l'énergie, répondant ainsi au besoin de simulations sur des périodes prolongées.

Le maintien d'une tension continue (DC) stable dans un micro-réseau DC est crucial pour une distribution d'énergie fiable, la stabilité du réseau, la protection du stockage d'énergie et une gestion énergétique efficace. Cette thèse met l'accent sur l'importance d'une tension DC stable pour améliorer la fiabilité et la résilience du micro-réseau DC, même face à des perturbations importantes, des variations de paramètres et du bruit des capteurs. Pour un fonctionnement stable de ce micro-réseau DC, il est nécessaire de garantir l'équilibre de puissance entre la production et la consommation.

Le troisième chapitre se concentre sur la structure de contrôle proposée pour l'application étudiée. Pour expliquer son fonctionnement interne, commençons par le panneau solaire photovoltaïque (PV). Afin d'extraire la puissance maximale pouvant être générée par le système solaire, le contrôle de haut niveau du panneau PV représenté par l'algorithme de poursuite du point de puissance maximale (MPPT) génère une tension de référence variant dans le temps à suivre par le contrôle local au niveau du convertisseur de PV. Lorsque toute la puissance PV est générée et directement consomée par la charge, tout excès ou déficience de puissance au niveau du bus DC doit être pris en charge par les autres éléments d'énergie restants (FC, Batt et SC). Cela se fait en fonction des spécifications et caractéristique de chaque élément pour s'adapter à de telles fluctuations. Ainsi, un régulateur de tension du bus DC au niveau supérieur calcule le courant total requis à fournir/absorber par les unités de stockage de manière à respecter le principe de l'équilibre énergétique.

Le système présente un comportement multi-échelle caractérisé par la présence de transitoires rapides, intermédiaires et lents. Par conséquent, le courant de référence total est transmis aux unités de stockage par le biais d'un système de gestion de l'énergie qui joue le rôle de l'allocation de courant. Il répartit le courant entre les différentes unités (Batt, SC et FC) en fonction de leurs spécifications physiques et dynamiques. Ensuite, chaque fraction de courant est suivie par son contrôleur local correspondant, en générant un rapport cyclique pour contrôler le convertisseur associé. Du point de vue de la dynamique du courant et de la tension, la dynamique du courant doit être contrôlée de manière à être beaucoup plus rapide que la dynamique de la tension. Par conséquent, le système peut fonctionner sur plusieurs échelles de temps. De plus, une boucle de contrôle proportionnelle-intégrale (PI) supplémentaire est mise en œuvre pour réguler l'état de charge (SoC) du supercon-

densateur. Cette boucle de contrôle prend en compte la caractéristique de décharge rapide du supercondensateur. En surveillant et en gérant activement le SoC, le système de contrôle optimise le fonctionnement du supercondensateur pour maintenir ses performances et sa longévité. La technique principale de contrôle utilisée dans la structure de contrôle est le contrôle de mode glissant sans-modèle Super-Twisting (MF-STSMC).

Afin d'évaluer la fonctionnalité et la faisabilité de la structure de contrôle et de la loi proposées, des simulations numériques ont été réalisées à l'aide de MATLAB/Simulink. Diverses conditions de test ont été étudiées, notamment des variations de la puissance générée, des fluctuations de la demande de charge, des variations de paramètres et du bruit potentiel des capteurs. Deux régulateurs candidats basés-modèles, à savoir le bouclage linéarisant "Feedback Linearization" (FL) et la technique de Contrôle en Mode Glissant (SMC) conventionnelle, ont été sélectionnés pour la comparaison avec la technique proposée. Dans l'ensemble, les résultats confirment que la structure de contrôle et la technique choisies maintiennent efficacement la stabilité de la tension du bus DC tout au long de la période de simulation, notamment après l'injection des perturbations. Cette stabilité se traduit par d'excellentes performances de suivi du Model Free Sliding Mode Control (MFSMC), qui suit efficacement les transitoires et se stabilise rapidement à la consigne souhaitée. Le MFSMC a également démontré une meilleure robustesse face aux variations de paramètres et aux perturbations par rapport aux autres régulateurs, avec moins de dépassements, ainsi qu'une réponse rapide aux perturbations imposées. De plus, une analyse de sensibilité a été réalisée en introduisant du bruit dans les capteurs, révélant que le MFSMC présente une sensibilité nettement inférieure par rapport à FL.

Chaque unité du système multi-source a ses propres spécifications, exigences dynamiques, sens de flux faisable, limitations de puissance en charge et décharge, ainsi que d'autres contraintes spécifiques. Afin d'assurer une utilisation maximale et efficace des unités, le défi consiste à fournir un système de gestion de l'énergie approprié (EMS). Cet EMS agit en tant que coordinateur des flux d'énergie en prenant en compte toutes les contraintes et exigences du système. L'objectif principal d'un tel EMS est de gérer efficacement en temps-réel les flux d'énergie internes tout en garantissant des conditions de fonctionnement saines et sécurisées pour le Micro-réseau. Le quatrième chapitre est consacré au développement de la stratégie du système de gestion de l'énergie. Pour le système multi-source etudié, le processus de vieillissement des différentes unités et la minimisation du coût de consommation de carburant (H2) sont deux critères essentiels à prendre en compte dans l'EMS. D'une part, la dégradation des divers composants affecte largement

le coût, l'efficacité et donc les performances de l'ensemble du système. D'autre part, la consommation de carburant (H2) représente une part importante du coût d'exploitation du système. Ainsi, optimiser à la fois le taux de dégradation des unités du système et le coût de consommation d'hydrogène serait d'un grand intérêt, en particulier lorsqu'il est intégré à un EMS conçu pour la gestion du SoC de la batterie. Dans ce contexte, la stratégie de gestion proposée visant une meilleure distribution de la puissance demandée répond à ces exigences cruciales en se basant sur une optimisation des coûts entre la consommation d'hydrogène et le vieillissement de la batterie. Il est important de noter que l'un des principaux objectifs de cette approche EMS, outre l'assurance de l'équilibre de puissance dans le système, est de maintenir l'état de charge de la batterie dans ses limites tout en optimisant la consommation d'hydrogène et le vieillissement de la batterie. Ainsi, la batterie et la pile à combustible sont les deux unités spécifiques concernées par cette optimisation. En conséquence, l'intérêt principal est de trouver un moyen d'influencer directement ces parties de basse et moyenne fréquence. En effet, les deux principaux facteurs qui influencent la sortie d'un filtre passe-bas sont sa fréquence de coupure et son gain. En modifiant le gain, on affecte directement l'amplitude des signaux à toutes les fréquences, en ciblant plus particulièrement les signaux de basse à moyenne fréquence qui concernent respectivement la pile à combustible et la batterie.

Dans l' EMS à filtrage simple, la référence de courant totale générée par le controlleur de bus DC est répartie sur plusieurs composants, c'est-à-dire la pile à combustible (FC), la batterie (Batt) et le supercondensateur (Sc), chacun étant chargé d'accomplir sa tâche associée, c'est-à-dire de suivre sa référence de courant correspondante. En effet, contraindre l'un de ces composants à accomplir plus ou moins que sa tâche assignée, en faisant varier le gain du filtre, se fera au détriment de l'autre composant. Ainsi, dans ce cas, un problème d'optimisation doit nécessairement être pris en compte pour sélectionner, dans une large mesure, la meilleure valeur de gain satisfaisant les exigences du système. Par conséquent, lorsque l'état de charge (SoC) de la batterie nécessite une intervention en raison d'une surcharge ou d'une décharge profonde, l'action de faire varier le gain dans le premier filtre passe-bas, c'est-à-dire destiné à répartir la puissance entre la pile à combustible et la batterie, permet d'ajuster le poids de la tâche entre la FC et la Batt. Cela implique une sorte de changement de rôle entre les deux sources tout en respectant les contraintes de fonctionnement imposées sur le système.

L'idée principale de l'approche proposée est de créer un filtre à gain programmé où les gains sont sélectionnés en ligne pendant le fonctionnement, par exemple en passant entre

1, G_{min} et G_{max}. Le gain $G = 1$ est utilisé lors du fonctionnement normal lorsque la valeur de l'état de charge (SoC) se situe dans sa plage définie pour un fonctionnement optimal, tandis que G_{min} et G_{max} sont les valeurs de gain responsables de la gestion de l'état de charge de la batterie. Ces valeurs sont choisies en résolvant un problème d'optimisation qui prend en compte le coût d'utilisation de la batterie et le coût de la consommation d'hydrogène. En mode de fonctionnement normal ($SoC_{min} \leqslant SoC_{batterie} \leqslant SoC_{max}$), le gain sélectionné est de 1, c'est-à-dire comme dans le filtrage en cascade passif. En cas de surcharge ($SoC_{batterie} \geq SoC_{max}$), la pile à combustible est sollicitée avec une moindre implication, le gain sélectionné est donc G_{min} (< 1), ce qui se traduit par une économie d'hydrogène au détriment d'une exploitation accrue de la batterie. Dans un contexte de décharge profonde ($SoC_{batterie} \leqslant SoC_{min}$), une demande d'augmentation de la contribution de la pile à combustible est lancée, le gain est donc choisi à G_{max} (> 1), de cette manière, une utilisation réduite de la batterie est obtenue au prix d'une consommation accrue d'hydrogène tant que le stock d'hydrogène le permet. La figure 5.30 montre le diagramme de l'EMS proposé incluant sa gestion de batterie, où le choix des gains à appliquer est réalisé à l'aide de deux relais d'hystérésis et d'un commutateur. Les hystérésis sont utilisés pour détecter la situation dans laquelle se trouve le système et générer ainsi la valeur de gain appropriée. Le relais d'hystérésis 1 aide à gérer la batterie lors d'une surcharge, tandis que le relais d'hystérésis 2 fonctionne en cas de décharge profonde de la batterie. Selon la valeur de l'état de charge de la batterie, en utilisant les relais d'hystérésis 1 et 2, la valeur de gain est soit G_{min}, 1 ou G_{max}. Le commutateur capture la valeur de gain générée et l'envoie au bloc de filtrage en cascade.

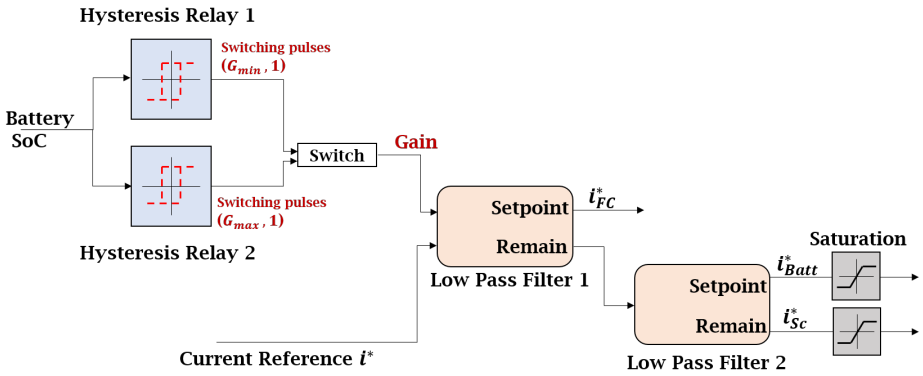

Figure 5.30 – Gain scheduled filtering EMS.

Trois étapes principales constituent la phase de conception de la technique de l'EMS, ce qui signifie la détermination de chaque valeur de G_{min} et G_{max}. La première étape

marque la phase de collecte des données de l'ensemble de variables à optimiser (les profiles de SOC de la batterie generés a partir de chaque gain candidat ainsi que le courant sortant de la pile à combustible) les étapes 2 et 3 concernent la phase d'analyse des données. Dans la première étape, pour chaque cas de G_{min} et G_{max}, un ensemble de valeurs de gain candidates est sélectionné, puis une simulation du système contrôlé est réalisée à chaque fois avec un gain de cet ensemble et les données sont collectées pour les deux étapes suivantes. De cette manière, chaque valeur du gain candidat possède un ensemble de données prêtes à être utilisées dans le problème d'optimisation. Ensuite, l'étape 2 consiste à calculer et préparer les termes de la fonction de coût. Ces termes expriment le coût de consommation de masse d'hydrogène et le coût d'utilisation de la batterie. Pour le coût d'utilisation de la batterie, deux variables essentielles doivent être calculées: le facteur de sévérité et le cycle complet équivalent de la batterie. Le facteur de sévérité est défini comme un facteur caractérisant l'effet de vieillissement de n'importe quel cycle que la batterie traverse par rapport à son cycle nominal prédéfini. Ce facteur permet une estimation plus précise du vieillissement de la batterie. Quant au cycle complet équivalent de la batterie, l'algorithme Rain-flow est utilisé pour compter les cycles partiels de chaque profil SoC, puis recalculer le cycle complet équivalent. Le coût de consommation d'hydrogène est estimé en fonction du courant de la pile à combustible. Enfin, l'étape 3 concerne la définition de la fonction de coût multi-objectif avec ses contraintes afin de définir le problème d'optimisation et la normalisation des termes de la fonction de coût. Cette optimisation vise à produire les valeurs quasi-optimales de G_{min} et G_{max}.

Des simulations numériques ont été réalisées pour évaluer la performance de l'algorithme proposé de SGE. Les résultats de simulation ont été comparés à ceux de deux autres stratégies candidates dans les mêmes conditions du système ("Rate-Limiter" et découplage de fréquence). La stratégie proposée a démontré des économies de coûts significatives en réduisant la consommation d'hydrogène sans affecter de manière significative la dégradation de la batterie. Un graphique comparatif présenté dans la thèse a clairement illustré l'augmentation minime de l'utilisation de la batterie par rapport à la diminution substantielle de la consommation d'hydrogène, mettant en évidence l'avantage précieux de la stratégie proposée.

Le dernier chapitre est consacré à la mise en œuvre des algorithmes de contrôle et à leur validation sur un système multisource réel, qui comprend une pile à combustible émulée et deux types différents de systèmes de stockage d'énergie et de puissance avec des technologies différentes (batterie et supercondensateur). L'objectif principal de ce chapitre

est de démontrer que la méthode de contrôle est pratique et peut être mise en œuvre en temps-réel de manière efficace. Le chapitre commence par présenter le banc d'essai utilisé pour les tests "Hardware in the loop" (HIL) (les sources d'énergie, convertisseurs, les différents types de capteurs, etc). Le chapitre couvre aussi la mise en œuvre de l'ensemble du système en utilisant MATLAB/SIMULINK, dSPACE et l'interface temps-réel ControlDesk. Les sources d'énergie sont connectées au modèle Simulink via l'interface ControlDesk, ce qui permet un échange de données en temps-réel entre le matériel et le logiciel. Trois scénarios différents sont réalisés pour évaluer les performances de la structure de contrôle. Sur la base de ces résultats, le MFSMC s'est révélé être très efficace en termes de facilité de mise en œuvre et de performance, tout en résolvant efficacement le problème de "chattering" en mode glissant, ce qui se traduit par un système de contrôle plus stable et plus précis. De plus, les résultats démontrent la capacité du contrôleur à répondre rapidement aux changements de consigne et à maintenir une précision de performance en régime permanent en suivant de près la valeur de référence souhaitée.

Contributions : Les contributions scientifiques principales de cette recherche peuvent être résumées comme suit :

- L'utilisation d'un MF-STSMC associé à une technique anti-dépassement garantissant les points suivants :
  - Un fonctionnement stable et fiable du système avec une qualité d'alimentation constante.
  - Robustesse face aux incertitudes et perturbations.
  - Limitation du phénomène de d'oscillation forte (Chattering).
  - Prévention de la dérive du contrôleur en cas de saturation.
- Structure de contrôle globale avec deux niveaux (niveau inférieur : contrôle local, niveau supérieur : contrôle global).
- Régulation de l'état de charge (SoC) de la batterie dans des marges cibles prédéfinies grâce à une technique de filtrage avec ajustement des gains.
- Optimisation des coûts entre l'utilisation de la batterie et la consommation d'hydrogène, en recherchant la meilleur valeur possible de gain, appropriée pour la régulation du SoC, parmi un ensemble fini de gains.

Perspectives :

- Développer l'approche de l'EMS pour inclure l'etat de charge supercondensateur

et le viellissement de la pile dans le problème d'optimisation.
— Viser une opération en temps-réel de l'approche de l'EMS en incorporant la prédiction en ligne du profil de charge et les prévisions météorologiques.
— Développer un gain variable continu au lieu du gain discret actuel, où une courbe de gains optimaux en fonction de l'état de charge (SoC) peut être dérivée, et on s'attend à ce que cela permette une planification plus précise que le concept d'hystérésis.
— Pour se rapprocher le plus possible des valeurs de gain optimales, il serait bénéfique d'augmenter le nombre de valeurs de gain potentielles prises en compte.
— Inclure un électrolyseur dans l'architecture : Évaluer la faisabilité de l'intégration et développer un modèle pour l'électrolyseur dans le cadre du contrôle et de l'EMS.
— Évaluer l'adaptabilité des algorithmes développés pour gérer des configurations de micro-réseaux plus complexes (comme des micro-réseaux radiaux ou maillés) en analysant leurs caractéristiques et leurs contraintes.

Ce travail a abouti à la publication de 3 articles de conférences internationales IEEE et 2 papiers de journaux de classe Q2:

— Kassir S, Doumiati M, Machmoum M, Elrafei M, Francis C. DC microgrid voltage stability by Model Free Super-Twisting Sliding Mode Control. In Proceedings of the 47th Annual Conference of the IEEE Industrial Electronics Society (IECON2021), Virtually in Toronto, Canada, October 10-13, 2021.
— Kassir S, Doumiati M, Machmoum M, El Rafei M, Francis C. Robust control and energy management in a hybrid DC microgrid using second-order SMC. In IEEE IECON 2022–48th Annual Conference of the IEEE Industrial Electronics Society, Brussels, Belgium on Oct 17, 2022, (pp. 1-6). IEEE.
— Kassir S, Doumiati M, Machmoum M, Francis C, Elrafei E. Energy management system based on cost optimization of battery aging and hydrogen consumption in a microgrid. International Review of Electrical Engineering 2022, I.R.E.E, PWP, vol. 17(4), pp. 346-359, DOI: https://doi.org/10.15866/iree.v17i4.21983.
— Mroueh M, Kassir S, Doumiati M, Francis C, Machmoum M. A time scale based energy management strategy for hybrid energy storage system in DC Microgrid. In47th IEEE IECON2021 2021 Oct 13.
— Imen Iben Ammar, Moustapha Doumiati, Sarah Kassir, Mohamed Machmoum, Clovis Francis, et al. New Nonlinear Control Based on Polynomial Approach for Islanded DC Microgrid Robustness and Voltage Stability. International Review

of Automatic Control, 2022, 15 (5), pp.263. ⟨10.15866/ireaco.v15i5.22535⟩. ⟨hal-03925300⟩. 20

Titre : Une Approche Intégrée De Gestion Intelligente De L'énergie Et De Contrôle Sans Modèle Pour Les Micro-Réseaux Résidentiels Isolés.

Mot clés : Micro-réseau, Stockage d'énergie, pile à combustible, Gestion optimisée de l'énergie, Consommation d'hydrogène, vieillissement des batteries, contrôleur en mode glissant Super-Twisting.

Résumé : La crise environnementale pousse à l'intégration des énergies renouvelables dans les micro-réseaux pour les zones rurales et urbaines. Cependant, l'adoption des micro-réseaux rencontre des défis de stabilité et de gestion de l'énergie nécessitant des contrôles résilients. Cette thèse propose une structure de contrôle hiérarchique pour un micro-réseau autonome résidentiel, combinant énergie solaire, pile à combustible et stockage hybride (Battery et supercondensateur). La technique de contrôle utilisée est le contrôle en mode glissant super twisting sans modèle avec anti-dépassement pour la saturation. La structure de contrôle vise à assurer un micro-réseau stable et résilient avec une stabilité souhaitée de la tension du bus continu, validée par des tests de simulation et des expériences en boucle fermée. De plus, la thèse propose une nouvelle stratégie de gestion optimisée de l'énergie (EMS) axée sur le partage de puissance et la régulation de l'état de charge de la batterie, en tenant compte de la balance entre l'utilisation de la batterie et les coûts de consommation d'hydrogène. Les tests de simulation confirment la réussite des objectifs prévus par l'EMS.

Title: An Integrated Smart Energy Management and Model-Free Control Approaches for Islanded Residential Microgrids.

Keywords: Microgrid, Energy Storage, Fuel Cell, Optimized Energy Management, Hydrogen Consumption, Battery aging, Super-Twisting Sliding Mode Control.

Abstract: The environmental crisis drives the integration of renewable energy sources into grids, leading to the emergence of microgrids for power supply in rural and urban areas. However, microgrid adoption faces stability and energy management challenges that require resilient control structures and intelligent mechanisms. This thesis proposes a hierarchical control structure for a standalone residential microgrid system, combining solar, fuel cell, and hybrid energy storage (battery and supercapacitor). The control technique employed is model-free super twisting sliding mode control with anti-windup for saturation. The control structure aims to ensure a stable and resilient microgrid with desired DC bus voltage stability, validated through simulation tests and hardware-in-the-loop experiments. Additionally, the thesis proposes a novel optimized energy management strategy (EMS) focusing on power sharing and battery state of charge regulation, considering the trade-off between battery usage and hydrogen consumption costs. Simulation tests confirm the successful achievement of the intended goals by the EMS.